Strojniški vestnik
Journal of Mechanical Engineering

no. 7-8
year 2022
volume 68

Strojniški vestnik – Journal of Mechanical Engineering (SV-JME)

Aim and Scope
The international journal publishes original and (mini)review articles covering the concepts of materials science, mechanics, kinematics, thermodynamics, energy and environment, mechatronics and robotics, fluid mechanics, tribology, cybernetics, industrial engineering and structural analysis.
The journal follows new trends and progress proven practice in the mechanical engineering and also in the closely related sciences as are electrical, civil and process engineering, medicine, microbiology, ecology, agriculture, transport systems, aviation, and others, thus creating a unique forum for interdisciplinary or multidisciplinary dialogue.
The international conferences selected papers are welcome for publishing as a special issue of SV-JME with invited co-editor(s).

Editorial Office
University of Ljubljana, Faculty of Mechanical Engineering
SV-JME, Aškerčeva 6, SI-1000 Ljubljana, Slovenia
Phone: 386 (0)1 4771 137
Fax: 386 (0)1 2518 567
info@sv-jme.eu, http://www.sv-jme.eu

Print: Demat d.o.o., printed in 250 copies

Founders and Publishers
University of Ljubljana, Faculty of Mechanical Engineering, Slovenia
University of Maribor, Faculty of Mechanical Engineering, Slovenia
Association of Mechanical Engineers of Slovenia
Chamber of Commerce and Industry of Slovenia, Metal Processing Industry Association

President of Publishing Council
Mihael Sekavčnik
University of Ljubljana, Faculty of Mechanical Engineering, Slovenia

Vice-President of Publishing Council
Bojan Dolšak
University of Maribor, Faculty of Mechanical Engineering, Slovenia

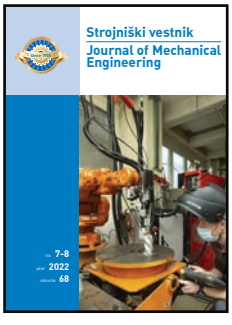

Image Courtesy:
University of Ljubljana,
Faculty of Mechanical Engineering,
Chair of Materials, Science and Technology
Laboratory for Welding,
Slovenia

Photo:
Željko Stevanić, IFP, d.o.o.

General information
Strojniški vestnik – Journal of Mechanical Engineering is published in 11 issues per year (July and August is a double issue).

Institutional prices include print & online access: institutional subscription price and foreign subscription €100,00 (the price of a single issue is €10,00); general public subscription and student subscription €50,00 (the price of a single issue is €5,00). Prices are exclusive of tax. Delivery is included in the price. The recipient is responsible for paying any import duties or taxes. Legal title passes to the customer on dispatch by our distributor. Single issues from current and recent volumes are available at the current single-issue price. To order the journal, please complete the form on our website. For submissions, subscriptions and all other information please visit: *http://www.sv-jme.eu.*

You can advertise on the inner and outer side of the back cover of the journal. The authors of the published papers are invited to send photos or pictures with short explanation for cover content.

We would like to thank the reviewers who have taken part in the peer-review process.

ISSN 0039-2480, ISSN 2536-2948 (online)

The journal is subsidized by Slovenian Research Agency.

SV-JME is indexed / abstracted in: SCI-Expanded, Compendex, Inspec, ProQuest-CSA, SCOPUS, TEMA. The list of the remaining bases, in which SV-JME is indexed, is available on the website.

Strojniški vestnik - Journal of Mechanical Engineering is available on *https://www.sv-jme.eu.*

Contents

Strojniški vestnik - Journal of Mechanical Engineering
volume 68, (2022), number 7-8
Ljubljana, July-August 2022
ISSN 0039-2480

Published monthly

Papers

Strojniški vestnik - Journal of Mechanical Engineering 68(2022)7-8, 451-460
DOI:10.5545/sv-jme.2022.191
Original Scientific Paper
Received for review: 2022-05-08
Received revised form: 2022-06-22
Accepted for publication: 2022-08-05

Short-term Creep Behaviour of Different Polymers Used in Additive Manufacturing under Different Thermal and Loading Conditions

Oguz Dogan*
Kahramanmaras Sutcu Imam University, Department of Mechanical Engineering, Turkey

Polymer materials produced by additive manufacturing undergo significant changes in their dimensions under continuous loading conditions. This situation affects the operation of polymer structures produced by additive manufacturing within safe limits. Therefore, it is crucial to determine the creep behaviour of polymers produced by the additive manufacturing method. This study investigates the creep behaviour of six different materials, acrylonitrile butadiene styrene (ABS), chlorinated polyethylene (CPE), polylactic acid (PLA), tough polylactic acid (TPLA), polycarbonates (PC), and nylon most commonly used in additive manufacturing. The creep test specimens are firstly produced with a three-dimensional (3D) printer, and then their final dimensions are given using computer numerical control (CNC) milling. The creep experiments are carried out at three different ambient temperatures (25 °C, 40 °C, and 60 °C) and two different stress levels (10 MPa, 20 MPa). According to the test results, it was determined that the material type, temperature, and loading levels significantly influenced the creep behaviour of the 3D printed polymer materials.

Keywords: Additive manufacturing, creep experiments, polymer materials, thermal effect

Highlights

- *Creep test specimens are produced with a 3D printer and CNC milling.*
- *Creep tests are performed for different temperatures and loading conditions.*
- *Short-term creep behaviours of polymers are investigated experimentally.*
- *Material type, heat, and loading significantly affected the creep behaviour of the polymer materials.*

0 INTRODUCTION

Fused deposition modelling (FDM) is a production method that allows parts to be processed layer by layer and produced as one piece. As a basic principle, in FDM, the raw material is heated, fluidized, and passed through a nozzle to produce the part in layers. With this production technique, products that cannot be produced in one step with traditional production methods have become easily produced. The FDM technique has started to increase its importance in practical life day by day with the increase and cheapening of three-dimensional (3D) printers. The advantages of FDM are summarized by Ngo et al. [1] as design freedom, customization, waste minimization, and the ability to produce complex structures.

The FDM method allows many different polymer materials to be used in 3D production. PLA, TPLA, ABS, PC, nylon, and CPE are the most commonly used polymer materials in the studies carried out with the FDM method in the literature. PLA is the most commonly used biopolymer and thermoplastic produced from corn starch and sugar cane in 3D printing. PLA enables fast and reliable 3D production with high surface quality [2]. ABS is also commonly used in 3D printing; it is tough and durable, provides high dimensional stability, and is resistant to physical impacts and chemical corrosion [3]. PC is a thermoplastic with a wide range of uses in the modern manufacturing industry; it can be defined as strong, temperature resistant, and tough. PC provides high mechanical strength, ultimate printing quality, and thermal resistance up to 100 °C [4]. Nylon is well known for good elongation, abrasion resistance, high strength-to-weight ratio, and low friction coefficient but a much lower strength [5]. Compared to other materials, the use of CPE with FDM is limited. CPE is defined as chemically resistant and tough [6].

The determination of the mechanical properties of the products produced using the FDM method has attracted great interest with the widespread use of FDM technology. Thus, many researchers have carried out extensive studies on the determination of the mechanical properties of the products produced by FDM. In these studies, generally, the tensile [7], bending [8], and impact [9] strengths of materials produced by the FDM method are experimentally investigated. While the mechanical properties of different materials have been investigated [10], the effects of FDM process parameters on mechanical properties have also been studied [11]. In addition, the fatigue strength of the materials produced with 3D printers has been experimentally investigated [12].

*Corr. Author's Address: Kahramanmaras Sutcu Imam University, Department of Mechanical Engineering, Turkey, oguzdogan@ksu.edu.tr

Creep is the permanent deformation that occurs over time in materials under the influence of a constant temperature, stress, or loading. The creep behaviour of polymer materials is significant in industrial applications where dimensional stability is essential. For this reason, the creep behaviour of polymer materials should be determined, and the designs should be carried out accordingly. Many studies examine the creep behaviour of different polymer materials in the literature. Generally, the researchers are focused on the effects of the printing process parameters on the creep behaviour of the 3D printed materials. Zhang et al. [13] investigated the tensile, creep, and fatigue behaviour of the 3D printed ABS samples. The effects of the printing orientation on the creep properties of the ABS test samples were defined experimentally. The effect of printing orientation on short-term creep behaviour of the 3D printed PLA samples is investigated in another comprehensive study [14]. In addition, the effects of layer thickness and different PLA types on creep are investigated experimentally. Mohammed et al. [15] investigated the flexural creep stiffness behaviour of PC-ABS material produced with FDM. In another study, the authors experimentally investigated the effects of process parameters on the creep and recovery behaviours of samples produced using the FDM method [16]. The creep and recovery behaviour of the reinforced 3D composites are investigated by Al Rashid and Koç [17]. Waseem et al. define the most effective process parameters on the tensile creep behaviour of the 3D printed PLA parts. They proposed the optimal combination of the process parameters using categorical response surface methodology [18]. Some researchers have experimentally investigated the effects of environment variables on creep. Temperature-humidity [19] and creep load [20] are considered variable parameters when these studies are examined. Various models have been used to predict creep in some studies. Lim et al. [21] developed a long-term creep model using the short-term creep test results for PC and ABS. Ye et al. [22] proposed a modified Burger model to predict the creep behaviour of the 3D printed test samples. The proposed model is validated with the creep experiments. As a result of the study, the modified model can accurately calculate the creep behaviour of the PLA-max samples with different printing angles.

According to the literature review, it is seen that the effect of process parameters on the creep behaviour of materials produced by the FDM method has been generally investigated. No study has been found that investigated the creep behaviour of different materials produced by the FDM method. In addition, temperature is one of the most influential parameters on the creep behaviour of the polymer materials. Similarly, when the literature is examined, the studies examining the effects on the creep behaviour of the samples produced with FDM temperature are very limited. These shortcomings in the literature have been the biggest motivation for this study.

The present investigates the creep behaviour of six different polymer materials (ABS, CPE, PLA, TPLA PC, nylon) produced by the FDM method. In addition, experiments are carried out for each material type at three different temperatures (room temperature, 40 °C, and 60 °C) and two different stress levels (10 MPa and 20 MPa). The effect of temperature and stress on the creep behaviour of materials produced by the FDM method has been explained.

1 MATERIAL METHOD

2.1 Production of Creep Test Specimens

In this study, the creep behaviour of the different polymer materials produced with a 3D printer was experimentally investigated. The polymer test specimens were produced by combining FDM and CNC milling operations. The creep test specimens were produced with the Ultimaker 2+ Extended 3D printer. The printing area is 223 mm × 220 mm × 305 mm, and the resolution is 12.5 µm – 12.5 µm – 5 µm for the $x - y - z$ axes, respectively. The dimensions of the creep test specimens were determined according to ASTM D638 Type IV [23]. The computer-aided design (CAD) data of the test specimens were created in Solidworks software. The designed data were converted into the stl file format and sent to the Ultimaker Cura (version 4.8) software to define the 3D printing parameters. The G – codes of the test specimens were created in Ultimaker Cura software. The manufacturing parameters of the test specimens determined in Ultimaker Cure are given in Table 1.

The creep test specimens were produced with the Ultimaker brand filaments with a diameter of 2.85 mm. The 3D printing parameters of the test samples were defined according to the manufacturer's technical data sheets [24] to [29]. The test samples were produced with the same G – codes and one by one in the middle of the printing table in order to produce the test samples as similar as possible. Each specimen was produced three times for the repeatable experiments.

When the samples are produced in a 3D printer, the notch effect and different wall pattern geometries

Table 1. *3D printing parameters of the test samples*

Material	Extrusion temperature [°C]	Table temperature [°C]	Printing speed [mms^{-1}]	Nozzle diameter [mm]	Layer thickness [mm]	Infill density [%]	Infill pattern
PLA [24] (Pearl-White)	200	60	60	0.4	0.2	200	Lines
ABS [25] (Yellow)	230	80	55				
Nylon [26] (Black)	245	60	45				
PC [27] (Transparent)	270	110	45				
CPE [28] (Yellow)	240	85	45				
TPLA [29] (Black)	205	60	60				

occur on the test samples. To eliminate this problem, the creep test samples were subjected to CNC milling after the 3D printing process, minimizing the notch effect and possible size and dimensional defects. The CNC milling process was completed in two steps. First, holes were drilled to connect the specimens to the creep test device. Then, 2 mm from the outer region of the creep test specimen was machined to achieve a homogeneous structure. To carry out these operations, two special drilling and milling dies were designed and produced. The produced special drilling and milling dies are seen in Fig. 1a.

Creep test specimens produced with a 3D printer for CNC milling were produced in sizes 2 mm larger than the dimensions specified in ASTM D638 Type IV. After the CNC milling process, the samples were brought to the dimensions in ASTM D638 Type IV (Fig. 1b). Four flutes milling cutter, with 6 mm diameter, were used in both drilling and milling operations. The cutting direction is defined as climb. The spindle speed is selected at 8000 rpm, and the *x*-, *y*-axis speeds are defined as 8000 mm/min.

2.2 Creep Tests

The primary purpose of this study is to determine the creep behaviour of different polymer materials produced in 3D printers with the FDM method under different temperatures and loads. Various creep tests have been carried out to achieve this aim. The experiments were performed on the standard creep test device shown in Fig. 2. As seen in the figure, two measurement devices on the creep test device measure the temperature and the amount of test sample elongation. An Etopoo brand electronic micrometer was used to measure the time-dependent creep deformations of the test samples. The micrometer can measure between 0 mm to 12.7 mm with an accuracy of 1 µm. The temperature of the test area was measured instantaneously with the PT100 temperature sensor. This sensor can measure the temperature between 80 °C and 200 °C with an accuracy of 0.1 °C. The temperature and elongation data collected over the temperature sensor and micrometer are sent to the PLC module on the creep tester. The data on the PLC module is instantly transferred to the computer environment. The data transmitted to the computer environment can be obtained in Excel format with the software of the creep test device.

Creep tests were carried out as specified in the ASTM D2990-17 [30] standard. Moreover, the creep tests were performed in a climate-controlled room and on a vibration-insulated table. The creep tests were performed for three different temperatures (25 °C, 40 °C, and 60 °C) and two various stress levels (10 MPa and 20 MPa). The temperature is set to the

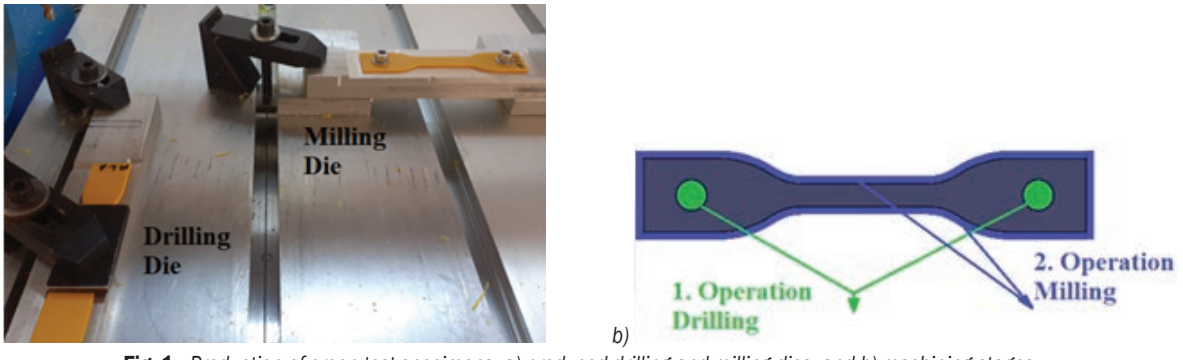

a) b)

Fig. 1. *Production of creep test specimens; a) produced drilling and milling dies, and b) machining stages*

Fig. 2. *General view of the creep test device and detailed view of the test region*

desired level in the creep tests, and the heater starts to heat the test area. When the ambient temperature reaches the desired temperature, the heater turns off. If the ambient temperature drops 1 degree below the desired temperature, the heater works again and brings the environment to the desired level. In this way, the ambient temperature is controlled with minimal fluctuations. Creep tests are started when the test zone temperature reaches equilibrium at the desired temperature. Experiments begin by lowering the protective latch, and temperature and elongation data are instantaneously collected and recorded from the computer environment. Each creep test was carried out for 3 hours (10800 s); during this time, the creep elongation was measured and recorded with a micrometer.

2 RESULTS AND DISCUSSIONS

This study performed creep tests for six different materials (ABS, PLA, TPLA, CPE, PC, and nylon) under three different temperatures and two different loading conditions. Each experiment was repeated until three successful results were obtained. The amount of elongation obtained depending on time has been interpreted by presenting different graphs. Result graphs were created by considering the test result closest to the mean for each material, temperature, and loading condition. Short-term creep behaviours (primary and secondary creep phases) of different materials are investigated in this study. Tertiary creep behaviour is also seen under specific ambient temperature and stress levels in some cases. However, this study is mainly interested in the short-term creep behaviour of different polymers.

The creep test results for ABS material for different ambient temperatures and stress levels are seen in Fig. 3 The creep characteristic's first and second stages can be seen for all tests except the 60 °C and 20 MPa case. The ABS sample ruptured quickly in approximately 3 min at 60 °C temperature and 20 MPa stress conditions. The first stage creep region extends over a longer period with the increase in temperature. In the first creep stage, the sample elongates due to the

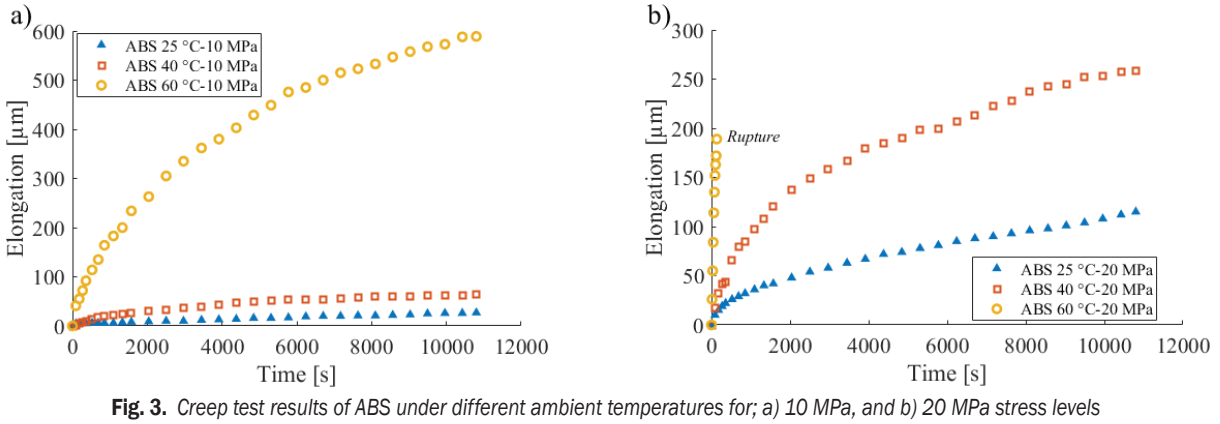

Fig. 3. *Creep test results of ABS under different ambient temperatures for; a) 10 MPa, and b) 20 MPa stress levels*

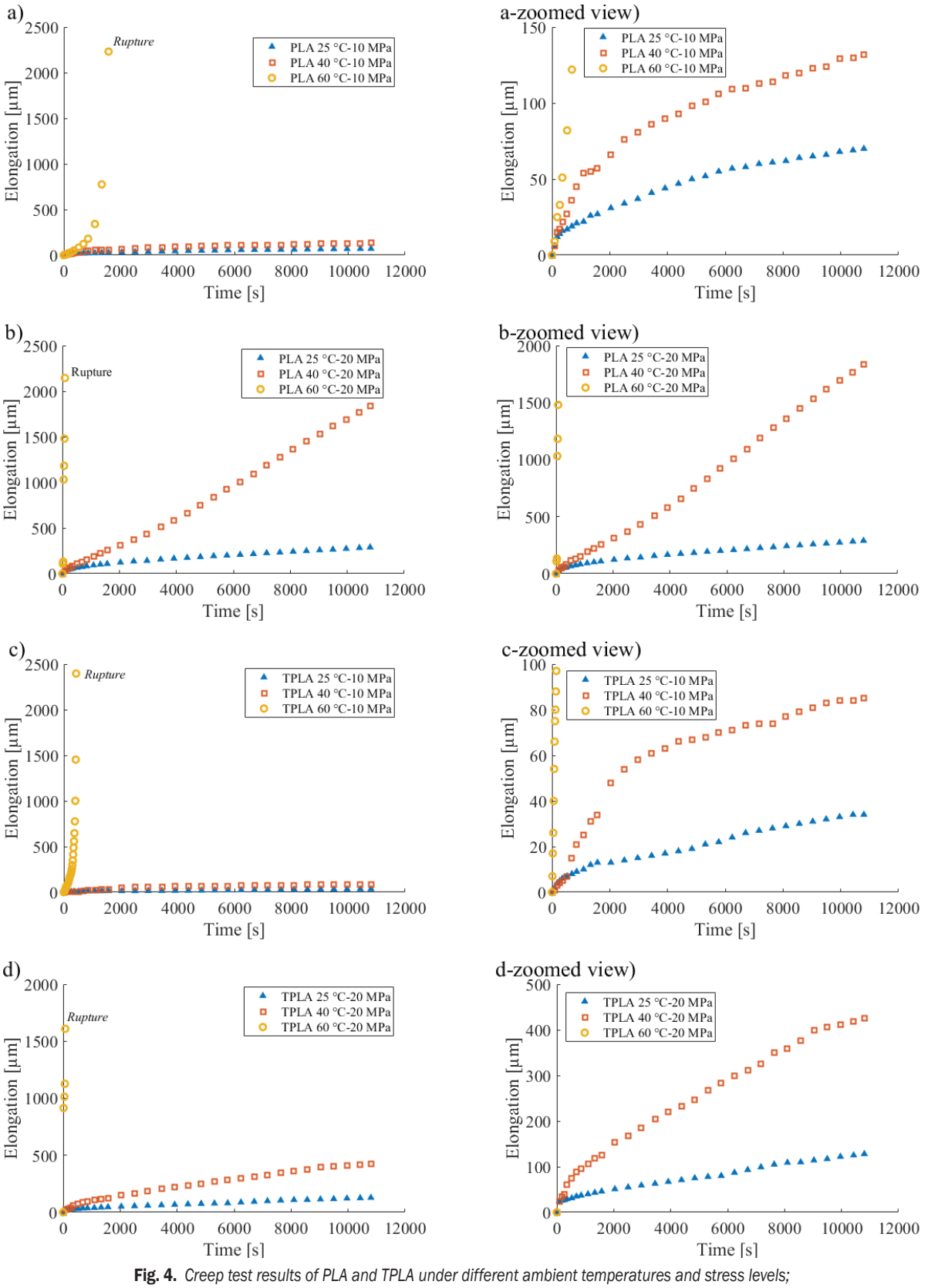

Fig. 4. *Creep test results of PLA and TPLA under different ambient temperatures and stress levels; a) 10 MPa PLA, b) 20 MPa PLA, c) 10 MPa TPLA, and d) 20 MPa TPLA (left column normal, right column zoomed views)*

effect of the load, where the dislocation movements are pretty large. As the temperature increases, the first stage creep zone expands because the ability to move on dislocations in the material increases. The creep resistance of the ABS material decreases with the increase in the ambient temperature and stress levels.

Fig. 4 indicates the creep test results for PLA and TPLA for different ambient temperatures and stress levels. As the figures are unclear at high temperatures and loads, a zoomed-in view of each figure is shown in the right column of the Fig. 4. The creep samples produced from PLA are exposed to much more creep under the same test conditions than the samples produced from ABS. It is determined that the increase in temperature and applied load reduces the creep strength of the samples produced from PLA more than ABS samples. In addition, it has been tested that the sample breaks after a while in the case of θ °C and

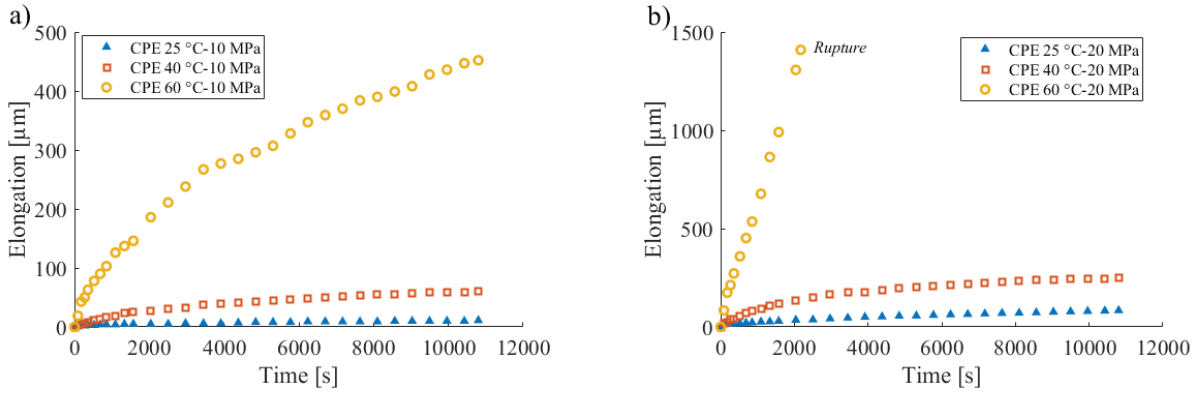

Fig. 5. *Creep test results of CPE under different ambient temperatures for; a) 10 MPa, and b) 20 MPa stress levels*

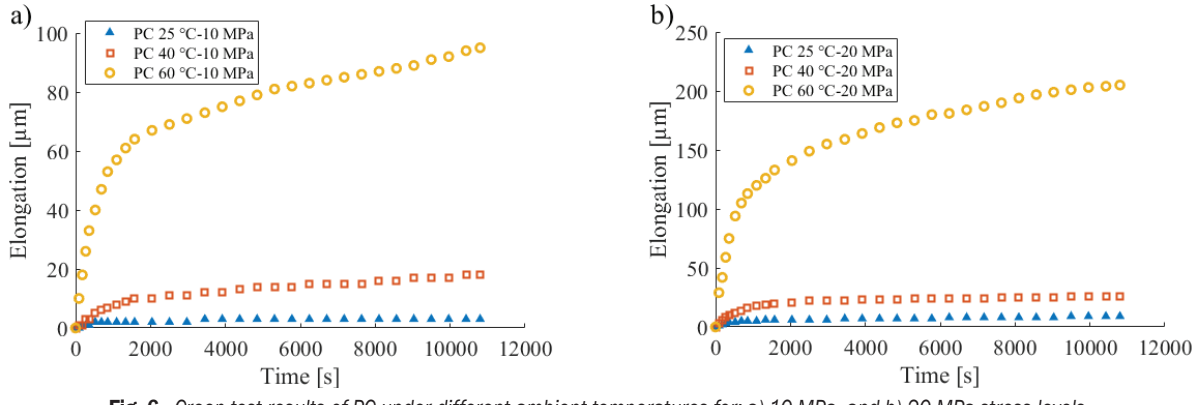

Fig. 6. *Creep test results of PC under different ambient temperatures for; a) 10 MPa, and b) 20 MPa stress levels*

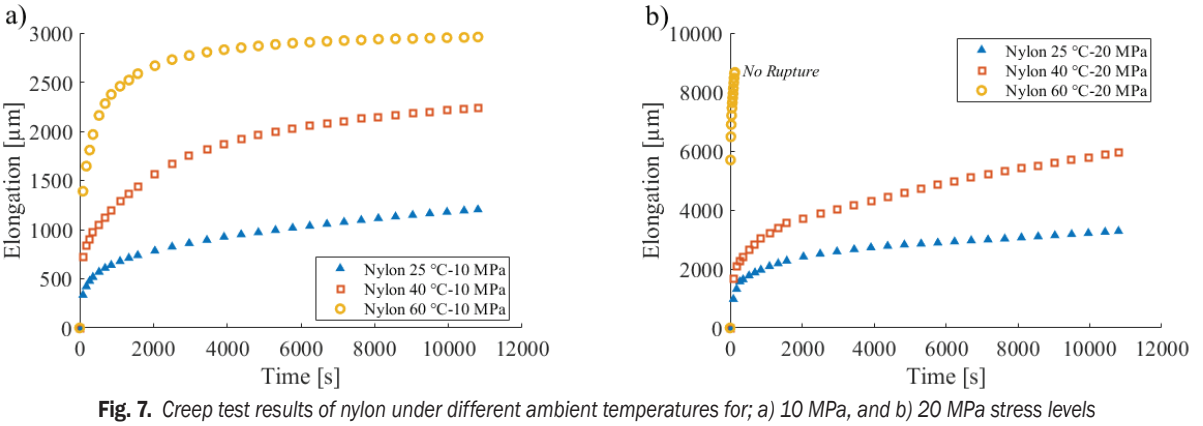

Fig. 7. *Creep test results of nylon under different ambient temperatures for; a) 10 MPa, and b) 20 MPa stress levels*

MPa. However, the time to rupture is much longer than the °C – 20 MPa case. According to the test results, although PLA is the most commonly used polymer in additive manufacturing, its creep strength is quite low. It can be said that both temperature and load significantly reduce the creep strength; therefore, parts made of PLA material are suitable for use at room temperature and very low constant loads. Similar to ABS and PLA materials, the creep increases in creep test specimens produced from TPLA with the increase in ambient temperature and load. When the total creep values are examined, the samples produced from TPLA showed less creep than PLA but more than ABS. The creep test samples were damaged quickly under both loading conditions at 60 ˚C. In short, the TPLA material has better creep strength than PLA and worse strength than ABS.

Fig. 5 illustrates the creep test results of CPE test samples under different ambient temperatures and stress levels. Similar to other materials, the creep rate of the CPE increases with the increase in the ambient temperature and stress levels. However, the creep resistance of the CPE materials is better than ABS, PLA, and TPLA. The CPE creep test samples break after a short amount of time in the case of °C and 20 MPa test conditions. This time is much longer compared to PLA, ABS, and TPLA samples. This shows that the creep strength of CPE samples is higher than PLA, ABS, and TPLA.

The creep test results of PC test samples for different ambient temperature and loading conditions are illustrated in Fig. 6 According to the results obtained from the creep tests, it has been determined that the creep strength of PC material is very high compared to all other materials. In addition, the test samples produced from PC are the least affected by temperature and loading conditions. No damage occurred in the samples produced from PC material under this study's applied loading and temperature conditions. For this reason, PC materials should be used in parts that will operate under high temperature and high constant static loading conditions since creep is very low.

The creep test results for the nylon samples are seen in Fig. 7 The first and second creep stages are clearly seen for the nylon test specimens. Because, the maximum creep values are seen for the nylon test samples. The flexibility of the nylon is much higher than the other materials. However, no damage is seen for this material, even in the case of 60 °C and 20 MPa test conditions. The experiment was terminated because it went out of the measuring range of the micrometer. Parts produced from nylon with a printer should be used in low loading and temperature conditions where flexibility is at the forefront.

The comparison of the creep test results of the five different materials under MPa stress levels and different ambient temperatures is shown in Fig. 8. The first and second stage of the creep is seen clearly from the figures; also, the tertiary (accelerated) creep phase is seen only in PLA and TPLA under °C and MPa test conditions. During the first stage of creep, the elongation rate is high. However, due to the strain

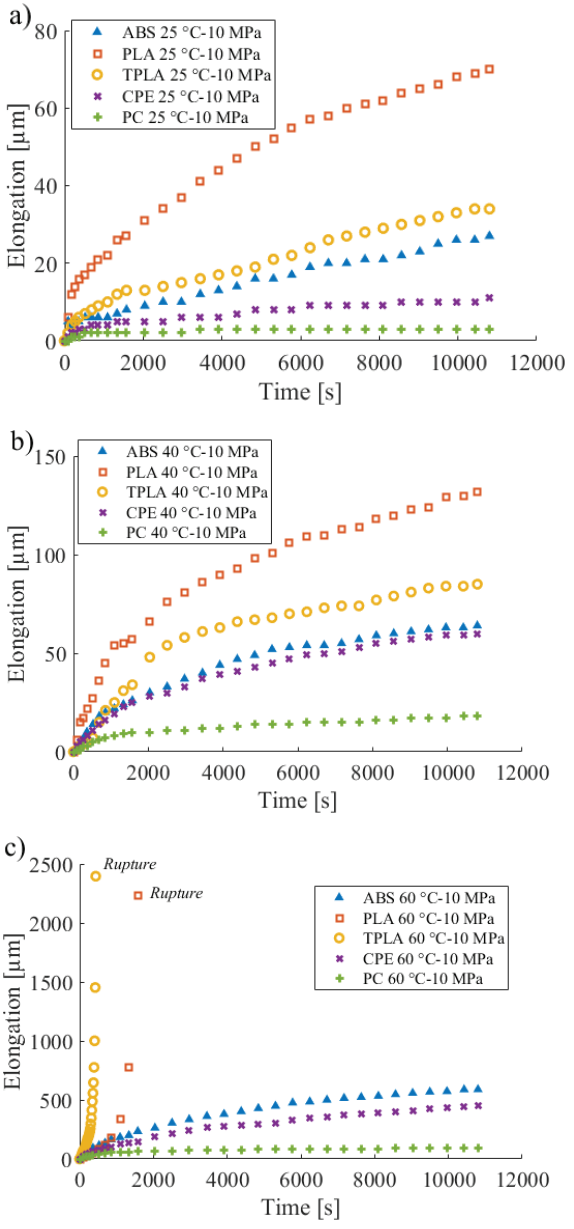

Fig. 8. *Comparison of creep test results of different materials under 10 MPa stress level and different ambient temperatures; a) 25 °C, b) 40 °C, and c) 60 °C*

hardening, the elongation rate slows down over time and reaches the lowest level, and remains constant. During the second stage of creep, the elongation increases approximately linearly with time. After the second stage creep zone, the elongation increases rapidly, and the specimens break. This region is called the creep region. The tertiary stage of creep is only seen for PLA and TPLA.

Fig. 9 shows the creep behaviour of samples produced from five different materials under 20 MPa loading and different temperatures. No rupture was observed in the experiments carried out at 25 °C and 40 °C ambient temperatures. However, in the experiments carried out at an ambient temperature of 60 °C, all other materials, except PC material, break quickly after a certain period of time. The amount of creep increases with the increase of the stress value from 10 MPa to 20 MPa. This increase in the amount of creep increases more with increasing temperature. Similar results are found in [14] to [20]. In addition, the increase in the maximum creep value increases with the increase in the stress level. Therefore, it cannot be said that there is a direct linear relationship between stress level and creep.

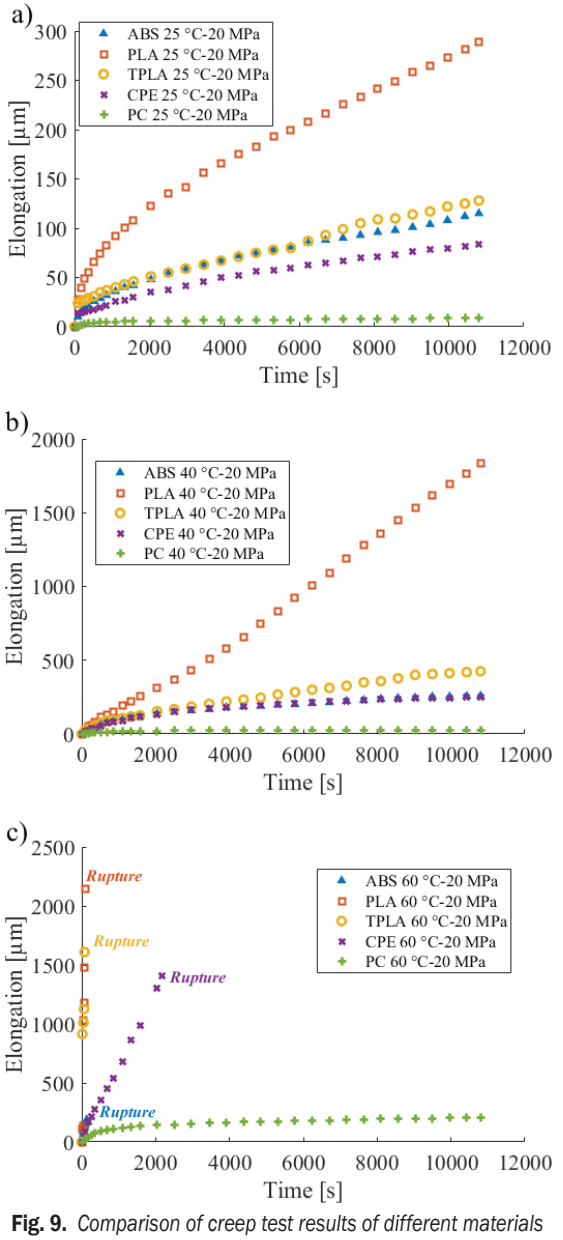

Fig. 9. *Comparison of creep test results of different materials under 20 MPa stress level and different ambient temperatures; a) 25 °C, b) 40 °C, and c) 60 °C*

3 CONCLUSIONS

In this study, the creep behaviour of test specimens produced from six different materials (PLA, ABS, TPLA, CPE, nylon, PC) by the additive manufacturing method was investigated experimentally under three different temperatures (25 °C, 40 °C, and 60 °C) and two different stress values (10 MPa, and 20 MPa). The creep test samples are produced by using Ultimaker 2+ Extended 3D printer and CNC milling to obtain a homogeneous structure. Creep experiments were carried out for three hours. The results of the creep tests performed in this study can be summarized as follows.

- The creep rate increases with the increase in ambient temperature and stress level for all materials used in this study.
- According to the test results, the load is a more effective parameter on creep than the temperature.
- PLA, which is the most commonly used polymer in 3D printers, is determined as the material with the worst creep resistance. For this reason, it is recommended that the parts produced using PLA with a 3D printer should be used at room temperature with no load or under very low static loads.
- Although TPLA has slightly better creep behaviour than PLA, it is not suitable for high temperatures and loads.
- According to the results obtained from ABS and CPE samples, these materials can be used at medium loads and moderate temperatures, but they are not suitable for use at high loads and temperatures.
- Although more creep occurred in the test specimens made of nylon compared to other materials, no rupture was observed.

- PC is determined to be the most resistant material against creep. The lowest creep amounts are observed in PC material in all experimental scenarios. Therefore, PC material can be used more safely than other materials under high load and temperature conditions.

After this study, the creep behaviour of polymer materials produced with ƀ printers can be better understood by examining the effect of ƀ printer production parameters (printing angle, nozzle diameter, layer thickness, extrusion temperature, printing speed, etc.) on creep under different temperature and loading conditions.

4 ACKNOWLEDGEMENTS

This work has been partially supported by the Scientific Research Projects Coordination Unit of the Rectorate of Kahramanmaras Sutcu Imam University with the project number 2020/7 M .

5 REFERENCES

[1] Ngo, T.D., Kashani, A., Imbalzano, G., Nguyen, K.T.Q., Hui, D. (2018). Additive manufacturing (3D printing): A review of materials, methods, applications and challenges. *Composites Part B: Engineering*, vol. 143, p. 172-196, **DOI:10.1016/j.compositesb.2018.02.012**.

[2] Beauson, J., Schillani, G., Van der Schueren, L., Goutianos, S. (2022). The effect of processing conditions and polymer crystallinity on the mechanical properties of unidirectional self-reinforced PLA composites. *Composites Part A: Applied Science and Manufacturing*, vol. 152, art. ID 106668, **DOI:10.1016/j.compositesa.2021.106668**.

[3] Saenz, F., Otarola, C., Valladares, K., Rojas, J. (2022). Influence of 3D printing settings on mechanical properties of ABS at room temperature and 77 K. *Additive Manufacturing*, vol. 39, art. ID 101841, **DOI:10.1016/j.addma.2021.101841**.

[4] Abzan, M.S., Mirzaee, R., Ahmadi, S. (2021). The correlation between morphological variations and thermo-mechanical properties of the PA6/PC/PP ternary blends: an established boundary between structures. *Polymer Testing*, vol. 93, art. ID 106930, **DOI:10.1016/j.polymertesting.2020.106930**.

[5] Fu, X., Zhang, X., Huang, Z. (2021). Axial crushing of Nylon and Al/Nylon hybrid tubes by FDM 3D printing. *Composite Structures*, vol. 256, art. ID 113055, **DOI:10.1016/j.compstruct.2020.113055**.

[6] Chen, W., Wu, K., Qu, Z., Lu, M. (2019). Intrinsic high thermal conductive co-polyester based on offset π-π stacking. *European Polymer Journal*, vol. 121, art. ID 109275, **DOI:10.1016/j.eurpolymj.2019.109275**.

[7] Hsueh, M.-H., Lai, C.-J., Chung, C.-F., Wang, S.-H., Huang, W.-C., Pan, C.-Y., Zeng, Y.-S., Hsieh, C.-H. (2021). Effect of printing parameters on the tensile properties of 3D-printed polylactic acid (PLA) based on fused deposition modeling. *Polymers*, vol. 13, no. 14, art. ID 2387, **DOI:10.3390/polym13142387**.

[8] Maqsood, N., Rimašauskas, M. (2021). Tensile and flexural response of 3D printed solid and porous CCFRPC structures and fracture ınterface study using image processing technique. *Journal of Materials Research and Technology*, vol. 14, p. 731-742, **DOI:10.1016/j.jmrt.2021.06.095**.

[9] Tezel, T., Ozenc, M., Kovan, V. (2021). Impact properties of 3D-printed engineering polymers. *Materials Today Communications*, vol. 26, art. ID 102161, **DOI:10.1016/j.mtcomm.2021.102161**.

[10] Vidakis, N., Petousis, M., Maniadi, A., Koudoumas, E., Kenanakis, G., Romanitan, C., Tutunaru, O., Suchea, M., Kechagias, J. (2020). The mechanical and physical properties of 3D-printed materials composed of ABS-Zno nanocomposites and ABS-Zno microcomposites. *Micromachines*, vol. 11, no. 6, art. ID 615, **DOI:10.3390/mi11060615**.

[11] Kamaal, M., Anas, M., Rastogi, H., Bhardwaj, N., Rahaman, A. (2020). Effect of FDM process parameters on mechanical properties of 3D-printed carbon fibre-PLA composite. *Progress in Additive Manufacturing*, vol. 6. p. 63-69, **DOI:10.1007/s40964-020-00145-3**.

[12] Safai, L., Cuellar, J.S., Smit, G., Zadpoor, A.A. (2019). A review of the fatigue behavior of 3D printed polymers. *Additive Manufacturing*, vol. 28, p. 87-97, **DOI:10.1016/j.addma.2019.03.023**.

[13] Zhang, H., Cai, L., Golub, M., Zhang, Y., Yang, X., Schlarman, K., Zhang, J. (2017). Tensile, creep, and fatigue behaviors of 3D-printed acrylonitrile butadiene styrene. *Journal of Materials Engineering and Performance*, vol. 27, p. 57-62. **DOI:10.1007/s11665-017-2961-7**.

[14] Tezel, T., Kovan, V., Topal, E.S. (2019). Effects of the printing parameters on short-term creep behaviors of three-dimensional printed polymers. *Journal of Applied Polymer Science*, vol. 136, no. 21, art. ID 47564, **DOI:10.1002/app.47564**.

[15] Mohamed, O.A., Masood, S.H., Bhowmik, J.L. (2016). Investigation on the flexural creep stiffness behavior of PC-ABS material processed by fused deposition modeling using response surface definitive screening design. *JOM*, vol. 69. p. 498-505, **DOI:10.1007/s11837-016-2228-z**.

[16] Mohamed, O.A., Masood, S.H., Bhowmik, J.L. (2017). Influence of processing parameters on creep and recovery behavior of FDM manufactured part using definitive screening design and ann. *Rapid Prototyping Journal*, vol. 23, no. 6, p. 998-1010, **DOI:10.1108/RPJ-12-2015-0198**.

[17] Al Rashid, A., Koç, M. (2021). Creep and recovery behavior of continuous fiber-reinforced 3DP composites. *Polymers*, vol. 13, no. 10, art. ID 1644, **DOI:10.3390/ polym13101644**.

[18] Waseem, M., Salah, B., Habib, T., Saleem, W., Abas, M., Khan, R., Ghani, U., Siddiqi, M. U. (2020). Multi-response optimization of tensile creep behavior of PLA 3D printed parts using categorical response surface methodology. *Polymers*, vol. 12, no. 12, art. ID 2962, **DOI:10.3390/polym12122962**.

[19] An, T., Selvaraj, R., Hong, S., Kim, N. (2017). Creep behavior of ABS polymer in temperature-humidity conditions. *Journal of Materials Engineering and Performance*, vol. 26. p. 2754-2762, **DOI:10.1007/s11665-017-2680-0**.

[20] Molina, R., Pender, G., Moro, L., Piovan, M.T. (2018). Comportamiento al creep de un polímero utilizado para

ımpresión 3D. Matéria (Rio de Janeiro), vol. 23, no. 2, **DOI:10.1590/S1517-707620180002.0412**.

[21] Lim, S.D., Rhee, J.M., Nah, C., Lee, S.-H., Lyu, M.-Y. (2004). Predicting the long-term creep behavior of plastics using the short-term creep test. *International Polymer Processing*, vol. 19, no. 3, p. 313-319, **DOI:10.3139/217.1826**.

[22] Ye, J., Yao, T., Deng, Z., Zhang, K., Dai, S., Liu, X. (2020). A modified creep model of polylactic acid (PLA-max) materials with different printing angles processed by fused filament fabrication. *Journal of Applied Polymer Science*, vol. 138, no. 17, art. ID 50270, **DOI:10.1002/app.50270**.

[23] ASTM D638-14 (2015). *Standard Test Method for Tensile Properties of Plastics*, ASTM International: West Conshohocken.

[24] Ultimaker PLA (2018). Technical datasheet from: *https://support.ultimaker.com/hc/en-us/articles/360011962720*, accessed on 2022-02-10.

[25] Ultimaker ABS (2018). Technical datasheet, from: *https://support.ultimaker.com/hc/en-us/articles/360012759139*, accessed on 2022-02-10.

[26] Ultimaker Nylon (2018). Technical datasheet, from: *https://support.ultimaker.com/hc/en-us/articles/360011962600*, accessed on 2022-02-10.

[27] Ultimaker PC (2018). Technical datasheet, from: *https://support.ultimaker.com/hc/en-us/articles/360012061159*, accessed on 2022-02-10.

[28] Ultimaker CPE (2018). Technical datasheet, from: *https://support.ultimaker.com/hc/en-us/articles/360012061099*, accessed on 2022-02-10.

[29] Ultimaker TPLA (2018). Technical datasheet, from: *https://support.ultimaker.com/hc/en-us/articles/360012759599*, accessed on 2022-02-10.

[30] ASTM D2990-17 (2017). *Standard Test Methods for Tensile, Compressive, and Flexural Creep and Creep- Rupture of Plastics*. ASTM International: West Conshohocken.

Strojniški vestnik - Journal of Mechanical Engineering 68(2022)7-8, 461-470
DOI:10.5545/sv-jme.2022.148
Original Scientific Paper
Received for review: 2022-04-06
Received revised form: 2022-06-13
Accepted for publication: 2022-06-16

Preparation and Thermal Characterization of Nanographene-Enhanced Fatty Acid-Based Solid-Liquid Organic Phase Change Material Composites for Thermal Energy Storage

Ragul Kumar Kittusamy* – Velavan Rajagopal – Paul Gregory Felix
PSG College of Technology, Department of Mechanical Engineering, India

In this research work, nano-phase change material (NPCM) composites were prepared by adding 1 %, 2 %, and 3 % mass fractions of highly conductive carbon-based graphene nanoparticles into the base phase change material (PCM). The existence and uniform graphene dispersion in the PCM was confirmed through Raman spectrometer and scanning electron microscope (SEM) analysis. The Fourier transform infrared (FTIR) and x-Ray diffraction (XRD) results showed that all three NPCM composites were chemically stable, and their crystallinity was similar to the base PCM. For the sample with 3 % graphene, the solid-state thermal conductivity was increased by 219.89 %, and liquid-state thermal conductivity was increased by 161.65 %, with a 3.52 % drop in latent heat capacity was revealed from differential scanning calorimetry (DSC) analysis. All NPCM composites have onset and peak melting temperatures closer to the base PCM. Hence, the NPCM composites can be employed for thermal energy storage (TES) integrated solar water heater (SWH) applications.

Keywords: phase change material, graphene nanoparticles, nano-phase change material composite, thermal energy storage, solar water heater

Highlights

- *Highly conductive nanographene was dispersed into the fatty acid-based PCM.*
- *The prepared NPCM composites were thermally and chemically stable.*
- *For 3 wt.% graphene in PCM, the solid-state thermal conductivity was improved by 219 %.*
- *The DSC result shows a 3.52 % decline in latent heat capacity for NPCM 3 composite.*
- *All NPCM composites have closer onset and peak melting temperatures with base PCM.*

0 INTRODUCTION

Solar energy is an essential sustainable resource since it is available in abundance. Considering the absorption and scattering losses, the total solar flux reaching the earth's surface is about 1.08 GW. Hence, the earth's surface receives 3.4 · 10^24 J of total energy annually, roughly around 7000 times the annual world primary energy use [1]. As a tropical country, India receives about 5000 trillion kWh of solar radiation annually, resulting in a daily average solar irradiance of 4 kWh/m² to 7 kWh/m². Currently, the residential sector contributes roughly about 8 % of India's total solar water heater (SWH) installations. Solar water heating is a recognized technology for cleaner hot water production from solar energy. A 100- litre SWH system can prevent up to 1.5 tonnes of CO_2 emissions each year [2].

However, the insolation of solar radiation at any point on the earth's surface is diurnal. It depends on several factors, such as weather conditions, length of the day, latitude, and season at that particular surface [3]. Therefore, it requires a technology that stores the heat energy received from the sun during sunshine hours and uses it for off-shine hours. Thermal energy storage (TES) technology is an attractive option for storing solar energy effectively to reduce the mismatch between energy supply and demand [4].

Integrating phase change material (PCM) based latent heat thermal energy storage (LHTES) in SWH is an environment-friendly solution for passively obtaining additional hot water with the same system capacity. Using PCMs in TES systems has proliferated and received tremendous attention worldwide [5] and [6]. Generally, PCMs, including organic, inorganic, and organic-inorganic categories, exhibit good potential for storing energy in the form of sensible and latent heat. The PCM-based LHTES can absorb and release substantial energy during the phase transition process at near isothermal working conditions [7].

Domestic solar water heating falls under low and medium-temperature applications with an operating temperature of around 65 °C [8]. Among the PCMs, paraffin wax was widely used for TES in SWHs, typically having a melting temperature range between 60 °C to 65 °C, a latent heat capacity of 200 kJ/kg, and a solid-state thermal conductivity of 0.21 W/(m·K) [9] to [11]. With paraffin as an energy storage medium for TES in SWHs, the maximum water temperature obtained from SWHs has been limited to 65 °C,

*Corr. Author's Address: PSG College of Technology, Peelamedu, Coimbatore, India - 641 004, ragulkumarkittusamy@gmail.com

despite the heat energy supplied to TES being at an elevated temperature. This temperature limitation is due to the heat energy stored in paraffin PCM beyond θ °C is in the form of sensible heat, which is inferior to the latent heat stored at θ °C. Using appropriate PCM with melting temperatures close to the operating temperature of SWH is necessary to obtain hot water at the desired temperature. It has been identified that the proper selection of PCM melting temperature plays a crucial role in the performance of TES systems [12]. This constitutes a research gap that could be bridged by utilizing alternative PCMs to paraffin, possessing a higher melting temperature than θ ° C.

The eutectic mixture of fatty acids offers a more comprehensive range of engineering applications because of its greater heat storage reliability [13]. Therefore, some recent studies on the synthesis and characterization of fatty acids and their eutectic mixtures reported that the fatty acid-based PCMs are a potential candidate for TES applications [14] and [15]. The fatty acid-based PCMs fall under the organic category, and they have attracted broad attention in the field of TES applications. Compared to individual fatty acid PCMs, the eutectic combinations of organic fatty acids significantly impact the phase change temperature. Any desired phase transition temperature for the TES application could be obtained by proper mixing of two or more PCMs, forming a eutectic mixture of fatty acids. For the eutectic mixture, the melting temperature of the selected PCMs should be around the desired operating temperature range such that each component in the mixture melts and solidifies simultaneously [16].

In contrast, the thermal conductivity of widely used contemporary PCMs in LHTES systems is relatively low, typically ranging from 0.5 W/(m·K) to 1 W/(m·K), which prolongs the melting and solidification process of the PCM used in TES applications. This phenomenon seriously affects the overall efficiency of the TES system. Therefore, it is necessary to address this issue with potential heat transfer enhancement techniques [17].

The inclusion of smaller mass fractions of highly conductive metallic or carbon-based nanoparticles in a PCM significantly improves the effective thermal conductivity of PCM, leading to accelerated charging and discharging rates of PCM [18]. The nanoparticles have a greater surface-area-to-volume ratio. By increasing the mass concentration of nanoparticles in the base PCM, the thermal conductivity of PCM could be improved with a decrease in the latent heat of the PCM. Hence, the mass/volume fraction of nanoparticles added to the PCM is optimized to obtain the lowest possible reduction in latent heat capacity [19].

For the previous two decades, the heat transfer enhancement in PCM-based TES applications by employing metal-based nanoparticles has been the subject of extensive research. Many researchers are currently focusing on carbon-based nano-additives (multi-wall carbon nanotubes, graphene nanoparticles, and nano-graphite) to enhance the effective thermal conductivity of PCM [20]. For the same mass fraction, metal-based nanoparticles have a higher mass-to-volume ratio when compared to carbon-based nanoparticles. Hence, this could reduce the effect of nanoparticles in PCM due to the aggregation and sinking of metal particles inside the liquid phase-change medium [21].

The use of graphene nanoparticles in energy storage and thermal management applications has been put in practice, and it outmatches metal nanoparticles, carbon-based nanotubes, and other carbon allotropes [22]. It has been proved that adding nanographene to PCM improves its thermal conductivity and, at the same time, increases the viscosity of PCM, leading to the degradation of the effect of natural convection in its liquid state. As a result, compared to pure PCM, the temperature rise rate of nano-graphene-based PCM composites was more significant during the initial stage and lowered during later stages of the charging process [23]. The higher the mass fraction of graphene in PCM, the higher the viscosity of the liquid nano-phase change material (NPCM) composite. Hence, this was a limiting factor for adding higher mass concentrations of graphene in PCM to retain the liquid state temperature rise rate of NPCM composites [24].

This study addresses the aforementioned research gaps by using a new eutectic fatty acid-based solid-liquid organic PCM and graphene nanoparticles as a thermal conductivity booster. The PCM used in this study is selected based on its melting temperature by considering the operating temperature of the domestic SWH. The main objective of this research work is to prepare and characterize the thermal properties of the NPCM composites, considering their applicability for TES integrated domestic SWHs. The appropriate use of the prepared NPCM composites and the design of the LHTES system for practical applications requires basic knowledge about the material characteristics.

1 METHODS

The research strategy followed in this work consists of three modules: material selection,

preparation of NPCM composites, and characterization of the samples.

1.1 Material Selection

The base PCM, OM65 which is a mixture of organic fatty acids, was purchased from Pluss Advanced Technologies Pvt. Ltd., Haryana, India. PCM selection was made by considering the applicability to LHTES for domestic SWHs. At room temperature, the PCM appeared to be a white flake solid. The highly conductive graphene nanoparticles were purchased from Ultrananotech Pvt. Ltd., Bangalore, India. The physical appearance of graphene was that of a light black fluffy powder. All the materials were used exactly as they were procured, with no further modifications. The suppliers' properties of PCM and nanographene are listed in Table 1.

1.2 Preparation of NPCM Composites

The NPCM composites were prepared using a two-step mechanical dispersion method [25] and [26], as illustrated in Fig. 1. The PCM was heated up to 80 °C (above its melting temperature), and the liquid PCM was stirred at 600 rpm using a hot plate magnetic stirrer. The graphene nanoparticles were then added to the liquid PCM in mass fractions of 1 wt.%, 2 wt.%, and 3 wt.% and stirred continuously for 1 hour to obtain NPCM 1, NPCM 2, and NPCM 3 samples, respectively.

Table 1. *Properties of PCM and graphene nanoparticles*

PCM (OM65)		Graphene	
Melting temperature [°C]	65	Purity [%]	> 99
Solid specific heat, 30 °C [kJ/(kg·K)]	2.83	Particle diameter [nm]	5 to 10
Latent heat [kJ/kg]	204	Length [μm]	5 to 10
Solid density, 30 °C [kg/m^3]	924	Density [g/cm^3]	3.1
Solid thermal conductivity @ 30 °C [W/(m·K)]	0.18	Surface area [m^2/g]	200 to 210
Liquid thermal conductivity @ 70 °C [W/(m·K)]	0.13	Thermal conductivity [W/(m·K)]	3000

The graphene concentration in PCM was limited to 3 wt.% by considering a minimum reduction in latent heat capacity of the NPCM composite [27]. The macro-level dispersion of nanoparticles in PCM with some agglomerated particles was obtained by shear mixing using magnetic stirring. The liquid NPCM was subjected to ultrasonication for 1 hour by maintaining water bath temperature at 80 °C and sonication frequency at 40 kHz [28]. The dispersion quality was improved by ultrasonication, thus by untangling the agglomerated graphene nanoparticles, which are collapsed by microbubbles inside the liquid medium, forming a homogeneous composite. The homogeneously dispersed liquid NPCM samples were then allowed to solidify entirely at room temperature before being collected for characterization. After complete solidification, the samples are turned into cake-like composites, subsequently ground into powder for characterization by using a polished granite mortar and pestle.

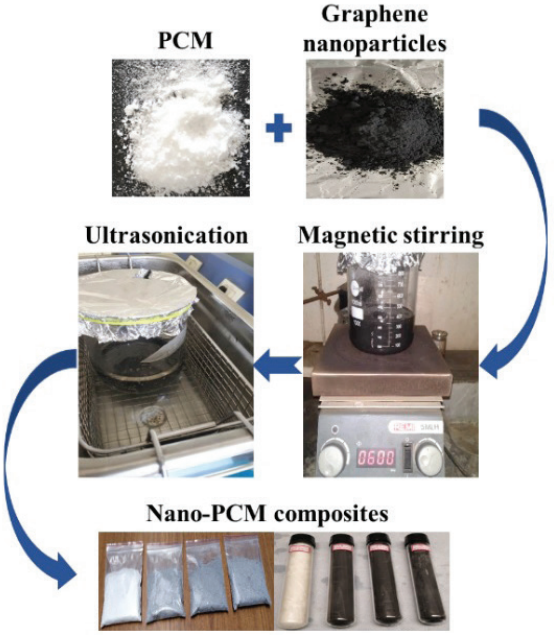

Fig. 1. *Schematic of NPCM composite preparation by the two-step method*

1.3 Characterization of the Samples

The presence of graphene in the prepared samples was identified using a WITec alpha 300 Raman spectrometer with a 532 nm argon green laser source. A scanning electron microscope (SEM) (ZEISS EVO 18 USA) with 10 kV accelerated voltage was used to examine the dispersion of graphene in PCM and the microstructures of all the prepared samples at a working distance of 10 mm. The chemical interaction between graphene nanoparticles and PCM was investigated using a Shimadzu IRAffinity 1 s model Fourier transform infrared spectrometer (FTIR) with a wavenumber range from 4000 cm^{-1} to 400 cm^{-1} and a resolution of 0.5 cm^{-1}. The Empyrean, Malvern Panalytical multipurpose X-ray diffractometer (XRD) with Cu Kα (λ = 1.54 Å) as an X-Ray source was used to study the crystal structures of PCM and NPCM

3 in the range of $0° \leq 2\theta° \leq 80°$ at a scanning rate of 6 s^{-1}. Thermal conductivities of PCM and NPCM composites were measured at solid state and liquid state using a TEMPOS thermal analyser (METER Group). The energy storage properties, such as melting temperature, latent heat capacity, and thermal decomposition temperature of PCM and NPCM composites were characterized using a NETZSCH STA 2θ0 Regulus analyser, a simultaneous differential scanning calorimetry-thermogravimetry analysis (DSC-TGA) instrument by heating the samples from θ °C to 200 °C in an alumina crucible, and in an N_2 environment at a 0 ° C/min heat ramp.

2 RESULTS AND DISCUSSION

2.1 SEM Analysis

The dispersion quality and microstructure of the prepared samples were examined through SEM. It can be seen from Fig. 2a that the graphene nanoparticles have rough flake-shaped multiple layered structures with wrinkles and wrapped edges. This characteristic feature indicates the presence of small random porous structures in graphene that can hold a small quantity of PCM in it. In comparison with the same mass concentration of metal nanoparticles, the carbon-based graphene with random void structures accommodates a smaller volume of liquid PCM, resulting in a minimum reduction in the latent heat capacity of the TES system. The typical graphene nanoparticle width was approximately 6.5 μm, indicating the graphene nanoparticles' larger aspect ratio. Fig. 2b to d shows the microstructures of NPCM 1, NPCM 2, and NPCM 3 composites comprising 1 wt.%, 2 wt.%, and 3 wt.% of the porous structured graphene nanoparticles in the base PCM. The solidified NPCM composites morphologies appear rougher, and uniformly distributed graphene in the base PCM was identified. More numerous rough protuberances were observed on the samples as the nanoparticle concentration increased, ensuring the graphene's strong embedment in crystal PCM, and establishing effective heat conduction paths within the NPCM composites [29].

2.2 Raman Spectra Analysis

A Raman spectrometer is commonly used to characterize carbon compounds because the strong Raman intensities were observed for conjugated carbon and carbon-carbon complexes [30]. The presence of graphene in all the NPCM composites was

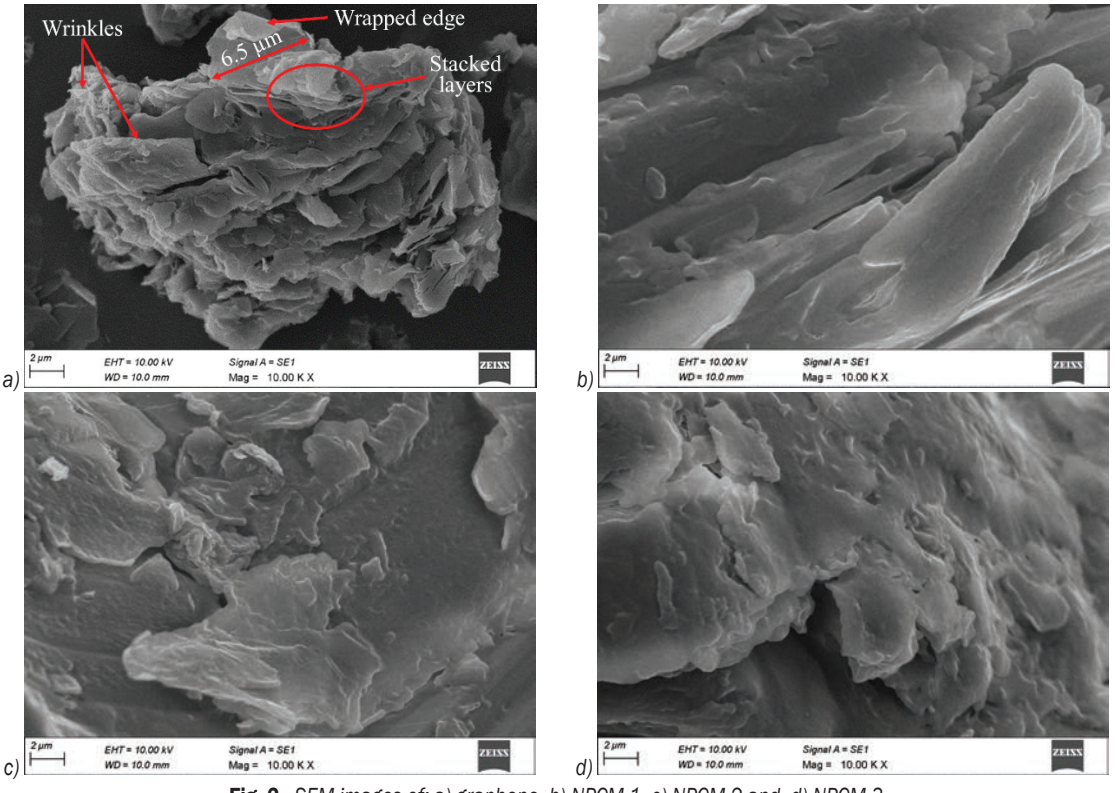

Fig. 2. *SEM images of: a) graphene, b) NPCM 1, c) NPCM 2 and, d) NPCM 3*

analysed using a Raman spectrometer, as illustrated in Fig. 3. The graphene nanoparticle shows two strong peaks: a D peak at 1357 cm^{-1} and a G peak at 1594 cm^{-1}. The D band corresponds to the sp^3 hybrid carbon atoms, the defect band whose intensity is directly related to the defect in the sample. A weak D band peak was seen for the graphene employed in this study, indicating that the graphene quality was acceptable. The G band is sharp, and the band is an in-plane vibrational mode involving the sp^2 hybridized carbon atoms contained in the graphene sheets [31]. The Raman spectrum of all three NPCM composites comprised D peak and G peak at its corresponding wavelength, as shown in Fig. 3. Thus, the presence of graphene in all NPCM composites was confirmed. The inclusion of graphene into the base PCM resulted in modifications in some spectral peaks of PCM and the formation of new characteristics in the spectra, implying that only the vibrational modes were modified due to the attachment of the graphene flakes in the chains of fatty acid PCM [32].

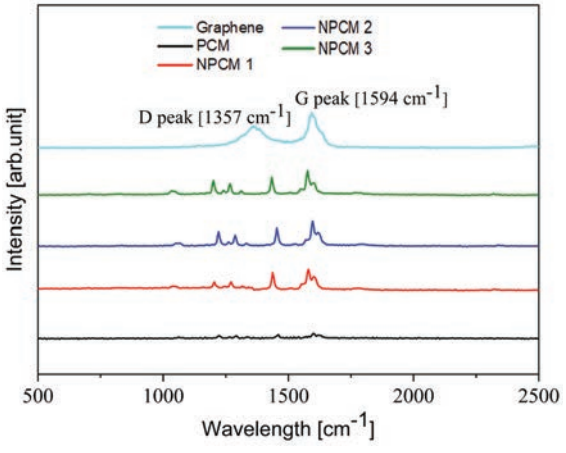

Fig. 3. *Raman spectra of graphene, PCM, and NPCM composites*

2.3 FTIR Analysis

The chemical characteristics of the fatty acid PCM, graphene nanoparticles, and NPCM composites are portrayed in Fig. 4. The peaks near 2920 cm^{-1} and 2850 cm^{-1} wavelengths indicate the stretching vibrations of the symmetric $C-H_3$ and $C-H_2-$ groups of long-chain fatty acids. The absorption band of aliphatic C–H stretching vibration generally overlaps with the absorption band of O–H stretching vibration between the wavelength 3000 cm^{-1} and 2700 cm^{-1}. The peak at 1700 cm^{-1} represents the stretching vibrations of –C=O. The peak at 1470 cm^{-1} represents the –CH_2 and the peak at 1380 cm^{-1} represents the C–H and C–C groups bending peak. It was observed that the characteristic peaks of the PCM and the NPCM composites were similar, indicating that the chemical structures of the PCM remain unchanged upon blending it with graphene nanoparticles. Therefore, all the prepared NPCM composites were in a chemically stable form.

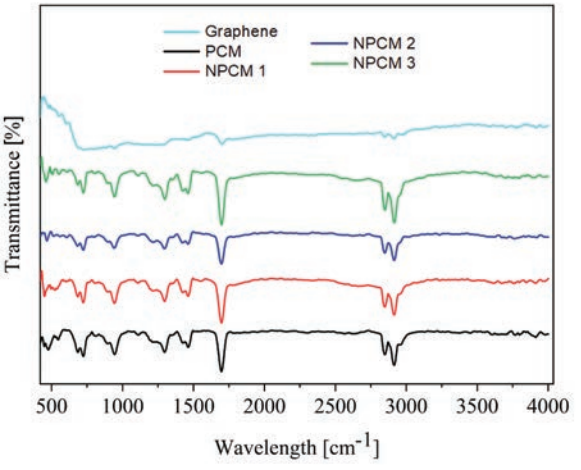

Fig. 4. *FTIR spectra of Graphene, PCM, and NPCM composites*

2.4 XRD Analysis

The PCM and NPCM 3 composite phase structure was characterized by XRD analysis. As illustrated in Fig. 5, the diffraction pattern of PCM includes two strong peaks at 21.38° and 24.02°, corresponding to the diffraction of (100) and (021) crystal planes of the fatty acid mixtures. Also, the XRD result of PCM shows a few weak diffraction peaks, such as the peak at 11.11° and 20.34°, as a result of the diffraction of (005) and (–1 1 1) crystal planes of PCM, respectively. It can be seen that the XRD pattern of the NPCM 3 composite is similar to the PCM diffraction pattern, revealing that the graphene insertion does not affect the crystal structure of the base PCM. Therefore, it was clear that the graphene-enhanced PCM composites are a mere physical mixture of PCM and graphene, and their crystal structures remained unaltered. From the above XRD results of the sample having 3 wt.% graphene (NPCM 3), it was inferred that the untested samples having 1 wt.% and 2 wt.% graphene in PCM (NPCM 1 & NPCM 2) are also a physical mixture of the PCM and the graphene.

2.5 Thermal Conductivity Measurement

The variation of solid and liquid state thermal conductivity of the PCM and the NPCM composites with change in mass fraction of the graphene

nanoparticles is shown in Fig. 6. It was observed that when the mass concentration of graphene nanoparticles increases, so does the thermal conductivity of PCM composites. The percentile increase in the thermal conductivity of the NPCM composites compared to PCM is summarized in Table 2. The solid-state thermal conductivity of the NPCM 1 composite was 0.9 W/(m·K), measured at 0 °C, with an increase of 132 % over the base PCM. The solid-state thermal conductivity of NPCM 2 and NPCM 3 composites was increased by 248 % and 299 % with 2 wt.% and 3 wt.% graphene in the base PCM. The liquid-state thermal conductivity of NPCM 1, NPCM 2, and NPCM 3 composites was enhanced by 54 %, 76 %, and 165 %, respectively, as compared to the base PCM (k_{PCM} at 70 °C is 0.13 W/(m·K)).

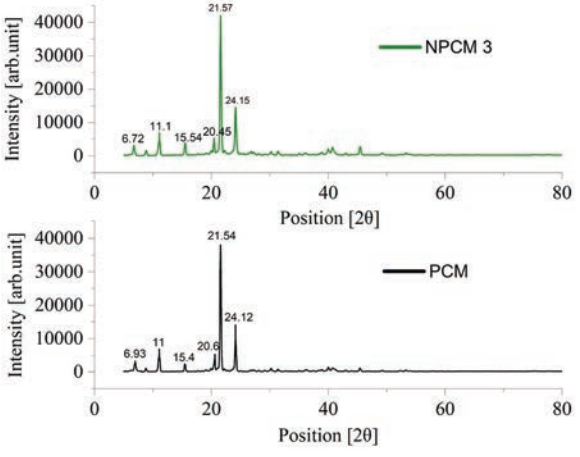

Fig. 5. *XRD patterns of PCM and NPCM 3 composite*

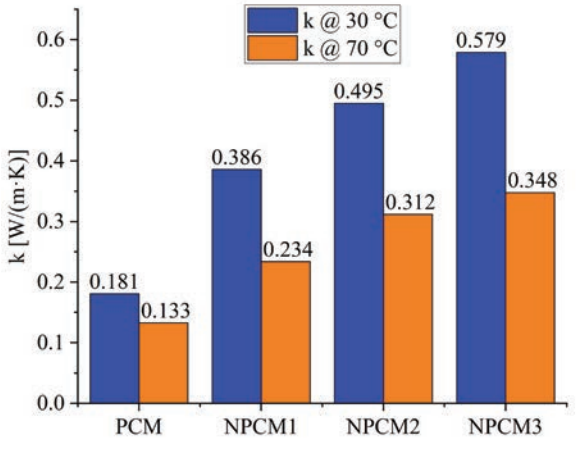

Fig. 6. *Thermal conductivity of PCM, and NPCM composites*

The percentile increase in the thermal conductivity of the NPCM composites tends to decline with a further rise in the graphene concentration. This trend was attributed to the phenomenon called agglomeration of the nanoparticles in liquid PCM [33], which occurs in NPCM composites with higher concentrations of nanoparticles. Hence, the phenomenon mentioned above was another reason for restricting the graphene mass added in PCM to 3 wt.%. With a further increase in the mass concentration of nanoparticles in PCM, there may not be a proportional improvement in the thermal conduction paths created by nanoparticles inside the NPCM composite.

2.6 DSC-TGA Analysis

Fig. 7 represents the DSC curves of PCM and NPCM composites. It was observed that the DSC curves of the NPCM composites were consistent with that of the base PCM, with a sharp solid-liquid phase transition and a modest decline in the heat flow peak for every 1 wt.% increase in the graphene concentration. Therefore, the above observation indicates that all the prepared NPCM composites were thermally stable. The latent heats of corresponding peaks were calculated by integration method considering the peaks above the baseline using NETZSCH Proteus thermal analysis software.

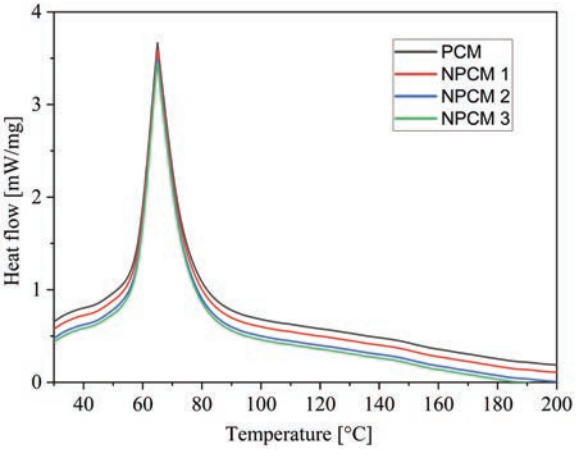

Fig. 7. *DSC curves of PCM and NPCM composites*

The DSC data of the samples are listed in Table 2. The melting latent heat capacity of the base PCM was 201.5 J/g. As expected, the latent heat capacity of NPCM composites containing graphene nanoparticles limited to 3 wt.% did not reduce much. Specifically, a reduction in the latent heat capacity of 10.8 %, 2.4 %, and 3.3 % was observed for NPCM 1, NPCM 2, and NPCM 3 composites, respectively. The small reduction in the heat storage capacity was due to the addition of nanoparticles in PCM [34]; for the same quantity

of the sample, the nanoparticles occupy some volume in place of PCM resulting in a drop in the latent heat capacity of the NPCM composites. In contrast, the phase transition curve of PCM and NPCM composites had only a single peak within the defined temperature range, and there were no indications of solid-solid secondary peaks. This observation demonstrates that the obtained PCM was in a pure form with negligible contaminants and had thermally stable phase change properties.

It was clear from the Table 2 data that the temperature that characterizes the melting was not markedly affected in the presence of nanographene in PCM. It was noted that the onset and peak melting temperatures of the PCM and NPCM composites were around 58 ˚C and 65 ˚C. This observation was a piece of significant evidence that the prepared NPCM composites could be used at the desired application temperature of 65 ˚C.

Fig. 8 depicts the TGA curve for the PCM and the NPCM composites, which shows that the mass loss has taken place in a single-step decomposition for all the samples. The steep decline curve indicates that the mass loss in PCM and NPCM composites are at very close proximities. As listed in Table 2, the onset thermal decomposition temperatures for PCM, NPCM 1, NPCM 2, and NPCM 3 composites were 185 ˚C, 194.7 ˚C, 195.4 ˚C, and 197 ˚C, respectively, which increases with an increase in the graphene mass concentration in the base PCM and follows a linear incremental trend with graphene concentration. The onset decomposition temperature for NPCM 3 composite was about 13 ˚C higher than the base PCM.

It was noticed that the onset degradation temperature of the prepared NPCM composites was higher than that of the PCM, indicating that the NPCM composites had relatively greater thermal stability. The better thermal stability of NPCM composites was linked to graphene nanoparticles' chemical inertness and its dominance in constructing the thermal barrier (i.e., retardation against the temperature) [35], which prolongs the thermal decomposition temperature of the NPCM composites. The complete decomposition of the PCM in all the NPCM composites occurs near 300 °C, whereas the graphene in NPCM 1, NPCM 2, and NPCM 3 composites remained undecomposed at this temperature. The final mass of each NPCM composite was near the initial mass of nanographene loaded in the composites.

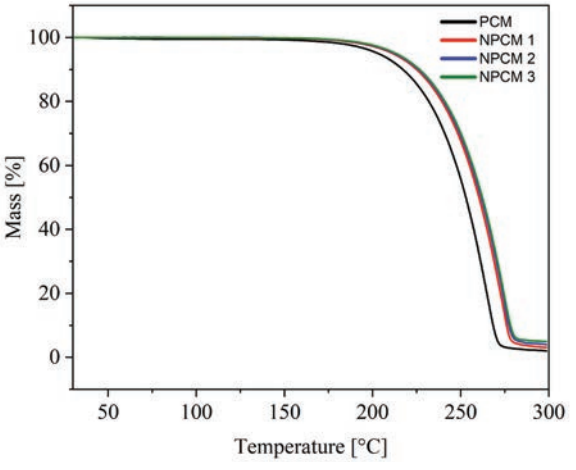

Fig. 8. *TGA curves of PCM and NPCM composites*

3 CONCLUSIONS

The experimental investigations on the thermal characterization of the prepared NPCM composites regarding its applicability for TES integrated domestic SWH have been presented in this article. The properties (i.e., microstructure, graphene presence, chemical characteristics, crystal structures, thermal conductivity) and thermal energy storage characteristics of the PCM and the NPCM composites

Table 2. *Thermal conductivity and DSC – TGA data of the PCM and the NPCM composites*

Samples	Thermal conductivity, k [W/(m·K)]		Percentage improved in k [%]		Melting onset temperature [˚C]	Melting peak temperature [˚C]	Latent heat (LH) capacity [J/g]	Percentage reduced in LH [%]	Decomposition temperature [˚C]
	Solid	Liquid	Solid	Liquid					
PCM	0.181	0.133	-	-	58.68	65.30	204.50	-	183.60
NPCM 1 (99 wt.% PCM + 1 wt.% graphene)	0.386	0.234	113.26	75.94	58.25	65.28	202.30	1.08	194.70
NPCM 2 (98 wt.% PCM + 2 wt.% graphene)	0.495	0.312	173.48	134.59	58.00	65.15	199.60	2.40	195.40
NPCM 3 (97 wt.% PCM + 3 wt.% graphene)	0.579	0.348	219.89	161.65	57.87	65.11	197.30	3.52	197.00

were investigated using their respective instruments. The key findings are summarized as follows:

1 The homogeneous dispersion of graphene and rougher protuberance in NPCM composites was observed via SEM analysis, ensuring the acceptable dispersion and strong embedment of graphene in PCM forms additional heat conduction paths inside the PCM network.

2. The presence of graphene in all the NPCM composites was confirmed using a Raman spectrometer.

3 The FTIR and XRD analysis results confirmed that the addition of nanographene does not affect the chemical structures and crystal structure of the base PCM, meaning that the PCM and nanographene in NPCM composites have only a physical connection where the graphene acts as a thermal conductivity enhancer.

4 Every 1 wt.% increase in graphene content in PCM resulted in a notable increase in the thermal conductivity of the prepared NPCM composites.

5 According to DSC analysis, the prepared NPCM composites had melting characteristics similar to the base PCM. The onset and peak melting temperatures for all the samples were around 66 ˚C and 73 ˚C, respectively, demonstrating that the selected PCM and NPCM composites would be ideal for the proposed application's temperature requirement.

6 Compared to the base PCM, there was a significant increase in the thermal conductivity of 299 % and 66 % in the solid and liquid states, respectively, and an insignificant drop in latent heat capacity of about 3.2 % was noted for the NPCM 3 composite. The significant increase in thermal conductivity of NPCM composites overshadows the minor decrease in their latent heat capacity.

7 The TG analysis demonstrated that the temperature at which the NPCM composites began to decompose increased linearly with increasing graphene mass fraction in the PCM. All the NPCM composites showed greater thermal stability when compared to the PCM because chemically inert graphene in NPCM composites had acted as a thermal barrier, increasing the thermal degradation temperature of the NPCM composites.

The investigations mentioned above demonstrate that the dispersion of the graphene nanoparticles in the fatty acid-based PCM is a viable option for increasing the PCM's thermal conductivity. Due to the increased thermal conductivity of the NPCM composites, the rate of melting and solidification during charging and discharging cycles could be accelerated, and this phenomenon could improve the overall performance of the NPCM-based LHTES system. Therefore, the proposed NPCM composites could be the best alternative to the conventional paraffin wax PCM for TES-integrated domestic SWHs.

The TES integrated SWH system could completely melt the NPCM composites faster than the base PCM with the available solar energy. For the maximum utilization of the available solar energy, the NPCM-based TES system's volume capacity could be increased, as the charging duration is reduced, allowing a greater quantity of NPCMs to be used. As a result, the maximum potential of latent heat capacity of NPCMs could be utilized to store additional thermal energy in it. From the application perspective, this advantage would enable the SWHs to deliver additional hot water at the desired temperature. However, the envisaged application of the proposed NPCM composites is not limited to TES integrated SWHs, they could also potentially be employed for TES integrated low-temperature waste heat recovery, and electronic thermal management applications.

Furthermore, to ascertain the thermal behaviour of the NPCMs in the longer run, performing accelerated thermal cycling tests is required. Also, to investigate the real-time behaviour of the NPCMs from an SWH perspective, it is necessary to conduct intricate studies with solar thermal energy.

4 ACKNOWLEDGEMENTS

The authors gratefully acknowledge the financial support provided by the All-India Council for Technical Education (AICTE) under AICTE Doctoral Fellowship (ADF) scheme. The authors would also like to thank PSG College of Technology, and PSG Institute of Advanced Studies, Coimbatore for providing research facilities and other support.

8 REFERENCES

[1] Wray, P. (2008). Solar power. *American Ceramic Society Bulletin*, vol. 87, no. 7, p. 31-33, **DOI:10.1016/B978-0-08-102631-1.00013-4**.

[2] Singh, S., Anand, A., Shukla, A., Sharma, A. (2021). Environmental, technical and financial feasibility study of domestic solar water heating system in India. *Sustainable Energy Technologies and Assessments*, vol. 43, art. ID 100965, **DOI:10.1016/j.seta.2020.100965**.

[3] Pan, T., Wu, S., Dai; E., Liu.Y. (2013). Estimating the daily global solar radiation spatial distribution from diurnal temperature

ranges over the tibetan plateau in China. *Applied Energy*, vol. 107, p. 384-393, **DOI:10.1016/j.apenergy.2013.02.053**.

[4] Cabeza, L.F. (2012). Thermal energy storage. *Comprehensive Renewable Energy*, vol. 3, p. 211-253, **DOI:10.1016/B978-0-08-087872-0.00307-3**.

[5] Ho, C.J., Gao,J.Y. (2009). Preparation and thermophysical properties of nanoparticle-in-paraffin emulsion as phase change material. *International Communications in Heat and Mass Transfer*, vol. 36, no. 5, p. 467-470, **DOI:10.1016/j.icheatmasstransfer.2009.01.015**.

[6] Ma, G., Sun, J., Zhang, Y., Jing, Y., Jia, Y. (2019). A novel low-temperature phase change material based on stearic acid and hexanamide eutectic mixture for thermal energy storage. *Chemical Physics Letters*, vol. 714, p. 166-171, **DOI:10.1016/j.cplett.2018.11.003**.

[7] Sari, A. (2012). Thermal energy storage properties of mannitol-fatty acid esters as novel organic solid-liquid phase change materials. *Energy Conversion and Management*, vol. 64, p. 68-78, **DOI:10.1016/j.enconman.2012.07.003**.

[8] Zsembinszki, G., Fernández, A.G., Cabeza, L.F. (2020). Selection of the appropriate phase change material for two innovative compact energy storage systems in residential buildings. *Applied Sciences*, vol. 10, no. 6, art. ID 2116, **DOI:10.3390/app10062116**.

[9] Fazilati, M.A., Alemrajabi, A.A. (2013). Phase change material for enhancing solar water heater, an experimental approach. *Energy Conversion and Management*, vol. 71, p. 138-145, **DOI:10.1016/j.enconman.2013.03.034**.

[10] Al-Kayiem, H.H. Lin, S.C. (2014). Performance evaluation of a solar water heater integrated with a PCM nanocomposite TES at various inclinations. *Solar Energy*, vol. 109, p. 82-92, **DOI:10.1016/j.solener.2014.08.021**.

[11] Mandal, S.K., Kumar, S., Singh, P.K., Mishra, S.K., Bishwakarma, H., Choudhry, N.P., Nayak, R.K., Das, A.K. (2019). Performance investigation of CuO-paraffin wax nanocomposite in solar water heater during night. *Thermochimica Acta*, vol. 671, p. 36-42, **DOI:10.1016/J.tca.2018.11.003**.

[12] Zavrl, E., Zupanc, G., Stritih, U., & Dovjak, M. (2020). Overheating reduction in lightweight framed buildings with application of phase change materials. *Strojniski vestnik - Journal of Mechanical Engineering*, vol. 66, no. 1, p. 3-14, **DOI:10.5545/sv-jme.2019.6244**.

[13] Yuan, Y., Zhang, N., Tao, W., Cao, X., He, Y. (2014). Fatty acids as phase change materials: A review. *Renewable and Sustainable Energy Reviews*, vol. 29, p. 482-498, **DOI:10.1016/j.rser.2013.08.107**.

[14] Duquesne, M., Mailhé, C., Doppiu, S., Dauvergne, J.L., Santos-Moreno, S., Godin, A., Fleury, G., Rouault, F., Del Barrio, E.P.. (2021). Characterization of fatty acids as biobased organic materials for latent heat storage. *Materials*, vol. 14, no. 16, art. ID 4707, **DOI:10.3390/ma14164707**.

[15] B, E.J., A, V.A.. (2020). Characterisation and stability analysis of eutectic fatty acid as a low cost cold energy storage phase change material. *Journal of Energy Storage*, vol. 31, srt. Id 101708, **DOI:10.1016/j.est.2020.101708**.

[16] Narayanan, S.S., Kardam, A:, Kumar, V., Bhardwaj, N., Madhwal, D., Shukla, P., Kumar, A., Verma, A., Jain, V.K. (2017). Development of sunlight-driven eutectic phase change material nanocomposite for applications in solar water heating. *Resource-Efficient Technologies*, vol. 3, no. 3, p. 272-279, **DOI:10.1016/j.reffit.2016.12.004**.

[17] Ling, Z., Chen, J., Xu, T., Fang, X., Gao, X:, Zhang, Z. (2015). Thermal conductivity of an organic phase change material/expanded graphite composite across the phase change temperature range and a novel thermal conductivity model. *Energy Conversion and Management*, vol. 102, p. 202-208, **DOI:10.1016/j.enconman.2014.11.040**.

[18] Shah, K.W.. (2018). A review on enhancement of phase change materials - A nanomaterials perspective. *Energy and Buildings*, vol. 175, p. 57-68, **DOI:10.1016/j.enbuild.2018.06.043**.

[19] Kibria, M.A., Anisur, M.R., Mahfuz, M.H., Saidur, R., Metselaar, I.H.S.C. (2015). A review on thermophysical properties of nanoparticle dispersed phase change materials. *Energy Conversion and Management*, vol. 95, p. 69-89, **DOI:10.1016/j.enconman.2015.02.028**.

[20] Fan, L.W., Fang, X., Wang, X., Zeng, Y., Xiao, Y.Q., Yu, Z.T., Xu, X., Hu, Y.C., Cen, K.F. (2013). Effects of various carbon nanofillers on the thermal conductivity and energy storage properties of paraffin-based nanocomposite phase change materials. *Applied Energy*, vol. 110, p. 163-172, **DOI:10.1016/J.apenergy.2013.04.043**.

[21] Qureshi, Z.A., Ali, H.M., Khushnood, S. (2018). Recent advances on thermal conductivity enhancement of phase change materials for energy storage system: A review. *International Journal of Heat and Mass Transfer*, vol. 127, p. 838-856, **DOI:10.1016/j.ijheatmasstransfer.2018.08.049**.

[22] Renteria; J.D., Nika, D.L., Alexander A. Balandin, A.A. (2014). Graphene thermal properties: Applications in thermal management and energy storage. *Applied Sciences*, vol. 4, no. 4, p. 525-547, **DOI:10.3390/app4040525**.

[23] Zeng, Y., Fan, L.W., Xiao, Y.Q., Yu, Z.T., Cen, K.F. (2013). An experimental investigation of melting of nanoparticle-enhanced phase change materials (NePCMs) in a bottom-heated vertical cylindrical cavity. *International Journal of Heat and Mass Transfer*, vol. 66, p. 111-117, **DOI:10.1016/j.ijheatmasstransfer.2013.07.022**.

[24] Zou, D., Ma, X., Liu, X., Zheng, P., Hu, Y. (2018). Thermal performance enhancement of composite phase change materials (PCM) using graphene and carbon nanotubes as additives for the potential application in lithium-ion power battery. *International Journal of Heat and Mass Transfer*, vol. 120, p. 33-41, **DOI:10.1016/j.ijheatmasstransfer.2017.12.024**.

[25] Xiang, J., Drzal, L.T. (2011). Investigation of exfoliated graphite nanoplatelets (xGnP) in improving thermal conductivity of paraffin wax-based phase change material. *Solar Energy Materials and Solar Cells*, vol. 95, no. 7, p. 1811-1818, **DOI:10.1016/j.solmat.2011.01.048**.

[26] Kim, S.C., Prabakaran, R., Sakthivadivel, D:, Thangapandian, N., Bhatia, A., Kumar, P.G. (2020). Thermal transport properties of carbon-assisted phase change nanocomposite. *Fullerenes Nanotubes and Carbon Nanostructures*, vol. 28, no. 11, p. 925-933, **DOI:10.1080/1536383X.2020.1786814**.

[27] Ali, M.A., Fayaz, Viegas, R.F., Kumar, M.B.S., Kannapiran, R.K., Feroskhan, M. (2019). Enhancement of heat transfer in paraffin wax PCM using nano graphene composite for

industrial helmets. *Journal of Energy Storage*, vol. 26, art. ID 100982, **DOI:10.1016/j.est.2019.100982**.

[28] Harikrishnan, S., Kalaiselvam, S. (2012). Preparation and thermal characteristics of CuO-oleic acid nanofluids as a phase change material. *Thermochimica Acta*, vol. 533, p. 46-55, **DOI:10.1016/j.tca.2012.01.018**.

[29] Singh, N.P., Gupta, V.K., Singh, A.P., Sapra, B. (2021). Synergistic effects of graphene nanoplatelets and NH2-MWCNTs on cryogenic mechanical properties of epoxy nanocomposites. *Polymer Testing*, vol. 94, art. ID 107032, **DOI:10.1016/j.polymertesting.2020.107032**.

[30] Zhang, L., Zhang, P., Wang, F., Kang, M., Li, R., Mou, Y., Huang, Y. (2016). Phase change materials based on polyethylene glycol supported by graphene-based mesoporous silica sheets. *Applied Thermal Engineering*, vol. 101, p. 217-223, **DOI:10.1016/j.applthermaleng.2016.02.120**.

[31] Lin, Y:, Zhu, C., Fang, G. (2019). Synthesis and properties of microencapsulated stearic acid/silica composites with graphene oxide for improving thermal conductivity as novel solar thermal storage materials. *Solar Energy Materials and Solar Cells*, vol. 189, p. 197-205, **DOI:10.1016/j.solmat.2018.10.005**.

[32] Goli, P., Legedza, S., Dhar, A., Salgado, R., Renteria, J., Balandin, A.A.. (2014). Graphene-enhanced hybrid phase change materials for thermal management of Li-ion batteries. *Journal of Power Sources*, vol. 248, p. 37-43, **DOI:10.1016/j.jpowsour.2013.08.135**.

[33] Wu, S.Y., Wang, H., Xiao, S., Zhu, D.S. (2012). An investigation of melting/freezing characteristics of nanoparticle-enhanced phase change materials. *Journal of Thermal Analysis and Calorimetry*, vol. 110, p. 1127-1131, **DOI:10.1007/s10973-011-2080-x**.

[34] Liu, P., Gu, X., Rao, J., Liu, S., Wang, B., Bian, L. (2020). Preparation and thermal properties of lauric acid/raw fly ash/carbon nanotubes composite as phase change material for thermal energy storage. *Fullerenes Nanotubes and Carbon Nanostructures*, vol. 28, no. 11, p. 934-944, **DOI:10.1080/1536383X.2020.1786815**.

[35] George, M., Pandey, A.K., Rahim, N.A., Tyagi, V.V., Shahabuddin, S., Saidur, R. (2020). A novel polyaniline (PANI)/ paraffin wax nano composite phase change material: Superior transition heat storage capacity, thermal conductivity and thermal reliability. *Solar Energy*, vol. 204, p. 448-458, **DOI:10.1016/j.solener.2020.04.087**.

Strojniški vestnik - Journal of Mechanical Engineering 68(2022)7-8, 471-484
DOI:10.5545/sv-jme.2022.84
Original Scientific Paper
Received for review: 2022-02-22
Received revised form: 2022-04-29
Accepted for publication: 2022-05-12

Optimization of in-Vehicle Carbon Dioxide Level in a 5-Seat Car

Prabhakaran Jayasankar*–Jayabal Subbaian
Government College of Engineering, Department of Mechanical Engineering, India

The air quality in a car's cabin can be five times worse than that of residential and non-residential buildings, resulting in a variety of health issues, such as headache, sore throat, and nausea, which are all symptoms of in-vehicle air pollution. The monitoring of carbon dioxide, which is one of the principal pollutants in car cabins, is required before regulating it. The current research is focused on the recording of carbon dioxide levels for different levels of human load, air speed, and temperature. A statistical analysis and plots were obtained for recorded responses to determine air quality parameters for a minimum value of carbon dioxide level in a five-seat car cabin. Three algorithms (generalized reduced gradient (GRG), response surface methodology (RSM), and genetic algorithm (GA)) were successfully used in a 5-seat car to optimize the in-vehicle carbon dioxide level. The GRG method provided the minimum carbon dioxide level of 471.531 ppm for a one-human load at an air speed of 2 m/s and a temperature of 24 °C. For varying human loads of 2,3,4, and 5, the GRG and GA methods provided carbon dioxide levels of 508.785 ppm, 580.722 ppm, 659.839 ppm and 769.016 ppm, respectively. Comparing all three techniques, the RSM provided carbon dioxide levels of 471.876 ppm, 508.865 ppm, 580.79 ppm, 659.905 ppm, and 769.362 ppm for human loads of 1, 2, 3, 4, and 5, respectively. This study will provide a platform for the researchers working on indoor air quality characteristics to apply soft computing techniques effectively for the evaluation of comfortable healthy environments and for the benefit of the passengers in car cabins.
Keywords: carbon dioxide, five-seat car, genetic algorithm, in-vehicle air quality, response surface methodology

Highlights
- *Carbon dioxide level for varying human loads, air speeds, and temperatures in a 5-seat car are studied.*
- *Influence of air quality parameter on response is studied with the help of ANOVA and statistical plots.*
- *Statistical analysis and regression equation are developed for the prediction of carbon dioxide levels.*
- *Air quality characteristics for minimum values of response are obtained through familiar optimization algorithms.*

0 INTRODUCTION

Human beings spend almost θ % to θ % of their time in confined spaces [1], such as houses, workplaces, classrooms, shopping malls, and theatres, as well as vehicles like cars. As a result, the indoor air quality (IAQ) of living spaces has become a matter of concern. The in-vehicle air quality (IVAQ) of automobiles, where pollution levels are much higher than the living indoor environments [2] to [4] is one such occupied space that has not been studied. The need for optimal indoor environmental quality (IEQ) is especially vital in all living and working places with vulnerable populations [5]. This is an area that needs to be seriously researched and studied to ensure better in-vehicle air quality for the passengers. Particulate matter (PM), carbon dioxide (CO_2), carbon monoxide (CO), volatile organic compounds (VOCs), and other pollutants impair the IVAQ of the cabins. People employ varying degrees of temperature, velocity, and air-circulation modes for their preferences while commuting in a car with an air-conditioning system, without realizing the deleterious repercussions of those settings. The levels of pollutant concentration have higher values in indoor environments that use mechanical ventilation compared to natural ventilation [6]. These factors may lead to an increase in PM, the particle-health correlation has been thoroughly investigated and found to be both valid and confirmatory [7]. The carbon dioxide concentrations within inhabited living spaces are more than such concentrations outdoors, as people generate and exhale CO_2.

The levels of the indoor-outdoor CO_2 concentration differential grow as the ventilation rate (i.e., supply of fresh air into the house) per individual reduces [8], As a result of the limited and closed aspect of public transit, contaminants accumulate and lead to rises in concentrations [9]. There is no major change in indoor CO_2 levels with changes in the average outdoor temperature [10]. There are a few factors that lead to the increase in cabin CO_2 levels. Various ventilation fan speeds may lead to variations in cabin CO_2 concentrations [11]. The month of the year when testing is being conducted will also have a significant impact on CO_2 levels in vehicles [12]. When the mode of travel is a subway rather than normal open roads the concentration levels will be high [13]. The CO_2 that the inhabitants breathe enters their bloodstream and creates respiratory problems, harms their health, and even leads to premature deaths [14] and [15]. This not only affects human health; it also triggers nutrition imbalances in plants that are exposed to higher levels of CO_2 [16]. As the amount of CO_2 inside the vehicle

*Corr. Author's Address: Government College of Engineering, Department of Mechanical Engineering, India , jpkn006@gmail.com

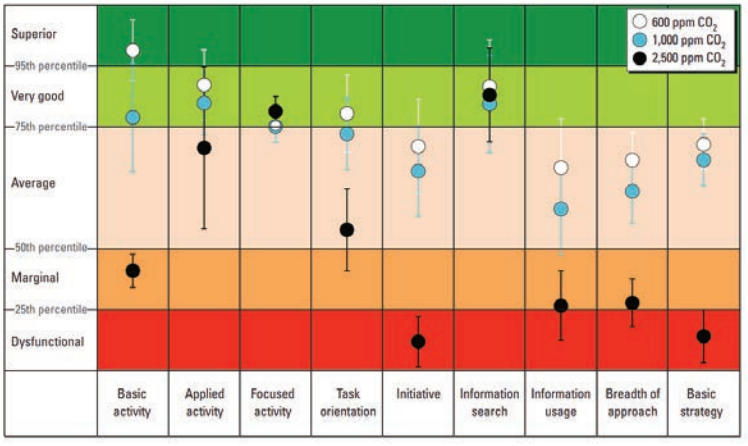

Fig. 1. *CO_2's effect on human decision-making*

cabin rises, so does the danger of an accident caused by the driver's tiredness and reduced agility [17]. Fig. 1 sourced from the research article documented by Satish et al. [18] shows the influence of the increase in CO_2 levels in human decision making.

CO_2 is a widely used and practical metric for determining air quality [19]. As of September 2021 [20], the worldwide average ambient CO_2 concentration level was at 419 ppm. The permissible amounts of CO_2 in air-conditioned space for human beings are defined by ASHRAE Standard-62 [21]. According to ASHRAE (American Society of Heating, Refrigerating, and Air-Conditioning Engineers), the maximum CO_2 level limit is 700 ppm over ambient surroundings continuously. Even though the value does not apply to CO_2 levels inside cars, it is still significant because a car is a confined space. In comparison to other small environments, automobile exposure is more difficult to comprehend because it is influenced by several interconnected factors, such as ventilation, motorway type, vehicle type, and self-pollution [22].

Many strategies are used to improve the IAQ for the inhabitants, and many researchers [23] and [24] have sought to optimise heating, ventilation, and air-conditioning (HVAC) systems for indoor conditions. Researchers have proved that productivity has a significant relationship with indoor air quality [25]. Different monitoring techniques should be applied for natural and mechanical ventilation, as both have different characteristics [26]. Prior research in IVAQ optimization has been documented, but the optimization of input parameters for the vehicle cabin to minimize CO_2 levels concerning occupants in a subcompact car is very limited. In this article, algorithms were used for optimization.

1 EXPERIMENTS

1.1 Air Quality Parameters and their Characteristics

In the modelling process, some parameters gathered are irrelevant or redundant. As a result, before constructing the predictive model, parameter selection is critical. In data mining, the availability of irrelevant or redundant parameters can obscure primary patterns [27], As a result, before beginning an experiment, identifying the right parameters is essential. On indoor air quality metrics, the Environmental Protection Agency (EPA), ASHRAE, and Leadership in Energy and Environmental Design (LEED) are all interrelated. The conditions for a healthy environment of particulate matter are 10 micrometres or less in diameter of 150 µg/m³ and 2.5 micrometres or less in diameter of 35 µg/m³. The humidity is below 60 %, ideally ranging from 30 % to 60 % (EPA). CO concentration should be less than 9 ppm and CO_2 is about 700 ppm above open-air air levels, and it is about 1000 ppm to 2100 ppm, and the temperature is 20.3 °C to 23.3 °C in winter and 23.9 °C to 26.9 C in summer (ASHRAE). The air quality parameters, such as air speed and temperature, were varied at different levels for varying human loads and CO_2 characteristics were measured accordingly.

1.2 Assumptions

To avoid ambiguity and maintain a regulated atmosphere inside the vehicle, the following assumptions were made, and similar ones were proposed to be applicable by Thirumal et al. [28] for optimizing IAQ characteristics using a multi-objective genetic algorithm.

- When the car's doors were closed, the leak is negligible. The air-conditioning is set in fresh air supply mode.
- The CO_2 may vary based on location and environmental conditions. Within the car, volatile organic component pollutants are not present.
- Before beginning the experiment, the indoor regulated space is allowed to reach equilibrium with the outdoor circumstances.
- Pollen, dander, dust solids, and particulate matter are not considered.
- Tobacco smoking, dust particles, and further unknown elements are not present in the space.
- The fan motor's input current and air speed will change when the engine rpm changes. Hence, the average air speeds were approximated as (1, 2, 3, 4, 5, 6, 7, 8, and 9) m/s.

1.3 Experimental Set-Up

1.3.1 Description of Locale

The assessment was recorded in an important roadway of the Karaikudi municipality, which is the 20th highest urban accumulation of Tamilnadu with a population of 106,464 (2011 census survey data). It is a heritage town situated in Sivagangai District, Tamilnadu, India. Fig. 2 shows the location of the town. This place can be accessible by the Tiruchirappalli–Rameswaram highway that passes through Karaikudi. This locus is located at 10.07° N latitude and 78° E longitude. The average maximum temperature is about 34° C (~93° F), and the average lowest temperature is about 24° C (~75° F); the twelve-monthly middling rainfall in Karaikudi is about 920 millimetres, the topography of the place is predominantly flat and some gravel areas are also found in the surroundings. The area of the municipality is about 33 km^2.

1.3.2 Measurements

To measure in-vehicle carbon dioxide concentration a portable IAQ CO_2 meter, the Extech device (Model CO20) by FLIR commercial systems Inc., USA, has been utilized. A similar experimental setup and equipment were used by Ayyakkannu et al. [29] for measuring in-vehicle pollutants. This measuring device works with the theory of the non-dispersive infrared (NDIR) technique. The device can assess up to a maximum range of 5000 ppm with 1 ppm resolution. The device was positioned in the centre of the car cabin at breathing level. The instrument was

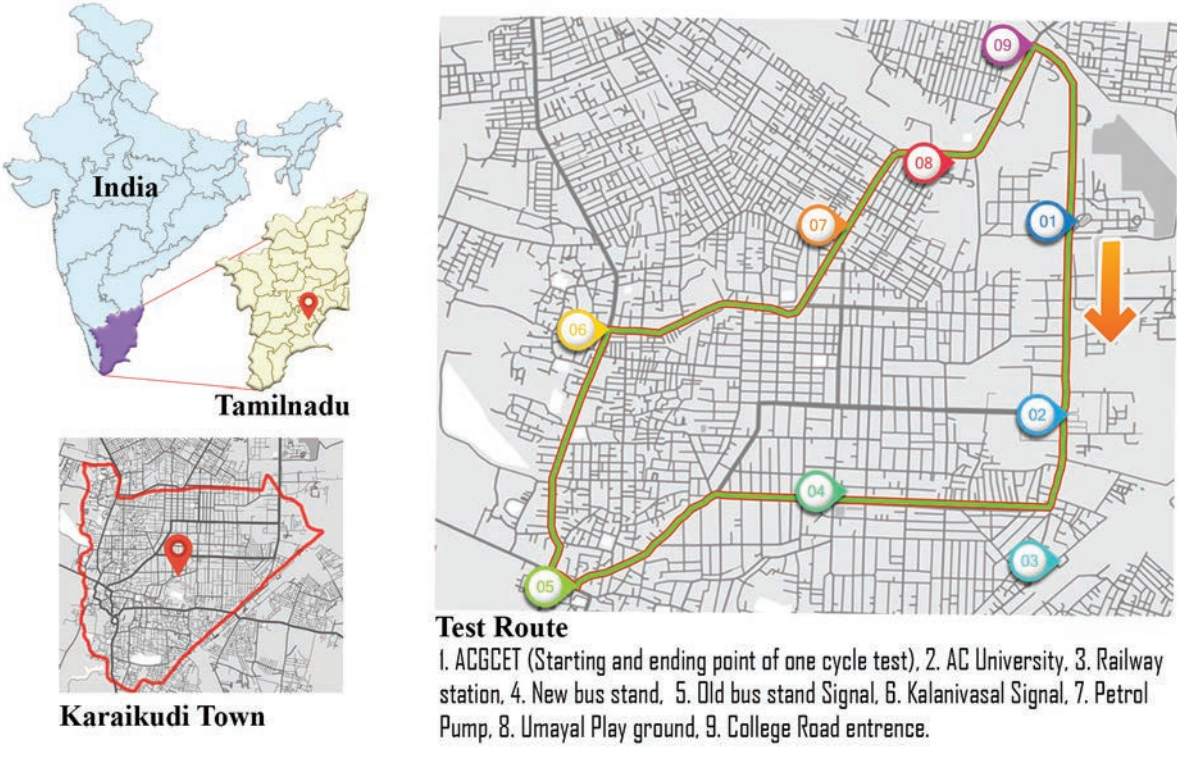

Fig. 2. *Location of Karaikudi town and experimental test route*

calibrated and field-tested before the measurement of CO_2. The measuring instrument is set to record data at a one-minute time interval; the data is then transferred to a laptop PC with an acquisition software provided by the device manufacturer to record the CO_2 values from the instrument. The schematic sketch is shown in Fig. 3 this set-up is used for carrying out our research. A five-seat hatchback car was chosen; it has air-conditioning with a variable temperature from 18 °C to 25° C and with recirculation modes.

Three tests are carried out for each human load varying from one to five, as the CO_2 concentration will significantly increase according to the number of passengers [30]. The mean values of three tests were considered for the final optimization of the parameters. The route at Karaikudi, where the test was carried out was about 13 km per cycle, which includes a college road with trees, traffic signals, a petrol station, road junctions, and a bus stand. The test route is shown in Fig. 2.

1.3.3 Design of Experiments and Regression Line

The design of experiments for the study was designed using full factorial design and regression modelling in statistical software. In each comprehensive trial run or repetition of the studies, the full factorial design establishes experimental points utilizing all feasible combinations of the levels of the components. The vertices of a hypercube in the n-dimensional design space are determined by the least and highest values of each of the factors. These factors are the experimental design points in a full factorial design; therefore, these experimental points are also known as factorial points.

Regression analysis is a type of predictive modelling approach that focuses on the correlation between a dependent (target) and an independent variable (predictor). This technique is used for the prediction of the finding of the fundamental effect relationship between the variables. The quartic non-linear regression model was suggested due to the better value of correlation coefficient and fitting to the data points. The refined model is also developed for predicting carbon dioxide levels for various human loads, which are further used for finding the better value of air quality parameters.

1.4 Search Optimization Methods

Among the various algorithms, the statistical, gradient, and metaheuristic algorithms are popularly used by most researchers for finding the optimum value of responses. The familiar algorithms in the above three categories are effectively chosen for finding indoor air quality characteristics in the present investigation. Response surface methodology (RSM) is based on indirect optimization self-organization; GRG is the most commonly used reduced gradient method to solve nonlinear problems, which finds a local optimal solution; genetic algorithm (GA solves optimization problems based on a natural selection process derived form biological evaluation; it uses high-level search procedures for minimization of response variables.

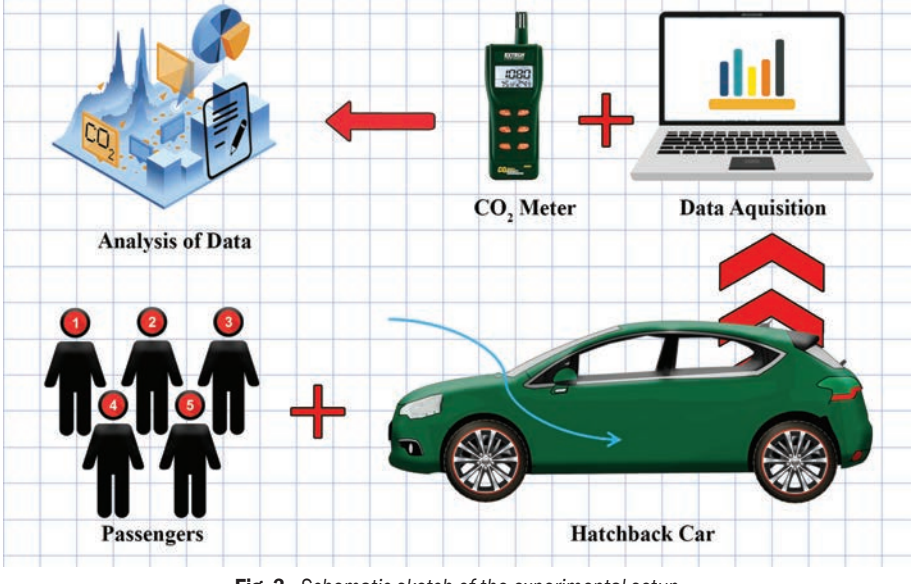

Fig. 3. *Schematic sketch of the experimental setup*

1.4.1 Response Surface Method

The RSM is a commonly used arithmetical and mathematical approach for developing and evaluating a process in which many factors impact the response of interest. This strategy aims to optimize the response time. The development of an approximation model for the true response surface is required for the RSM to be used in reality [31]. The RSM searches for a suitable approximation relationship between input and output variables to find the best operating conditions for a system or a portion of the factor field that complies with the requirements. The RSM was used to optimize the conditions of the experiment by the author Yan et al. [32] for the optimization and analysis of CO_2 surface assimilation by imidazole and tetraethylenepentamine operative sorbent material.

The RSM includes three stages (i.e., design, analysis, and optimization) using statistical software; a non-linear regression equation was developed and optimized using this approach for varying human loads in the present investigation. The ANOVA Table and statistical plots were also generated to study the individual, interaction, and higher-order effects of air quality parameters.

1.4.2 Generalized Reduced Gradient

The generalized reduced gradient (GRG) method is a nonlinear inequality constraint-aware expansion of the reduced gradient method. In this method, a quest path is found in which the current dynamic limitations remain precisely effective for any move. Microsoft Excel uses three solving methods such as GRG Nonlinear for problems that are smoothing nonlinear, LP Simplex for problems that are linear, and Evolutionary for non-smooth problems. GRG is used to find the optimum CO_2 level for various human loads by setting quadratic estimates, forward derivatives, and Newton search in the solver option. The max time was set to 100 seconds for 100 iterations with the precision value of 0.000001, the tolerance was set to 5 % and the convergence was 0.0001 in the Microsoft Excel Solver.

1.4.3 Genetic Algorithm

A genetic algorithm is a search heuristic based on Charles Darwin's natural-evolution hypothesis. This algorithm mimics natural selection, in which the fittest individuals are chosen for reproduction to create the next generation. GA have been used to solve a wide variety of systematic, engineering, and financial problems. GA are robust because they can find the global optimum in a multimodal landscape [33]. The initial population, fitness function, selection, crossover, and mutation are the five phases considered in a genetic algorithm.

MATLAB's R2016a graphical user interface was used to find the minimum value of the function. The double vector population type opted with the population type was left to default at 50 for five or fewer variables; otherwise, it was 200. The creation function was constrained dependent on keeping the initial population, initial scores, and initial range as default. For the fitness-scaling function, rank was chosen. The stochastic uniform was set for the selection function. In the reproduction section, elite count and cross-over fraction were default. Mutation and crossover functions are constraint-dependent. Migration direction is forward keeping fraction and interval values as default 0.2 and 20, respectively. For the constraint parameters, the nonlinear constraint algorithm Augmented Lagrangian is used with an initial penalty and penalty factor as default. The hybrid function was set to none, and the stopping criteria were completely used with default settings.

2 RESULTS AND DISCUSSION

2.1 Experimental Observation of Air Quality Characteristics

The three factors that are varied in three levels ($5 \times 8 \times 8 = 320$) contributed 320 experimental runs as per full factorial design. The standard deviation for human load, air speed, and temperature are 1.42, 2.29 and 2.29, respectively. A minimum value of 400 and a maximum value of 900 were observed in carbon dioxide level. The mean and standard deviations for the recorded value of responses are 583 and 128.9 respectively (Eq. (1)).

$$\bar{x} = \frac{\sum x}{n}, \quad \sigma = \sqrt{\frac{\sum \left(x - \bar{x}\right)^2}{n}}, \tag{1}$$

where $\bar{x}$ is mean, n number of observations, x individual observations, and σ standard deviation. The observation of the highest frequency for 230 data in 8 bins was obtained, which is shown in Fig. 4. The frequency is calculated using number of counts in the histogram range specified in x axis whereas proportion is calculated using the Eq. (2).

$$\text{Proportion} = \frac{\text{Frequency}}{n}. \tag{2}$$

The proportion and density plots are also obtained in correlation with recorded values of carbon dioxide levels. The CO_2 level is ranged from 460 ppm to 949 ppm and the corresponding frequency values up to 60 and proportion up to 0.2 are plotted.

2.2 Development of NLRM for Carbon Dioxide Level

The design is built, and response data is added to formulate a polynomial model of response design by including individual, interaction, and lower and higher-order terms. The polynomial degree of four, which is in the form of a quartic function was observed based on the best fit and the coefficient of correlation of 0.99. The statistical summary of factors and response are in Table 1

$$f(x) = ax^4 + bx^3 + cx^2 + dx + e. \quad (3)$$

The adjusted R^2 associates the explanatory power of regression replicas with varying numbers of predictors, whereas the projected R^2 shows how well a regression model predicts fresh observations' responses. The predicted R^2 of 0.98 is in satisfactory agreement with the adjusted of 0.99 due to the variance of less than 0.2. The subgroup sample standard deviation divided by the subsection mean, multiplied by 100, yields the percentage of the CV plot point. In practice, the percentage of CV is the proportion of the mean that the standard deviation.

The model *F*-value of 83 shows the model is considerable. There is only a 0.01 per cent probability that an *F*-value of this massive might appear due to noise. Model terms with *P*-values less than 0.0500 are noteworthy. x_1, x_3, $x_1 x_2$, $x_1 x_3$, x_1^2, x_3^2, $x_1 x_2 x_3$, $x_1^2 x_2$, $x_1^2 x_3$, x_1^3, $x_1^2 x_2^2$, $x_1^2 x_3^2$, $x_1^3 x_2$, $x_1^3 x_3$, $x_1 x_2^3$, $x_1 x_3^3$, x_1^4, x_3^4 are significant model terms in this scenario. The model terms are not significant if the value is larger than 0.1000. The model decrease may enhance your model if there are several irrelevant model terms (not involving those necessary to support hierarchy). The nonlinear regression model was developed using statistical software, as given in Eq. (4) .

$$\begin{aligned} f(x) = {} & +10021.14279 + 1030.93478 \times x_1 \\ & -2.\times x_2 - \times x_3 \\ & -2.\times x_1 \times x_2 - \times x_1 \times x_3 \\ & +3.\times x_2 \times x_3 + \times x_1^2 \\ & +0.\times x_2^2 + \times x_3^2 \\ & \times x_1 \times x_2 \times x_3 + \times x_1^2 \times x_2 \\ & +0.\times x_1^2 \times x_3 + \times x_1 \times x_2^2 \\ & +0.\times x_1 \times x_3^2 - \times x_2^2 \times x_3 \end{aligned}$$

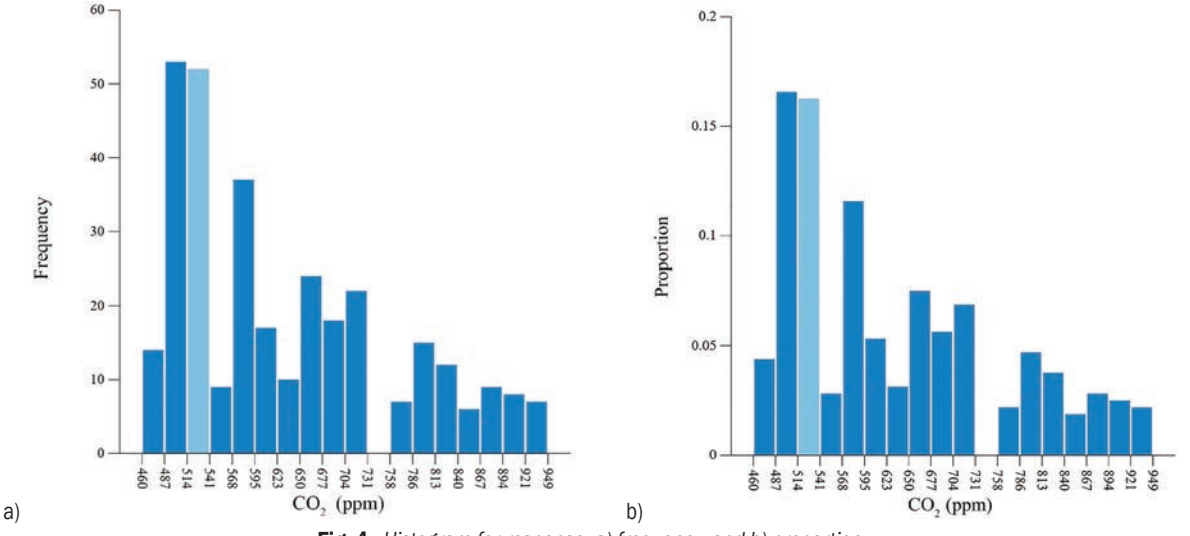

a) b)

Fig. 4. *Histogram for response; a) frequency, and b) proportion*

Table 1. *Statistical summary of factors and response*

Factor/ Response	Name	Minimum	Maximum	Coded Low	Coded High	Mean	Std. Dev.
Factor 1	Human load [No.]	1	5	-1 ↔ 1.00	+1 ↔ 5.00	3.00	1
Factor 2	Air speed [m/s]	1	8	-1 ↔ 1.00	+1 ↔ 8.00	4.50	2
Factor 3	Temperature [°C]	18	25	-1 ↔ 18.00	+1 ↔ 25.00	21.50	2
Response	CO_2 [ppm]	460	949	-	-	632.88	128.87

$$\begin{aligned} &-4.24 \times x_2 \times x_3^2 - 3.5 \times x_1^3 \\ &-1.24080 \times x_2^3 - 4.31326 \times x_3^3 - 0.192815 \times x_1^2 \times x_2^2 \\ &+ 0.0126 \times x_1^2 \times x_2 \times x_3 - 0.73 \times x_1^2 \times x_3^2 \\ &-0.0300 \times x_1 \times x_2^2 \times x_3 + 0.02888 \times x_1 \times x_2 \times x_3^2 \\ &+ 0.00532 \times x_2^2 \times x_3^2 - 0.041 \times x_1^3 \times x_2 \\ &+ 0.035 \times x_1^3 \times x_3 + 0.0092 \times x_1 \times x_2^3 \\ &-0.9 \times x_1 \times x_3^3 + 0.009 \times x_2^3 \times x_3 \\ &+ 0.020725 \times x_2 \times x_3^3 + 4.006 \times x_1^4 \\ &+ 0.08 \times x_2^4 + 0.0831 \times x_3^4 \ . \end{aligned} \quad (4)$$

The sequential *p*-value is less than 0.0001 and the difference between the adjusted and predicted coefficient of correlation is 0.0004 which indicated the best fit of the quartic model for 30 values of carbon dioxide level (Table 2). The sequential *p*-value is < 0.0001 for linear, two-factor interaction, quadratic, cubic, quartic, and quintic models. The best fit is selected based on the higher value of coefficient of correlation.

Table 2. *Fit summary and selection of model*

Source	Sequential *p*-value	Adjusted R^2	Predicted R^2	Remarks
Linear	< 0.0001	0.891	0.8889	-
2FI	< 0.0001	0.9197	0.917	-
Quadratic	< 0.0001	0.9935	0.9933	-
Cubic	< 0.0001	0.9942	0.9938	-
Quartic	< 0.0001	0.9972	0.9968	Suggested
Fifth	< 0.0001	0.9985	0.9981	Aliased

2.3 ANOVA, Diagnostics and Statistical Plots

The model includes the overall model test for significance and how much variance in the reaction is described by the model. Individual factors are removed from the model and tested separately. The residual indicates how much variation in the response remains unaccounted for. The degree to which the model predictions differ from the observed is referred to as "lack of fit". The amount of variation between replicate runs is known as "pure error". The degree of variation around the mean of the observations is shown by the corrected total. The individual effect of human load and temperature, combined effect of air speed and temperature, are significant terms in ANOVA listed in Table 3 The second-order effect of human load with air speed and temperature is also significant.

The normal probability plot shows whether the residuals have a normal distribution and, as a result, follow a straight line. For better analysis, scatter with normal data in an s-shaped curve showed the transformation response as shown in Fig. 5 . A graph of anticipated response values versus actual response values can be used to spot a value, or a collection of values, that the model cannot predict is shown in Fig. 5. The assumption of constant variance is tested by plotting the residuals against the ascending expected response values as shown in Fig. 5 . A studentized residual is calculated by dividing the residual by an estimate of its standard deviation. The standard deviation for each residual is computed with the observation excluded. A plot of the residuals against the experimental run order to look for hidden variables that could have influenced the response during the experiment is shown in Fig. 5. Internally studentized residuals are defined for each observation as an ordinary residual divided by an estimate of its standard deviation.

Cook's distance is a measurement of how much the entire regression function changes when the i^{th} point is removed from the model fitting (Fig. 6). The plot of the residuals versus any factor if the variation not accounted for by the model varies depending on the level of the factor is in Fig. 6. The response surface plot and contour plot for the interaction of variables are shown in Figs. 6 and d, respectively. Surface plots are diagrams of three-dimensional data that shows a functional relationship between a designated dependent variable and two independent variables. A contour plot is a graphical technique for representing a 3 dimensional surface by plotting constant z slices called "contours".

2.4 Optimization of Carbon Dioxide Level

2.4.1 RSM Optimization for Minimum Value of Carbon Dioxide Level

The human load is set to 1, 2, 3, 4 and 5 whereas the air speed and temperature are set in range as criteria and the minimization of carbon dioxide was carried out using response surface methodology. The minimum value of carbon dioxide levels for various human loads in accordance with air speed and temperature are given in Table 4 The optimization looks for a set of factor values that satisfies all the criteria for each of the responses and factors at the same time. The desirability function indicates the desirable limits for each response. The maximum value of air speed and low value of temperature is needed for getting the minimum value of CO_2 level in a 5 seat car. The minimum value of air speed and upper limit of temperature provided a minimum value of carbon dioxide of 7. The setting of air speed and

Table 3. *ANOVA for response and significance of factors*

Source	Sum of Squares	df	Mean Square	*F*-value	*p*-value	Remarks
Model	5.29E+06	34	1.55E+05	3389.3	< 0.0001	Significant
x_1	3.76E+05	1	3.76E+05	8202.13	< 0.0001	
x_2	145.96	1	145.96	3.18	0.0755	
x_3	6182.8	1	6182.8	134.82	< 0.0001	
$x_1 \times x_2$	851.29	1	851.29	18.56	< 0.0001	
$x_1 \times x_3$	5184.82	1	5184.82	113.06	< 0.0001	
$x_2 \times x_3$	31.56	1	31.56	0.6882	0.4075	
x_1^2	461.81	1	461.81	10.07	0.0017	
x_2^2	33.99	1	33.99	0.7412	0.39	
x_3^2	532.36	1	532.36	11.61	0.0008	
$x_1 \times x_2 \times x_3$	296.12	1	296.12	6.46	0.0116	
$x_2^2 \times x_3$	2296.85	1	2296.85	50.08	< 0.0001	
$x_1^2 \times x_3$	1101.23	1	1101.23	24.01	< 0.0001	
$x_1 \times x_2^2$	15.47	1	15.47	0.3374	0.5618	
$x_1 \times x_3^2$	0.7741	1	0.7741	0.0169	0.8967	
$x_2^2 \times x_3$	3.98	1	3.98	0.0867	0.7686	
$x_2 \times x_3^2$	54.02	1	54.02	1.18	0.2787	
x_1^3	594.83	1	594.83	12.97	0.0004	
x_2^3	0.4001	1	0.4001	0.0087	0.9256	
x_3^3	162.26	1	162.26	3.54	0.061	
$x_1^2 \times x_2^2$	699.53	1	699.53	15.25	0.0001	
$x_1^2 \times x_2 \times x_3$	4.08	1	4.08	0.089	0.7657	
$x_1^2 \times x_3^2$	559.98	1	559.98	12.21	0.0006	
$x_1 \times x_2^2 \times x_3$	67.35	1	67.35	1.47	0.2266	
$x_1 \times x_2 \times x_3^2$	57.83	1	57.83	1.26	0.2624	
$x_1^2 \times x_3^2$	4	1	4	0.0871	0.768	
$x_1^3 \times x_2$	971.26	1	971.26	21.18	< 0.0001	
$x_1^3 \times x_3$	3125.25	1	3125.25	68.15	< 0.0001	
$x_1 \times x_2^3$	393.27	1	393.27	8.58	0.0037	
$x_1 \times x_3^3$	973.35	1	973.35	21.22	< 0.0001	
$x_2^3 \times x_3$	2.37	1	2.37	0.0517	0.8203	
$x_2 \times x_3^3$	53.58	1	53.58	1.17	0.2807	
x_1^4	8445.27	1	8445.27	184.15	< 0.0001	
x_2^4	172.39	1	172.39	3.76	0.0535	
x_3^4	204.18	1	204.18	4.45	0.0357	
Residual	13070.01	285	45.86			

temperature for an intermediate value of human loads are effectively determined using response surface optimization. The maximum value of air speed and lower limit of temperature provided a minimum value of carbon dioxide of 9[illegible] ppm for the maximum capacity of the vehicle.

2.4.2 GRG Optimization for Minimum Value of Carbon Dioxide Level

The minimum CO_2 concentration value of 4[illegible]5 ppm was achieved in accordance with air speed and temperature of 2 m/s and 24 °C, respectively, for a single human load using the GRG technique. In a comparison of the three optimization methods utilized for one human load, among RSM (4[illegible]5 , GRG (4[illegible]5 , and GA (4[illegible]1), the lowest CO_2 level

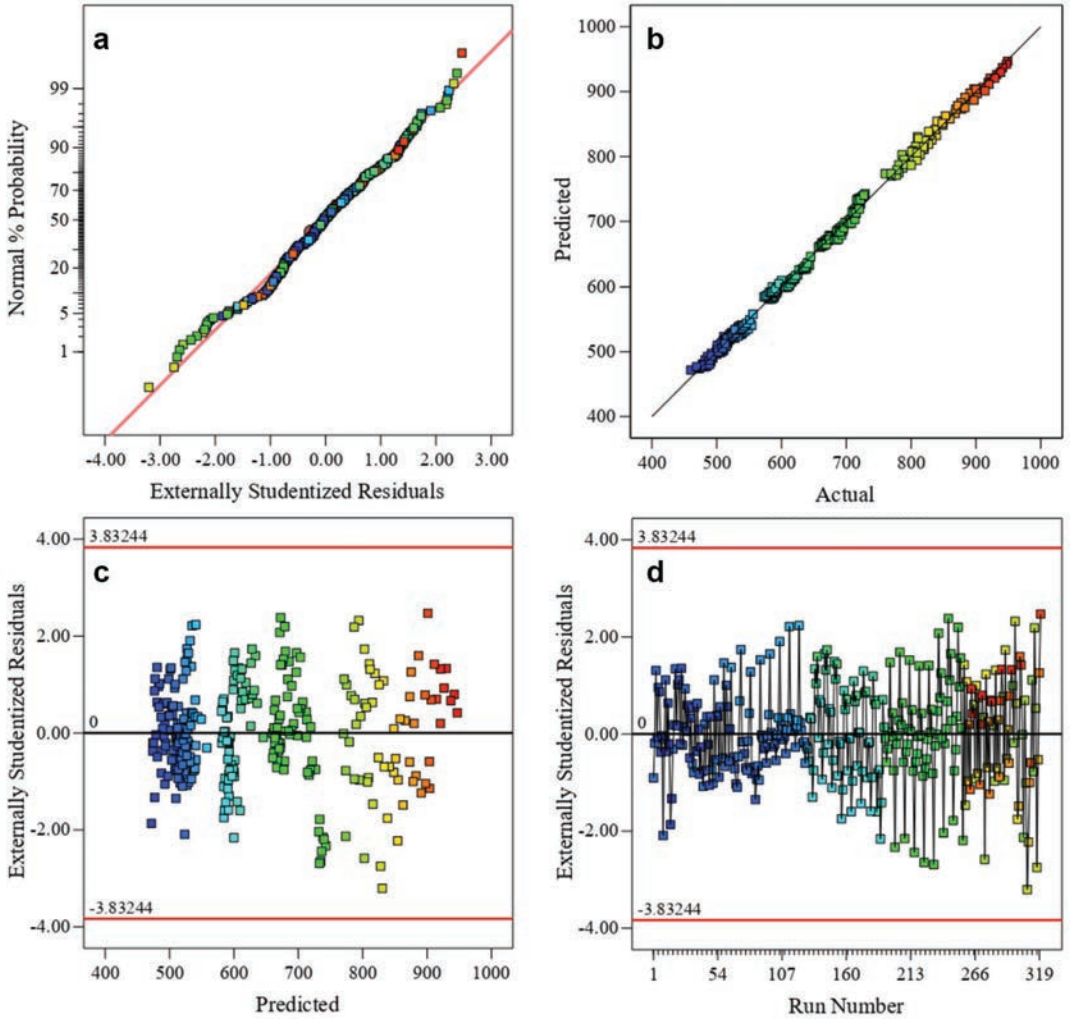

Fig. 5. *Plot of residuals; a) normal % probability, b) predicted vs. actual, c) residuals vs. predicted, and d) residuals vs. run*

was attained in GRG methods. The carbon dioxide levels of 688.37 ppm, 610.22 ppm, 619 ppm and 606 ppm were obtained for human loads 2, 3, 4 and 5, respectively.

When compared with RSM, GRG provided a minimum value of carbon dioxide level for all levels of human load. The search procedure in GRG found a better value of results when compared with statistical-based optimization. RSM is a mathematical and statistical technique for the empirical model building which predicted better value of responses using indirect optimization based on self-organization whereas the Newton method used a root-finding approach by polynomial approximation using Taylor's series. The air speed of 7 m/s and temperature of 18 °C were obtained for a minimum value of carbon dioxide level of 606 ppm in GRG and GA methods.

2.4.3 GA Optimization for Minimum Value of Carbon Dioxide Level

The minimum CO_2 concentration of 451 ppm for one human load was obtained for the air speed of 2 m/s and a temperature of 24 °C using the GA method, which was slightly higher than the optimum value (437 ppm) obtained using the GRG method. The lowest ideal value for a five-person capacity is 606 at an air speed of 7 m/s and a temperature of 18 °C, respectively. The carbon dioxide levels of 688.37 ppm, 610.22 ppm, 619 ppm and 606 ppm were obtained for human loads 2, 3, 4 and 5 respectively which is the same as the results obtained using the GRG method. When comparing the results acquired using the GA method in MATLAB software to the obtained results using RSM optimization in Design-Expert software, the GA approach produced

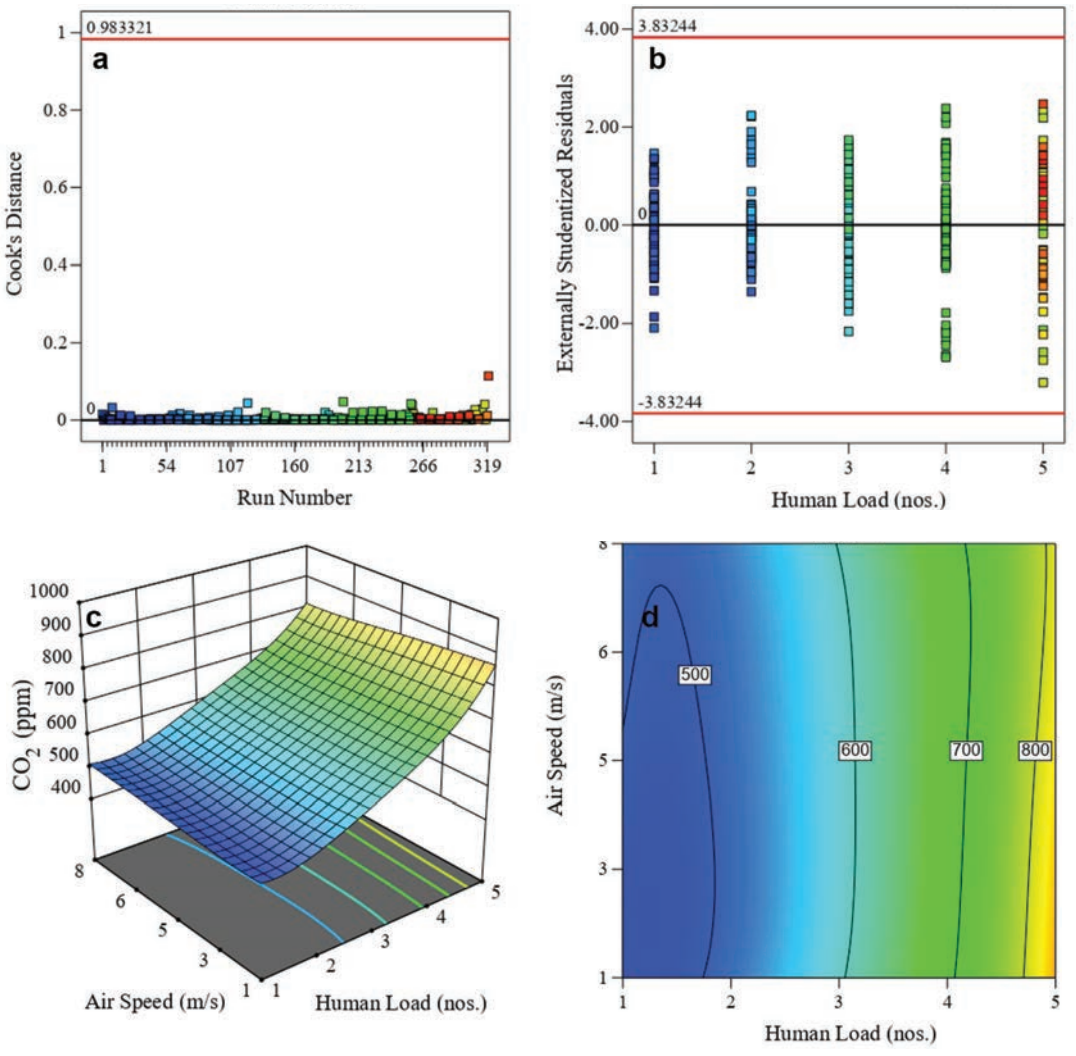

Fig. 6. *Design plots; a) Cook's distance, b) residual vs. factor, c) 3D surface plot, and d) contour plot*

Table 4. *Optimum values of CO_2 level for various human loads and confirmation of responses*

Sl. No.	Algorithm	Factors		CO_2 [ppm]		Absolute percentage of error
		Airspeed [m/s]	Air temp. [°C]	Predicted response	Experimental response	
1	RSM	2	24	471.876	479.983	1.7
2		3	21	508.865	503.832	0.2
3		3	20	580.79	586.231	0.9
4		6	19	659.905	671.376	1.7
5		8	18	769.362	752.263	2.2
6	GRG	2	24	471.537	479.983	1.8
7		3	21	508.785	503.832	0.9
8		3	19	580.722	586.231	0.9
9		6	19	659.839	671.376	1.7
10		7	18	769.016	777.847	1.1
11	GA	2	24	471.611	479.983	1.3
12		3	21	508.785	503.832	0.9
13		3	20	580.722	589.124	0.9
14		6	19	659.839	671.376	1.7
15		7	18	769.016	777.847	1.1

lower results due to the metaheuristic approach (High-level search procedure). In addition, when compared to RSM, the air velocity for the five human load conditions is lowered by one level in the GA optimization technique. The GA plots for optimization plotting fitness value vs. generation are shown in Fig. 7. The values are obtained in between 0 to 100 generations for the better value of fitness. The same value of best fitness and mean fitness was obtained which indicated the minimum value of carbon dioxide level for various human loads.

2.4.4 Confirmation of Optimum Conditions

The experiments were conducted for the optimum conditions obtained using RSM, GRG, and GA methods; the carbon dioxide levels values were reordered and compared with the optimum values. The comparison graph of experimental results and predicted results are shown in Fig. 8. The blue, green, and yellow lines indicated the optimum value of carbon dioxide levels for RSM, GRG, and GA, respectively, whereas the orange, red, and violet lines indicated the experimental value of carbon dioxide levels for RSM, GRG, and GA, respectively. RSM predicted carbon dioxide levels of 476 ppm, 508 ppm, 580.7 ppm, 660 ppm, and 769.8 ppm for human loads 1, 2, 3, 4 and 5 and the same is confirmed with experimental values of 479 ppm, 503 ppm, 582 ppm, 656 ppm, and 773.2 ppm. The absolute percentage error of values 1.3, 0.9, 0.9, 1.7, and 1.1 for human loads 1, 2, 3, 4 and 5 were obtained using the GRG method. GA predicted carbon dioxide levels of 476.1 ppm,

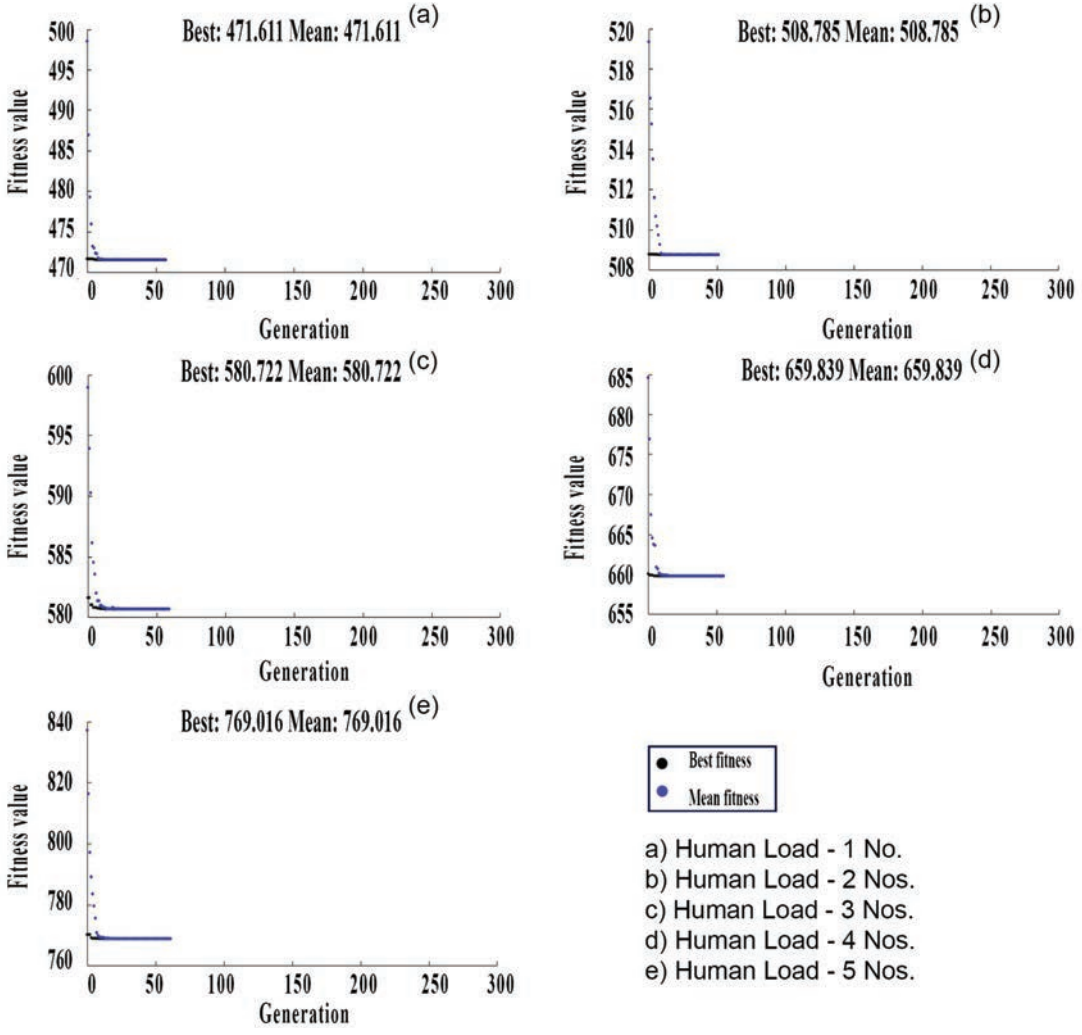

Fig. 7. *GA plot for optimization of carbon dioxide level for different human load*

0.87 ppm, 0.22 ppm, 0.9 ppm, and 0.06 ppm for human loads 1, 2, 3, 4 and 5 and the same is confirmed with experimental values of 0.9 ppm, 0.3 ppm, 0.4 ppm, 0.6 ppm, 0.4 ppm, respectively.

The absolute ratio of error is determined using the following formulation.

$$\text{Percentage of error} = \frac{(\text{Experimental value} - \text{Optimum value})}{\text{Experimental value}}. \quad (5)$$

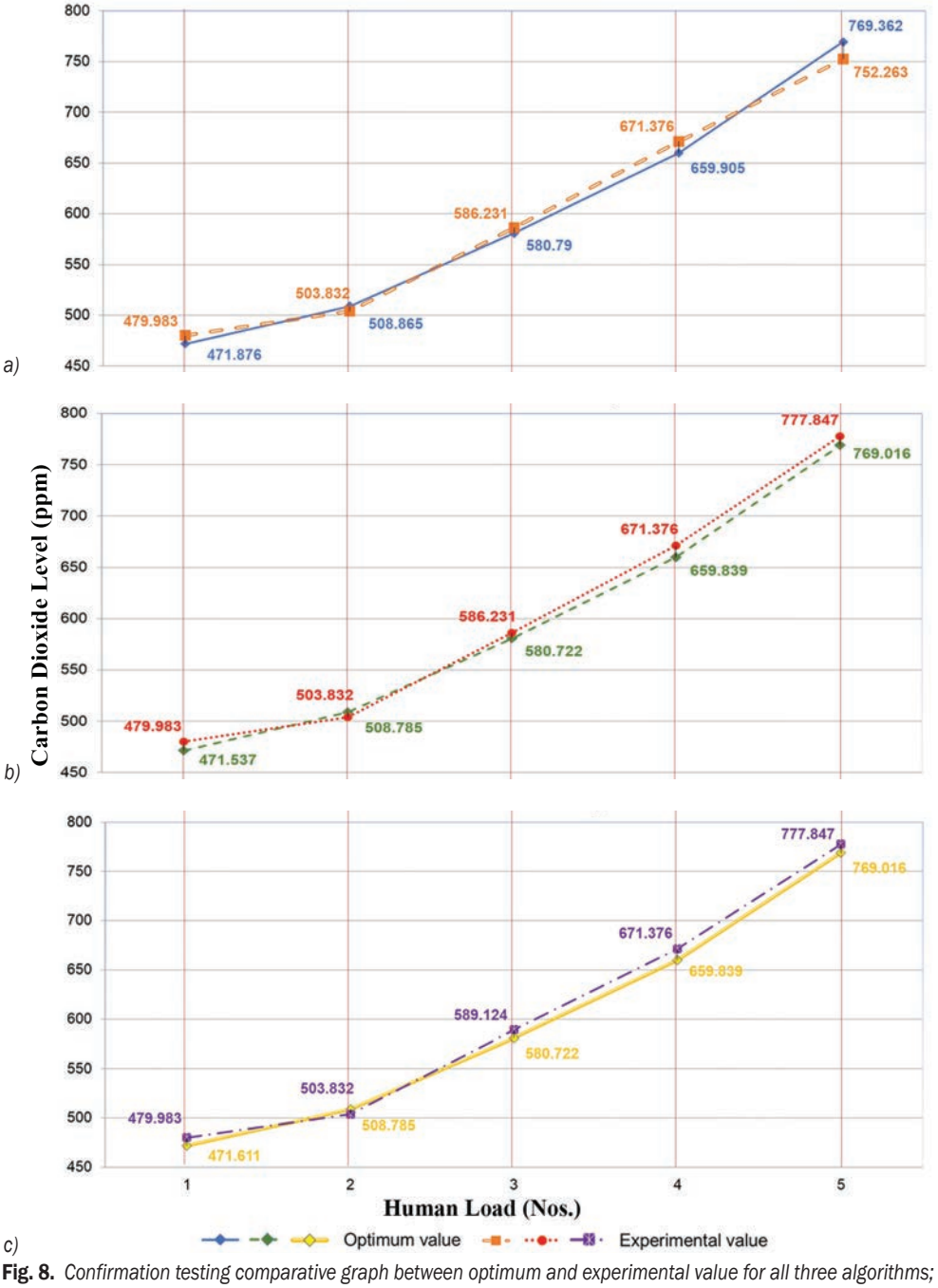

Fig. 8. *Confirmation testing comparative graph between optimum and experimental value for all three algorithms; a) RMS, b) GRG, and c) GA*

The absolute percentage of error is less than 2.5 indicating good level of accuracy in the confirmation of results the maximum absolute percentage of error of 2.2 in RSM, 1.8 in GRG and 1.7 in GA were obtained. The close prediction of experimental value with the predicted value was obtained.

3 CONCLUSION

Experimental runs were carried out for different values of human load, air speed, and temperature, and the observed value of carbon dioxide levels were recorded. Response surface design, analysis, and optimization were done to find the minimum value of carbon dioxide levels for various human loads and corresponding air velocity and temperature. In addition, with response surface methodology, the generalized reduced gradient and genetic algorithm are also used to find the minimum value of carbon dioxide levels in the present investigation. The minimum carbon dioxide level of 414.3 ppm for one human load was obtained for the air speed of 2 m/s and a temperature of 24 °C using the GRG method. The carbon dioxide levels of 608.8 ppm, 803.22 ppm, 999 ppm and 1190.6 ppm were obtained for human loads 2, 3, 4 and 5, respectively, using GRG and GA methods. The experiment was conducted for the optimum value of IVAQ parameters, and the corresponding CO_2 level was measured. The absolute percentage of error was found for all three algorithms, which resulted in the genetic algorithm providing a better value of results for the current problem. Other indoor air quality characteristics, such as relative humidity, particulate matter, carbon monoxide level, and oxygen level may be optimised using the optimization techniques, and the optimal value for comfort and healthy living in an enclosed environment can be found. These methods can be used to determine the optimal inlet HVAC parameters such as inlet velocity, the quantity of fresh air supply, type of filtration, and required temperature for various human loads in a confined area. This application could lead to a better and healthier indoor living environment. Even though this method has a wide range of applications, the IAQ characteristics vary from place to place, and values in different countries may deviate at a significant pace depending on the environmental circumstances and abrupt climate changes of that country as well as the region under study. In the future, the same study can be extended to other vehicle cabins, such as those of SUVs or seven-seat cars, trucks, buses and even trains by varying different passenger loads, elevation of location under study, ventilation type, and outside environmental weather conditions. It is also concluded that breathing clean air is a vital aspect of investigation for enhanced human health during the Covid-19 pandemic.

4 REFERENCES

[1] Gladyszewska-Fiedoruk, K. (2011). Concentrations of carbon dioxide in a car. *Transportation Research Part D: Transport and Environment*, vol. 16, no. 4, p. 166-171, **DOI:10.1016/j.trd.2011.01.005**.

[2] Kaur, S., Nieuwenhuijsen, M.J., Colvile, R.N. (2007). Fine particulate matter and carbon monoxide exposure concentrations in urban street transport microenvironments. *Atmospheric Environment*, vol. 41, no. 23, p. 4781-4810, **DOI:10.1016/j.atmosenv.2007.02.002**.

[3] El-Fadel, M., Abi-Esber, L., (2009). In-vehicle Exposure to Carbon Monoxide Emissions from Vehicular Exhaust: A Critical Review. *Critical Reviews in Environmental Science and Technology,* vol. 39, no. 8, p.585-621, **DOI:10.1080/10643380701798264**.

[4] Knibbs, L.D., Cole-Hunter, T., Morawska, L. (2011). A review of commuter exposure to ultrafine particles and its health effects. *Atmospheric Environment*,vol. 45, no. 16, p. 2611-2622, **DOI:10.1016/j.atmosenv.2011.02.065**.

[5] Dovjak, M., Slobodnik, J., Krainer, A. (2019). Deteriorated indoor environmental quality as a collateral damage of present day extensive renovations. *Strojniški vestnik - Journal of Mechanical Engineering*, vol. 65, no. 1, p. 31-40, **DOI:10.5545/sv-jme.2018.5384**.

[6] Yin, H., Zhai, X., Ning, Y., Li, Z., Ma, Z., Wang, X., Li, A. (2022). Online monitoring of $PM_{2.5}$ and CO_2 in residential buildings under different ventilation modes in Xi'an city. *Building and Environment*, vol. 207, art. ID 108453, **DOI:10.1016/j.buildenv.2021.108453**.

[7] Dab, W., Ségala, C., Dor, F., Festy, B., Lameloise, P., Le Moullec, Y., Quénel, P., Wallaert, B., Zmirou, D. (2001). Air pollution and health: Correlationor causality? The case of the relationship between particle exposure and cardiopulmonary mortality. *Journal of the Air & Waste Management Association*, vol. 51, no. 2, p. 203-235, **DOI:10.1080/10473289.2001.10464267**.

[8] Persily, A., Dols, W.S. (1990). The relation of CO_2 concentration to office building ventilation. *Air Change Rate and Air tightness in Buildings*. Sherman, M.H. (ed.), ASTM International, West Conshohocken, p. 77-92, **DOI:10.1520/STP17206S**.

[9] Kim, H.H., Park, G.Y., Lee, J.H. (2019). Concentrations of particulate matter, carbon dioxide, VOCs and risk assessment inside Korean taxis and ships. *Environmental Science and Pollution Research*, vol. 26, no. 10, p. 9619-9631, **DOI:10.1007/s11356-019-04361-5**.

[10] Muhič, S., Muhič, T. (2022). Measurements of air quality in kindergartens and schools in the republic of Slovenia before the COVID-19 epidemic. *Strojniški vestnik-Journal of Mechanical Engineering*, vol. 68, no. 4, p. 290-299, **DOI:10.5545/sv-jme.2022.13**.

[11] Grady, M.L., Jung, H., Kim, Y.C., Park, J.K., Lee, B.C. (2013). Vehicle cabin air quality with fractional air recirculation. *SAE Technical Paper*, no. 01-1494, **DOI:10.4271/2013-01-1494**.

[12] Kadiyala, A., Kumar, A. (2013). Quantification of in-vehicle gaseous contaminants of carbon dioxide and carbon monoxide under varying climatic conditions. *Air Quality, Atmosphere & Health*, vol. 6, no. 1, p. 215-224, **DOI:10.1007/s11869-011-0163-2**.

[13] Ren, J., He, J., Kong, X., Xu, W., Kang, Y., Yu, Z., Li, H., (2022). A field study of CO_2 and particulate matter characteristics during the transition season in the subway system in Tianjin, China. *Energy and Buildings*, vol. 254, art. ID 111620, **DOI:10.1016/j.enbuild.2021.111620**.

[14] Mathur, G.D. (2018). Effect of cabin volume on build-up of cabin carbon dioxide concentrations from occupant breathing in automobiles. *SAE Technical Paper*, no. 2018-01-0074, **DOI:10.4271/2018-01-0074**.

[15] Kumar, S., Jain, M.K., (2022). Exposure to particulate matter and CO_2 in indoor conditions at IIT (ISM) Dhanbad. *Materials Today: Proceedings*, vol. 49, p. 3469-3473, **DOI:10.1016/j.matpr.2021.04.496**.

[16] Kundu, P., Goel, K., Zinta, G. (2022). Nutritional imbalance in plants under rising atmospheric CO_2. *Plant Nutrition and Food Security in the Era of Climate Change*, p. 513-536, **DOI:10.1016/B978-0-12-822916-3.00006-8**.

[17] Chang, T.B., Sheu, JJ., Huang, J.W., Lin, Y.S., Chang, C.C. (2018). Development of a CFD model for simulating vehicle cabin indoor air quality. *Transportation Research Part D: Transport and Environment*, vol. 62, p. 433-440, **DOI:10.1016/j.trd.2018.03.018**.

[18] Satish, U., Mendell, M.J., Shekhar, K., Hotchi, T., Sullivan, D., Streufert, S., Fisk, W.J. (2012). Is CO_2 an indoor pollutant? Direct effects of low-to-moderate CO_2 concentrations on human decision-making performance. *Environmental Health Perspectives*, vol. 120, no. 12, p. 1671-1677, **DOI:10.1289/ehp.1104789**.

[19] Kusiak, A., Li, M. (2009). Optimal decision making in ventilation control. *Energy*, vol. 34, no. 11, p. 1835-1845, **DOI:10.1016/j.energy.2009.07.039**.

[20] Trends in Atmospheric Carbon Dioxide (2021). Global Monitoring Laboratory, Global average CO_2 level, NOAA, from *https://gml.noaa.gov/ccgg/trends/*, accessed on 2021-11-10.

[21] ANSI, Standard 62-1999. *Ventilation for Acceptable Indoor Air Quality*. American Society of Heating Refrigerating and Air Conditioning Engineers, Inc., Atlanta.

[22] Abi-Esber, L., El-Fadel, M. (2013). Indoor to outdoor air quality associations with self-pollution implications inside passenger car cabins. *Atmospheric Environment*, vol. 81, p. 450-463, **DOI:10.1016/j.atmosenv.2013.09.040**.

[23] Alcalá, R., Benítez, J.M., Casillas, J., Cordón, O., Pérez, R. (2003). Fuzzy control of HVAC systems optimized by genetic algorithms. *Applied Intelligence*, vol. 18, no. 2, p. 155-177, **DOI:10.1023/A:1021986309149**.

[24] Congradac, V., Kulic, F. (2009). HVAC system optimization with CO_2 concentration control using genetic algorithms. *Energy and Buildings*, vol. 41, no. 5, p. 571-577, **DOI:10.1016/j.enbuild.2008.12.004**.

[25] Fanger, P.O. (2000). Good air quality in offices improves productivity. *Strojniški vestnik - Journal of Mechanical Engineering*, vol. 46, no. 7, p. 408-412.

[26] Zhang, D., Ding, E., Bluyssen, P.M. (2022). Guidance to assess ventilation performance of a classroom based on CO_2 monitoring. *Indoor and Built Environment*, vol. 31, no. 7, p. 1107-1126, **DOI:10.1177/1420326X211058743**.

[27] Kusiak, A., Tang, F., Xu, G. (2011). Multi-objective optimization of HVAC system with an evolutionary computation algorithm. *Energy*, vol. 36, no. 5, p. 2440-2449, **DOI:10.1016/j.energy.2011.01.030**.

[28] Thirumal, P., Amirthagadeswaran, K.S., Jayabal, S. (2014). Optimization of indoor air quality characteristics in an air-conditioned car using multi-objective genetic algorithm. *Arabian Journal for Science and Engineering*, vol. 39, no. 11, p. 8307-8317, **DOI:10.1007/s13369-014-1392-0**.

[29] Ayyakkannu, R.K., Subbaian, J., Pandian, M., Iruthayaraj, D.L. (2021). Commuter exposure to fine particulate matter in private road transport modes in Salem, India. Thermal Science, vol. 26, no. 2, p. 1695-1708, **DOI:10.2298/TSCI200629214A**.

[30] Goh, C.C., Kamarudin, L.M., Shukri, S., Abdullah, N.S., Zakaria, A. (2016). Monitoring of carbon dioxide (CO_2) accumulation in vehicle cabin. *3rd International Conference on Electronic Design*, p. 427-432, **DOI:10.1109/ICED.2016.7804682**.

[31] Węglowski, M.S. (2014). Experimental study and response surface methodology for investigation of FSP process. *Archive of Mechanical Engineering*, vol. 61, no. 4, p. 539-552, **DOI:10.2478/meceng-2014-0031**.

[32] Yan, H., Zhang, G., Liu, J., Li, G., Wang, Y. (2021). Highly efficient CO_2 adsorption by imidazole and tetraethylenepentamine functional sorbents: Optimization and analysis using response surface methodology. *Journal of Environmental Chemical Engineering*, vol. 9, no. 4, art. ID 105639, **DOI:10.1016/j.jece.2021.105639**.

[33] Huang, W., Lam, H.N. (1997). Using genetic algorithms to optimize controller parameters for HVAC systems. *Energy and Buildings*, vol. 26, no. 3, p. 277-282, **DOI:10.1016/S0378-7788(97)00008-X**.

Strojniški vestnik - Journal of Mechanical Engineering 68(2022)7-8, 485-492
DOI:10.5545/sv-jme.2022.174
Original Scientific Paper
Received for review: 2022-04-25
Received revised form: 2022-06-20
Accepted for publication: 2022-07-08

Optimization in the Resistant Spot-Welding Process of AZ61 Magnesium Alloy

Davood Afshari[1,*] – Ali Ghaffari[1] – Zuheir Barsum[2]
[1] University of Zanjan, Iran
[2] Royal Institute of Technology, Sweden

In this paper, an integrated artificial neural network (ANN) and multi-objective genetic algorithm (GA) are developed to optimize the resistance spot welding (RSW) of AZ61 magnesium alloy. Since the stability and strength of a welded joint are strongly dependent on the size of the nugget and the residual stresses created during the welding process, the main purpose of the optimization is to achieve the maximum size of the nugget and minimum tensile residual stress in the weld zone. It is identified that the electrical current, welding time, and electrode force are the main welding parameters affecting the weld quality. The experiments are carried out based on the full factorial design of experiments (DOE). In order to measure the residual stresses, an X-ray diffraction technique is used. Moreover, two separate ANNs are developed to predict the nugget size and the maximum tensile residual stress based on the welding parameters. The ANN is integrated with a multi-objective GA to find the optimum welding parameters. The findings show that the integrated optimization method presented in this study is effective and feasible for optimizing the RSW joints and process.

Keywords: resistance spot welding, residual stresses, artificial neural network, genetic algorithm, AZ61 magnesium alloy

Highlights

- *A full factorial design of experiments has been utilized to investigate the effects of the welding parameters on the nugget size and the residual stresses in the AZ61 resistance spot welded joint.*
- *The nugget size and the residual stresses have been measured experimentally based on the DOE.*
- *Two separate ANN models have been created to predict the nugget size and the maximum residual stress using the welding parameters.*
- *An integrated ANN-ANN-GE algorithm has been developed to optimize the welding process.*
- *The results show that the welding current and the welding time have significant effects on the nugget size and the maximum residual stress, respectively.*
- *The findings confirm that the presented algorithm is effective and feasible to optimize the RSW process.*

0 INTRODUCTION

In recent years, alloys of Magnesium (Mg) have become of great attraction and significance as easy-to-machine metals with exceptional strength-to-weight ratios, for various sectors including automotive, aerospace, and structural applications [1]. Magnesium is the lightest of all commonly used structural metals; with a density that is approximately two thirds that of aluminium and one quarter that of steels. Other than this, magnesium alloys have a high strength-to-density ratio, high specific heat, low melting temperature, and good castability, hot formability, recyclability, and sound-damping capabilities [1] to [5]. These properties bring a significant interest in many industrial applications to reduce the weight of the structures. Despite these considerable interests, using magnesium alloys in the industry remains limited compared with aluminium and steel alloys due to some technical problems. For example, the resistance spot welding (RSW) of magnesium alloys is more complex than in steel and aluminium alloys and needs different welding parameters.

Although many new welding processes have been developed and presented for magnesium alloys (such as friction stir welding [6] to [9], laser welding [10] and [11]), RSW remains the most common joining process. In RSW, a high electric current is passed through the sheets via electrodes for a short time, which results in the generation of a melting zone between the sheets. After switching off the electrical current and undergoing a cooling process, a nugget is created in the welding area. Studies have shown that the nugget size is the most important controlling factor to determine the mechanical strength of the joint. The larger nugget results in higher mechanical strength [12] to [14]. In addition, when the molten metal starts cooling down to room temperature, a large temperature gradient occurs in the heat-affected zone (HAZ). This non-uniform temperature change leads to residual stresses in the welded joint. The residual stresses significantly affect stress corrosion cracking, hydrogen-induced cracking, and fatigue strength. Regardless of the loading conditions on spot-welded joints, tensile residual stress deteriorates the fatigue strength and the quality of the joint [15] to [17].

*Corr. Author's Address: University of Zanjan, Zanjan, Iran, dafshari@znu.ac.ir

Therefore, selecting the optimum welding parameters to achieve the maximum nugget size and the minimum tensile residual stress is the key factor in obtaining high-quality welding and joint strength.

Yi et al. [18] introduced a non-linear multiple orthogonal regression assembling model to optimize the welding parameters of RSW on galvanized steel sheet. They evaluated the effects of the welding parameters on the nugget size and optimized the parameters to maximize it. Hamidinejad et al. [19] predicted the mechanical strength of the RSW in the galvanized steel joints based on the welding parameters. They also optimized the welding parameters with a genetic algorithm (GA) to improve the tensile-shear strength. A multi-objective Taguchi method was applied to optimize the welding parameters in RSW of low-carbon steel by Muhammad et al. [20]. The main purpose of the study was to select the optimum RSW parameters to increase the nugget size and decrease the heat-affected zone (HAZ). Zhao et al. [21] utilized the response surface methodology (RSM) to optimize the nugget size, the mechanical strength, and the failure load in small-scale RSW of titanium alloy.

A hybrid ANN-GA model was developed by Pashazadeh et al. [22] to optimize the welding parameters of RSW on AISI 1008 steel alloy and achieve the maximum nugget size. Mirzaei et al. [23] developed a finite element (FE) model to predict the nugget size in RSW on galvanized steel. They used the RSM to optimize the welding parameters and obtain the maximum nugget size and maximum mechanical strength. Valera et al. [24] applied the Taguchi design of experiments to optimize the RSW of TRIP steel. The optimized electrical parameters were presented to increase the tensile-shear strength of the welded joints. The dissimilar RSW of AISI 316L austenitic stainless steel and 2205 duplex stainless steel were optimized by Vignesh et al. [25] using Taguchi's L27 orthogonal array (OA) design. Their results revealed that the welding current is the most dictating factor in achieving the highest tensile strength with superior weld quality.

The literature indicates that the optimization in the RSW of magnesium alloys has not been studied extensively. The purpose of this study is to contribute to the optimization of the welding parameters: electrical current, welding time, and electrode force of AZ61 magnesium alloy RSW joints. A full factorial design of the experimental (DOE) results is carried out and then two separate ANN models are developed to predict the nugget size and the maximum residual stress. Finally, an integrated ANN-ANN-GA algorithm is developed to optimize the welding parameters.

1 METHODS

In this study, AZ61 magnesium alloy has been used to prepare the welded samples. The nugget size has been measured experimentally for all the samples and an X-ray method has been utilized to measure the residual stresses. To predict the nugget size and the residual stresses, two ANN models have been developed. Finally, the welding parameters have been optimized by an integrated ANN-ANN-GE to obtain the maximum nugget size and the minimum tensile residual stress.

2 EXPERIMENTAL

AZ61 magnesium alloy sheets have been used to prepare the welding samples and their chemical composition is given in Table 1

Table 1. *Chemical compositions of AZ61 Mg alloy [wt.%]*

Ca	Cu	Fe	Si	Mn	Zn	Al	Mg
0.001	0.001	0.003	0.04	0.19	0.72	6.3	92.7

Fig. 1 shows the specification of the specimens (100 mm × 25mm × 1.2 mm) and the welded joints.

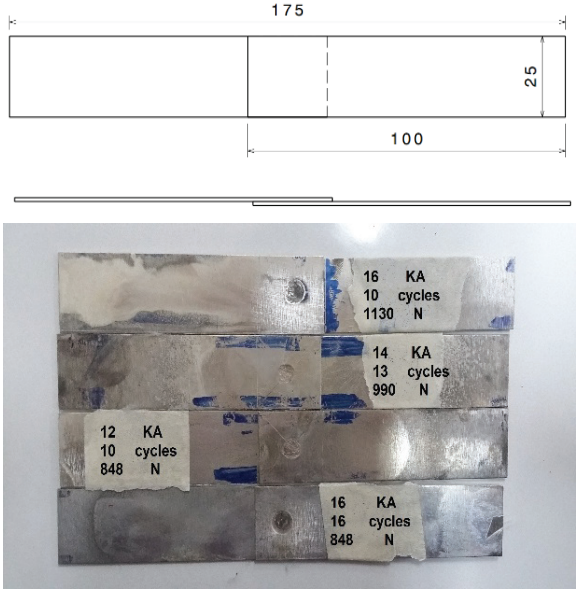

Fig. 1. *The dimensions of welded samples (dimensions in mm, not to scale) and the welded joints*

The surfaces of the specimens have been cleaned using a hard brush before welding. RSW has been

performed by using a Novin Sazan Company Machine (model SSA014 IRAN, Fig. 2) with a CU08 controller and nominal welding power of 120 kVA. Both copper electrodes were cooled by circulating water during the welding. The welded samples have been cut along the centreline and the nugget size has been measured using an optical microscope (Fig. 3). A SEIFERT X-ray diffractometer (model 3000P TS, Fig. 4) has been utilized for the residual stress measurements. Measurements have been performed in the centre of the welded zone where the maximum tensile residual stress occurs [17]. The residual stresses have been measured on both sides of the welded samples in radial and transverse directions. The average of measured residual stresses has been reported as the maximum tensile residual stress in the welded zone.

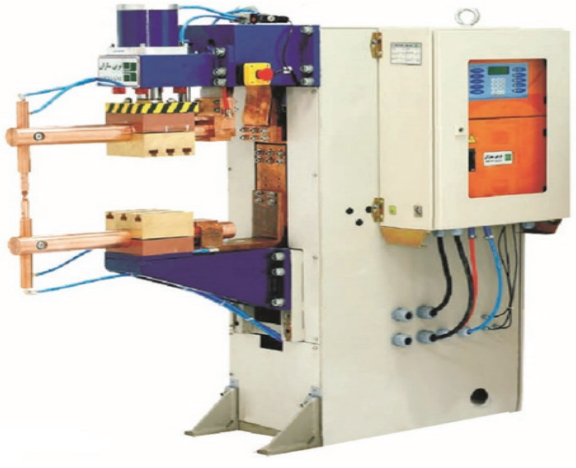

Fig. 2. *The RSW machine, Novin Sazan model SSA014*

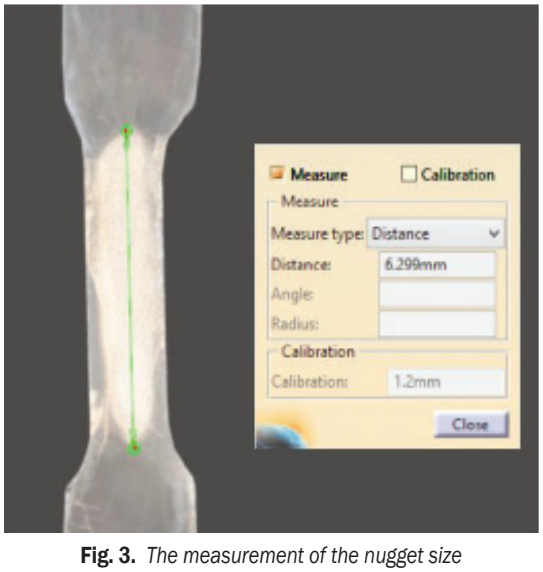

Fig. 3. *The measurement of the nugget size*

Fig. 4. *The SEIFERT X-ray diffractometer model 3000PTS*

3 RESULTS AND DISCUSSION

3.1 The Full Factorial Experiment Design

In this study, a full factorial design of an experiment has been used to design the welding parameters schedule. Electrical current, welding time, and electrode force have been considered to be the main influencing welding parameters. The lower bond of each welding parameter was selected to achieve the nugget size recommended by AWS [26], and the higher bond was chosen to prevent weld splash and spatter. The appropriate ranges of the welding parameters are given in Table 2. The full factorial 2^k design of experiments has been designed, k is the number of variables, which is 3 here with lower and higher bonds of −1 and +1, respectively. According to the full factorial DOE, a total of 8 combinations of the input parameters were considered.

Table 2. *The higher and lower bond of RSW parameters*

	Welding current [kA]	Welding time [cycle]	Electrode force [N]
Higher bond (+1)	12	12	848
Lower bond (−1)	16	16	1130

The samples have been welded based on the welding parameters given in Table 3 and the results

Table 3. *The full factorial DOE*

Sample	Welding current [kA]	Welding time [cycles]	Electrode force [N]	Nugget size [mm]	Maximum residual stress [MPa]
1	12	12	848	4.54	276
2	16	12	1130	5.76	255
3	12	12	1130	4.42	254
4	16	16	1130	6.34	216
5	16	12	848	5.75	280
6	12	16	1130	4.64	213
7	12	16	848	4.68	234
8	16	16	848	6.33	238

obtained from the nugget and the residual stress measurement are displayed in Table 3

Fig. 5 illustrates the results of the DOE analysis for the nugget size. The Pareto diagram shows that although the electrical current, welding time, and their interaction affect the nugget size, the electrode force and its interaction with other variables have almost no effect. In addition, the electrical current is the most influential parameter on the nugget size. The Normal diagram confirms the results obtained from the Pareto diagram. The electrical current is the furthest point from the normal line, which means it is the most significant parameter. The points close to the normal line have no impact on the output. Similar results have been reported in previous studies for other materials **[12]** to **[15]** and **[18]** to **[24]**.

The results of the DOE analysis for the residual stress are displayed in Fig. 6 According to the Pareto and Normal diagrams, the welding time and the electrode force affect the residual stresses. Although the welding time is the most influential parameter on the residual stress, the electrical current has almost no effect. The results are similar to those previously reported for RSW of Al joints **[16]**.

3.2 The Artificial Neural Networks

ANN is a powerful and reliable model to predict complex phenomena with multiple variables. ANN is also very flexible in terms of the number of variables, the training algorithm, transfer functions, and the structure. An ANN consists of several layers: an input layer, some hidden layers, and an output layer. In addition, each layer involves some neurons.

The number of hidden layers is usually one or, in specific cases, two. Using more than two layers is rarely done and is not recommended **[27]**.

Two separate multilayer backpropagation feedforward ANNs have been used to predict the nugget size and the maximum tensile residual stress. Theses ANNs have been implemented using Matlab.

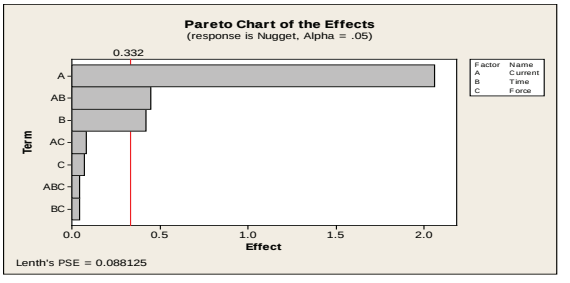

a)

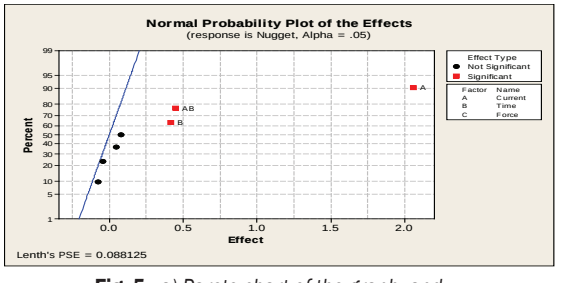

b)

Fig. 5. *a) Pareto chart of the graph, and b) normal probability plot of the effect for the nugget size*

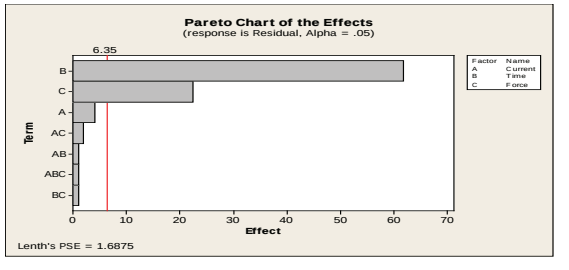

a)

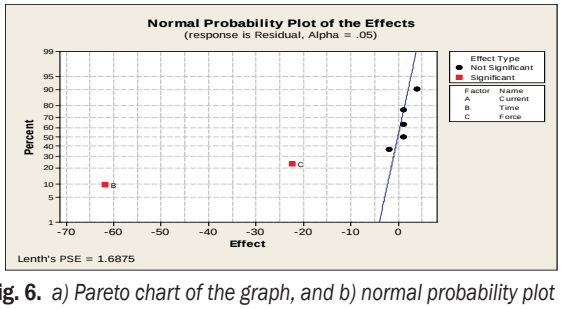

b)

Fig. 6. *a) Pareto chart of the graph, and b) normal probability plot of the effect for the maximum residual stress*

The Levenberg-Marquardt training algorithm has been utilized to train the ANNs. This algorithm minimizes a combination of squared errors and weights and then determines the correct combination. The transfers between layers have been done by using a combination of Tansig and Purelin transfer functions. Finally, the mean square error (MSE) function determines the ability of the ANNs to predict the outputs.

According to the number of the welding parameters and the output, the number of neurons in the input and output layers of both ANNs are three and one, respectively. The performance of the ANNs depends on the number of hidden layers and the number of their neurons. Hence, many trials need to be made to find the optimum structure for the ANN by changing the number of hidden layers and their neurons. Since there were two different ANN, two different structures have been considered. The proper structure for the first ANN to predict the nugget size was 3 6 1. The best structure for the second ANN to predict the maximum residual stress has been found to be 3 10 1 using a trial-and-error procedure. In addition, the values of the variables and outputs have been normalized between 1 and 2 (Eq. (1)) in order to increase the accuracy and speed of training the ANNs.

$$P_n = \frac{P - P_{\min}}{P_{\max} - P_{\min}} + 1, \tag{1}$$

where P is the real value of each parameter, P_n is the normalized value, $P_{\min}$ and $P_{\max}$ are the minimum and maximum values respectively. Eq. (2) also has been used to de-normalize the results obtained from the model.

$$P_n = \frac{P_n - 1}{P_{\max} - P_{\min}} + P_{\min}. \tag{2}$$

According to the DOE results, the electrical current is the most effective parameter on the nugget size, and the welding time has the most influential impact on the residual stress. Although the electrode force has almost no effect on the nugget size, it affects the residual stress. To run the ANNs, the five levels have been considered for both electrical current and welding time and just three levels have been selected for the electrode force. A total of 75 sets of welding parameters have been chosen to run the ANNs. Table 4 displays the level of the RSW parameters considered to run the ANNs. However, the nugget sizes have been measured experimentally; the maximum residual stresses have been obtained from the FE model [6] since the experimental testing would have been time consuming.

Table 4. *The levels of RSW parameters for running the ANNs*

RSW Parameters	Levels
Welding current [kA]	12-13-14-15-16
Welding time [cycles]	12-13-14-15-16
Electrode force [N]	848-990-1130

The overfitting is the usual phenomenon that may occur in the training of ANN. It happens when the ANN memorizes the training data instead of building input-output mapping for the problem. Thus, determining the number of training and test data has a very important role in avoiding overfitting. In this study, approximately 10 % of the total tests (i.e., 7 tests) have been randomly selected as the test data, and the remaining 68 tests have been considered for training data.

Fig. 7 illustrates the results obtained from the training and testing of the first ANN to predict the nugget size. The results indicate that the ANN has been trained successfully, and the first ANN can predict the nugget size very well. Table 5 displays the comparison between the results predicted from the first ANN and the results obtained from the experimental test.

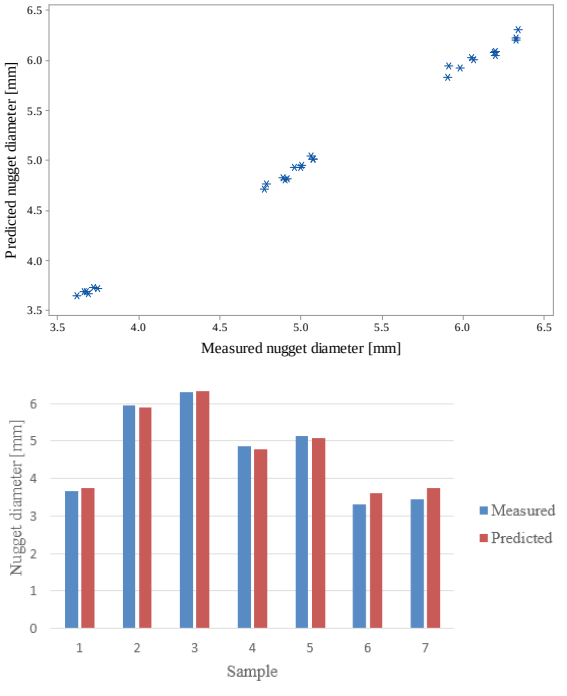

Fig. 7. *The compression results of measured and predicted nugget diameter by the first ANN model a) train samples and b) test*

The results obtained from the second ANN model are almost similar to the first model. The results indicate that the second ANN model can predict the residual stress based on the RSW parameters with high accuracy. Fig. 8 presents the results of the training and testing of the second ANN model.

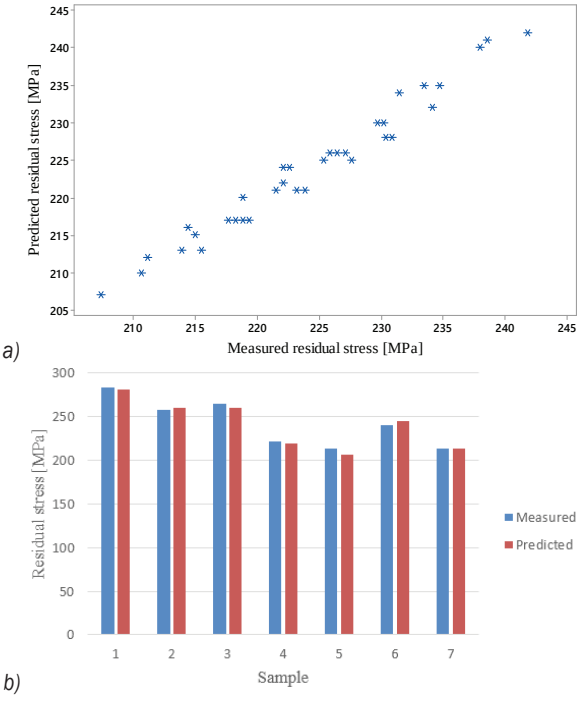

Fig. 8. *The compression results of measured and predicted residual stress by the second ANN model; a) train samples, and b) test*

3.3 The Multi-Objective Genetic Algorithm

The genetic algorithm (GA) is a repeat-based optimization method and its principles are adapted from genetic science. In the GA, a set of design variables are encoded by fixed-length or variable-length strings, which the biological systems refer to them as chromosomes or individuals. GA is based on natural and biological science, and it is widely used to solve optimization problems in engineering.

A non-dominated sorting genetic algorithm II (NSGA II) has been developed to optimize the RSW parameters to obtain a set of desired values for maximizing the nugget size and minimizing the residual stress. Since the GA is the minimizing algorithm, Eq. (3) has been used as the fitness function to achieve the desired goal.

$$MinM = \alpha R - \beta d, \tag{3}$$

where R is the residual stress, d is the nugget size, α and β are the weight coefficients for the residual stress and the nugget size, respectively. Because in this study there is no priority between the nugget size and residual stress, both α and β have been considered 1/2. Thus, the final fitness function is as follows:

$$MinM = 1/2R - 1/2d. \tag{4}$$

The flowchart of the developed multi-objective ANN-ANN-GA algorithm is presented in Fig. 10. The initial population size was 100 and was the same for each generation. According to this presented optimization algorithm, the nugget size and the residual stress were predicted by the ANNs. A different set of RSW parameters were born in each generation, and the nugget size and residual stress were predicted by ANNs inside of the integrated optimization algorithm. A two-point crossover rate of 0.5 and a uniform mutation probability of 0.05 were considered for the GA. In addition, 300 generations were chosen as the maximum generation and the condition for ending the algorithm.

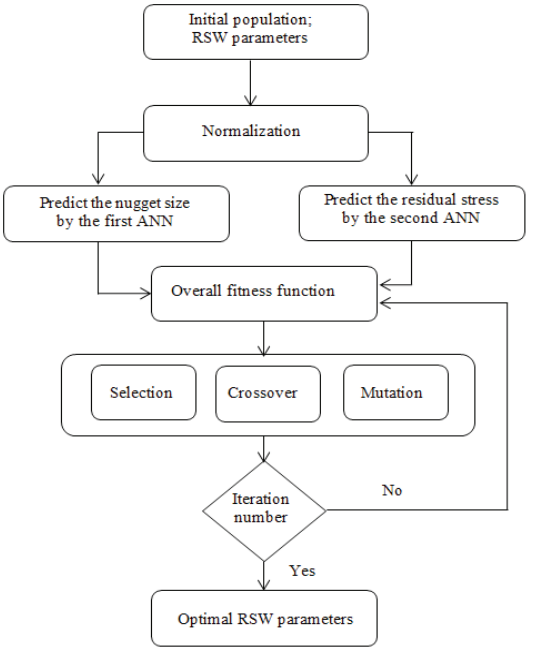

Fig. 10. *The flowchart of the multi-objective ANN-ANN-GA*

Fig. 11 displays the results of running the integrated optimization algorithm. The optimized RSW parameters are displayed in Fig. 12. Since all the variables and outputs have been normalized between 1 and 2, the normalized parameters have been used in both ANNs and multi-objective GA.

Thus, the optimized RSW parameters obtained from the proposed optimization algorithm are between 1 and 2. The real values of optimized RSW parameters are presented in Table 5

Table 5. *The optimized RSW parameters*

Welding parameters	Welding current [kA]	12
	Welding time [cycles]	16
	Electrode force [N]	1130
Nugget size	Measured [mm]	4.74
	Predicted [mm]	4.77
	Error [%]	0.6
Maximum residual stress	Measured [MPa]	213
	Predicted [MPa]	207
	Error [%]	2.8

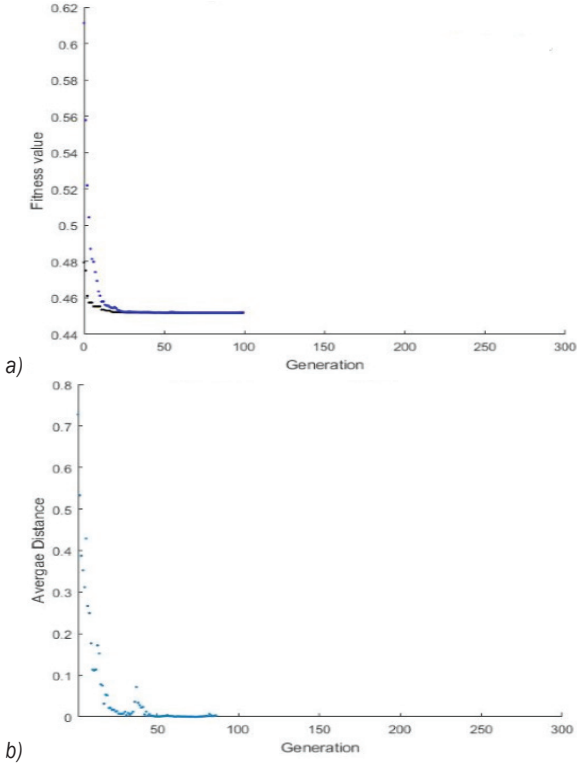

Fig. 11. *The results of the optimization algorithm, a) the best fitness value, b) average distance between individuals*

In order to evaluate the accuracy of the proposed multi-objective GA, a sample was welded based on the optimized RSW parameters. The nugget size and the residual stress were measured experimentally and were compared with the predicted one by the integrated optimization algorithm. Table 5 presents the results of this comparison. The results indicate that the integrated ANN-ANN-GA presented in this study can predict the nugget size and residual stress with high accuracy, and the optimum RSW parameters lead to high strength and good joint quality.

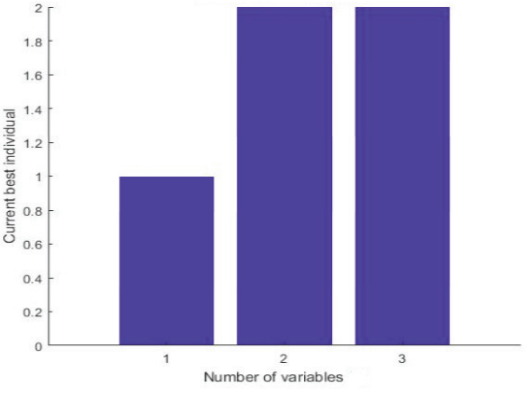

Fig. 12. *The optimized-normalized RSW parameters obtained from the integrated algorithm*

4 CONCLUSIONS

In this study, the RSW parameters of the electric current intensity, welding time, and electrode force have been optimized to achieve the largest nugget along with the lowest tensile residual stress in the RSW of the magnesium alloy AZ61. The full factorial DOE has been employed to investigate the effects of the RSW parameters on the nugget and the residual stress. The results of the DOE have been used to develop two separated ANN models. The ANN models have been utilized to predict the dimensions of the nugget and the maximum tensile residual stress in the welded zone. The results display that the proposed ANNs have a high accuracy in predicting the dimensions of the nugget and the residual stress. Finally, an integrated multi-objective ANN-ANN-GA has been developed to optimize the RSW parameters. The results show that the presented optimization model can be used very well to optimize the RSW parameters.

5 REFERENCES

[1] Danesh Babu, S.D, Sevvel, P., Senthil Kumar, R., Vijayan, V., Subramani, J. (2021). Development of thermo mechanical model for prediction of temperature diffusion in different FSW tool pin geometries during joining of AZ80A Mg alloys. *Journal of Inorganic and Organometallic Polymers and Materials*, vol. 31, p. 3196-3212, **DOI:10.1007/s10904-021-01931-4**.

[2] Cao, X., Jahazi, M., Immarigeon, J.P., Wallace, W. (2006). A review of laser welding techniques for magnesium alloys. *Journal of Materials Processing Technology*, vol. 171, no. 2, p. 188-204, **DOI:10.1016/j.jmatprotec.2005.06.068**.

[3] Chen, F.-K., Huang, T.-B. (2003). Formability of stamping magnesium-alloy AZ31 sheets. *Journal of Materials Processing Technology*, vol. 142, no. 3, p. 643-647, **DOI:10.1016/S0924-0136(03)00684-8**.

[4] Kulekci, M.K. (2008). Magnesium and its alloys applications in automotive industry. *The International Journal of Advanced Manufacturing Technology*, vol. 39, p. 851-865, **DOI:10.1007/s00170-007-1279-2**.

[5] Li, Q., Yu, Q., Zhang, J., Jiang, Y. (2010). Effect of strain amplitude on tension-compression fatigue behavior of extruded Mg6Al1ZnA magnesium alloy. *Scripta Materialia*, vol. 62, no. 10, p. 778-781, **DOI:10.1016/j.scriptamat.2010.01.052**.

[6] Sevvel, P., Jaiganesh, V. (2015). Effect of tool shoulder diameter to plate thickness ratio on mechanical properties and nugget zone characteristics during FSW of dissimilar Mg alloys. *Transactions of the Indian Institute of Metals*, vol. 68, p. 41-46, **DOI:10.1007/s12666-015-0602-0**.

[7] Xu, N., Ren, Z., Lu, Z., Shen, J., Song, Q., Zha, J., Bao, J. (2022). Improved microstructure and mechanical properties of friction stir-welded AZ61 Mg alloy joint. *Journal of Materials Research and Technology*, vol. 18, p. 2608-2619, **DOI:10.1016/j.jmrt.2022.03.160**.

[8] Sahu, P.K., Pal, S. (2017). Influence of metallic foil alloying by FSW process on mechanical properties and metallurgical characterization of AM20 Mg alloy. *Materials Science and Engineering: A*, vol. 648, p. 442-455, **DOI:10.1016/j.msea.2016.12.081**.

[9] Satheesh, C., Sevvel, P., Senthil Kumar, R. (2020). Experimental identification of optimized process parameters for FSW of AZ91C Mg alloy using quadratic regression models. *Strojniški vestnik - Journal of Mechanical Engineering*, vol. 66, p. 736-751, **DOI:10.5545/sv-jme.2020.6929**.

[10] Zhang, L., Zhang, H., Lei, X., Wang, R., Han, B., Zhang, J., Na, S. (2020). Laser processing of Mg-10Li-3Al-3Zn alloy: Part I - Microstructure and properties of laser welded joints. *Journal of Manufacturing Processes*, vol. 57, p. 871-880, **DOI:10.1016/j.jmapro.2020.07.053**.

[11] Huang, Y. Shen, C., Ji, X., Li, F., Zhang, Y., Hua, X. (2020). Effects of Mg content on keyhole behavior during deep penetration laser welding of Al-Mg alloys. *Optics & Laser Technology*, vol. 125, art. ID 106056, **DOI:10.1016/j.optlastec.2020.106056**.

[12] Pouranvari, M., Asgari, H.R., Mosavizadeh, S.M., Marashi, P.H., Goodarzi, M. (2007). Effect of weld nugget size on overload failure mode of resistance spot welds. *Science and Technology of Welding and Joining*, vol. 12, no. 3, p. 217-225, **DOI:10.1179/174329307X164409**.

[13] Pouranvari, M., Marashi, P. H. (2010). On the failure of low carbon steel resistance spot welds in quasi-static tensile-shear loading. *Materials and Design*, vol. 31, no. 8, p. 3647-3652, **DOI:10.1016/j.matdes.2010.02.044**.

[14] Afshari, D., Sedighi, M., Barsoum, Z., Peng, R.L. (2012). An approach in prediction of failure in resistance spot welded aluminum 6061-T6 under quasi-static tensile test. *Journal of Engineering Manufacture*, vol. 226, no. 6, p. 1026-1032, **DOI:10.1177/0954405411435198**.

[15] Hassanifard, S., Zehsaz, M. (2010). The effects of residual stresses on the fatigue life of 5083-0 aluminum alloy spot welded joints. *Procedia Engineering*, vol. 2, no. 1, p. 1077-1085, **DOI:10.1016/j.proeng.2010.03.116**.

[16] Afshari, D., Sedighi, M., Karimi M.R., Barsoum, Z. (2013). On residual stresses in resistance spot-welded aluminum alloy 6061-T6: experimental and numerical analysis. *Journal of Materials Engineering and Performance*, vol. 22, p. 3612-3619, **DOI:10.1007/s11665-013-0657-1**.

[17] Afshari, D., Mirzaahmadi, S., Barsoum, Z., (2019). Residual stresses in resistance spot welded AZ61 Mg alloy. *Computer Modeling in Engineering and Sciences*, vol. 118, no. 2, p. 275-290, **DOI:10.31614/cmes.2019.03880**.

[18] Luo, Y., Liu, J., Xu, H., Xiong, C., Liu, L., (2009). Regression modeling and process analysis of resistance spot welding on galvanized steel sheet. *Materials and Design*, vol. 30, no. 7, p. 2547-2555, **DOI:10.1016/j.matdes.2008.09.031**.

[19] Hamidinejad, S. M., Kolahan, F., Kokabi, A. H. (2012). The modeling and process analysis of resistance spot welding on galvanized steel sheets used in car body manufacturing. *Materials and Design*, vol. 34, p. 759-767, **DOI:10.1016/j.matdes.2011.06.064**.

[20] Muhammad, N., Manurung, Y., Jaafar, R., Abas, S.K., Than; G., Haruman, E. (2013). Model development for quality features of resistance spot welding using multi-objective Taguchi method and response surface methodology. *Journal of Intelligent Manufacturing*, vol. 24, p. 1175-1183, **DOI:10.1007/s10845-012-0648-3**.

[21] Zhao, D., Wang, Y., Sheng, S., Lin, Z. (2014). Multi-objective optimal design of small scale resistance spot welding process with principal component analysis and response surface methodology. *Journal of Intelligent Manufacturing*, vol 25, p. 1335-1348, **DOI:10.1007/s10845-013-0733-2**.

[22] Pashazadeh, H., Gheisari, Y., Hamedi, M. (2016). Statistical modeling and optimization of resistance spot welding process parameters using neural networks and multi-objective genetic algorithm. *Journal of Intelligent Manufacturing*, vol. 27, p. 549-559, **DOI:10.1007/s10845-014-0891-x**.

[23] Mirzaei, F., Ghorbani, H., Kolahan, F. (2017). Numerical modeling and optimization of joint strength in resistance spot welding of galvanized steel sheets. *The International Journal of Advanced Manufacturing Technology*, vol. 92, p. 3489-3501, **DOI:10.1007/s00170-017-0407-x**.

[24] Valera, J., Miguel, V., Martinez, A., Naranjo J., Canas, M. (2017). Optimization of electrical parameters in resistance spot welding of dissimilar joints of micro-alloyed steels TRIP sheets. *Procedia Manufacturing*, vol. 13, p. 291-298, **DOI:10.1016/j.promfg.2017.09.074**.

[25] Vignesh, K., Perumal, A.E., Velmurugan, P. (2017). Optimization of resistance spot welding process parameters and microstructural examination for dissimilar welding of AISI 316L austenitic stainless steel and 2205 duplex stainless steel. *The International Journal of Advanced Manufacturing Technology*, vol. 93, p. 455-465, **DOI:10.1007/s00170-017-0089-4**.

[26] American national standard, ANSI/AWS/SAE. (1997). *Weld Button Criteria, Recommended Practice for Test Methods for Evaluating the Resistance Spot Welding Behavior of Automotive Sheet Steel Metal*. AWS, New York.

[27] Hagan, M.T., Demath H.B., Beale, M. (1996). *Neural Network Design*. PSW Publication, Boston.

Strojniški vestnik - Journal of Mechanical Engineering 68(2022)7-8, 493-505
DOI:10.5545/sv-jme.2022.142
Original Scientific Paper
Received for review: 2022-03-31
Received revised form: 2022-05-30
Accepted for publication: 2022-06-01

Effect of Dual-stage Ageing and RRA Treatment on the Three-body Abrasive Wear of the AW7075 Alloy

Marzena M. Lachowicz* – Tadeusz Leśniewski – Maciej B. Lachowicz
Wroclaw University of Science and Technology, Faculty of Mechanical Engineering, Poland

The paper presents an analysis of the influence of the heat treatment state on the abrasive wear of the AW7075 aluminium alloy. To determine the hardening state, the material hardness was measured. It was found that hardness is not the only factor that influences this type of wear. For this reason, the influence of the emerging microstructure is also analysed in the considerations. After tribological tests, microscopic observations of surface features were carried out to determine the dominant mechanisms of surface damage. The results were extended by the hardness distribution carried out on the cross-section. There were no changes in hardness that could be related to either strain hardening or structural changes caused by friction.

Keywords: aluminium alloys, AW7075, abrasive wear, heat treatment, hardness, microstructure

Highlights

- *The hardness of the AW7075 alloy is not the only determinant of abrasive wear; with the microstructure of the tested alloy and the related heat treatment, the state also plays an important role in this respect.*
- *The abrasive wear of the tested alloy can be ranked in the following order according to the heat treatment condition: dual ageing < RRA treatment < T6 state.*
- *The wear features show a similar type of damage, regardless of the heat treatment state. Scratches, grooves, microcracks, and slight plastic deformation features be observed on the wear surface.*
- *Decohesion developed mainly around grain boundaries and interfacial boundaries, which facilitates the loss of continuity with the matrix in the presence of coherent particles. Larger and incoherent precipitates in the matrix can act as an abrasive and increase the wear rate.*
- *The presence of large particles of the primary phases, which do not dissolve at the stage of heat treatment, promotes their crushing and defragmentation during abrasive wear.*
- *The surface hardness does not change due to the occurrence of mechanical effects resulting from friction.*

0 INTRODUCTION

There is relative movement between surfaces of components in some applications of aluminium alloys. Wear resistance then becomes an important property to consider. Numerous research studies show that heat treatment can have a significant impact on tribological wear. In particular, the fragmentation of the microstructure components can significantly affect the obtained tribological parameters [1] to [3].

The presence of intermetallic phases in the microstructure offers a wide spectrum of possibilities for the strengthening of aluminium alloys. This group also includes the high-strength 7000 series alloys. Two treatments are used for this purpose: supersaturation and subsequent ageing. The sequence for ageing the 7000 series alloys is given as follows: solid solution (α) → Guinier-Preston (GP) zones → η' ($MgZn_2$) → η ($MgZn_2$) [4] and [5]. The typical hardness-ageing diagram for a heat-treatable aluminium alloy is shown in Fig. 1. GP zones are formed during ageing at room temperature or the early stages of ageing. They are fully coherent with the matrix. The greatest hardening effect is achieved at the stage of separation of the intermediate phase, which is related to the change in the mechanism of the interaction of the precipitates with dislocations. This is a typical T6 state. The stresses that are needed to cut the particles by dislocation, as well as the stresses caused by the Orowan mechanism associated with the formation of a dislocation loop around these precipitates, obtain their maximum values. The material hardness drops significantly when there is a complete loss of the coherence of the precipitates. Ageing to the T6 state is associated with a continuous distribution of grain boundary precipitates (GBPs) [6] and [7]. A properly carried out heat treatment should end at the stage of forming the matrix of precipitates (MPs), which is partially coherent with the intermediate phase η'.

The T6 state is characterized by high strength and hardness but is highly susceptible to stress corrosion cracking. When looking for greater resistance to this type of corrosion, dual-stage ageing (DA) and Retrogression and Re-Ageing (RRA) treatment are used [9] to [13]. The first stage of DA ageing is characterized by a lower temperature when compared

*Corr. Author's Address: Wroclaw University of Science and Technology, Faculty of Mechanical Engineering, Department of Metal Forming, Welding Technology and Metrology, Lukasiewicza 7-9, 50-371 Wroclaw, Poland, marzena.lachowicz@pwr.edu.pl

to conventional ageing, and it is responsible for the diffusion and homogeneous distribution of the GP zones. The coarse-grained GP zones and phases are formed during the second ageing and contribute to the peak hardness. MPs are coarser and partially incoherent with phase η when compared to one-step ageing. This helps to reduce the hardness of the alloy [12] and [13]. Another solution is the multi-stage RRA heat treatment. Retrogression involves heating the alloy, which had earlier been hardened, at a temperature in the range of 200 ºC to 2θ ºC for a short period (2θ s), and then re-ageing the alloy to a condition typical for the T6 state. The use of the RRA treatment leads to the obtaining of a microstructure that is characterized by the presence of fine-dispersed and coherent η' ($MgZn_2$) MPs. They are characteristic of the T6 state. However, at the GBPs there are fragmented and discontinuous precipitations that are typical for T7 over-ageing. As a result, the grain boundary that is line blocked with continuous GBPs particles, as in the T6 state, is transformed into a state in which the precipitates of the η phase are coarse and discontinuous [9], [14], and [15]. After the RRA treatment, a larger fraction of the GBPs was observed [7]. Also, the copper content of GBPs increases with the time of heat treatment [6].

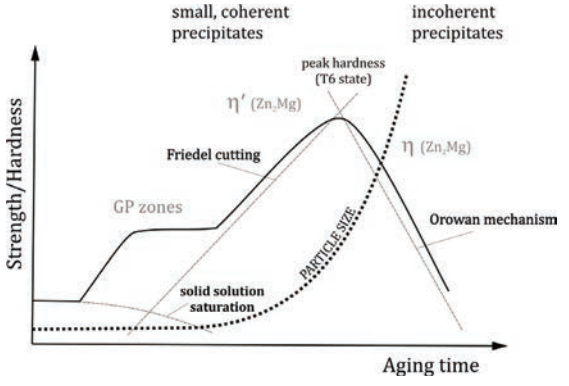

Fig. 1. *Schematic illustration of the precipitate strengthening contributions as a function aging time (based on [8])*

The effect of heat treatment of aluminium alloys on their strength is already known. Its influence on the resistance to structural corrosion is also well understood [12] to [16]. Retrogression and re-ageing treatment improve the resistance to stress corrosion cracking (SCC) [6], while maintaining high strength, until the MPs become coarse [6]. However, the microstructure changes caused by heat treatment affect other functional properties of aluminium alloys. The high strength is maintained as long as the MPs are not coarse [6]. The RRA state is characterized by high resistance to fatigue crack initiation and better impact toughness as a result of the increased discretion of the precipitates occurring at the grain boundaries [9], [17] and [18]. Coarse GBPs also increase electrical conductivity [9]. The DA state, in terms of microstructure, brings the alloy closer to the over-ageing condition, which in turn results in a reduction in strength and an increase in ductility [19]. It seems obvious that the different hardnesses obtained for individual states should also affect the tribological wear. For this reason, in the present study, it was decided to consider the influence of microstructure on the abrasive wear of the AW 7θ7a luminium alloy.

1 MATERIAL AND METHODS

The tests were carried out on the AW 7θ7 aluminium alloy. The chemical composition of the alloy, which was determined by GDS-θ0A Leco glow discharge optical spectrometry (GD OES), is shown in Table 1

In the microstructure of all the tested samples, α(Al) solid solution was observed with grey, large precipitates of the α-AlFeMnSi phase, and dark primary precipitates of the Mg_2Si phase (Fig. 2). The type of these particles was determined on the basis of the EDS results conducted as part of the preliminary studies and compared with the literature data. The grains of the solid solution were heterogeneous in nature and were surrounded by large precipitates of the iron-rich phase. The main changes in the microstructure, which were caused by the applied heat treatment, concern the morphology, size, quantity, and coherence of the formed precipitates. For this reason, the microstructure of the material in the image of the light microscope was of a similar nature. These changes are subtle and can, therefore, only be observed with the use of transmission electron microscopy (TEM) methods. However, it can be seen that in the case of the DA state, the precipitations of the strengthening phases are more clearly visible, which indicates their larger dimensions.

Table 1. *Chemical composition of the tested AW7075 aluminium alloy*

Element	Zn	Mg	Cu	Fe	Cr	Si	Mn	Ti	Al
Content [%]	5.42	2.34	1.45	0.39	0.26	0.12	0.10	0.03	rest

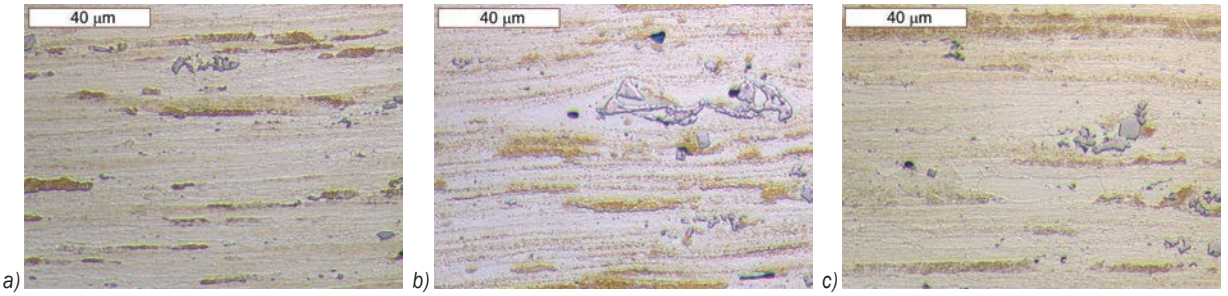

Fig. 2. *Microstructure after; a) T6, b) DA, and c) RRA, light microscopy, etched with 10 % HF*

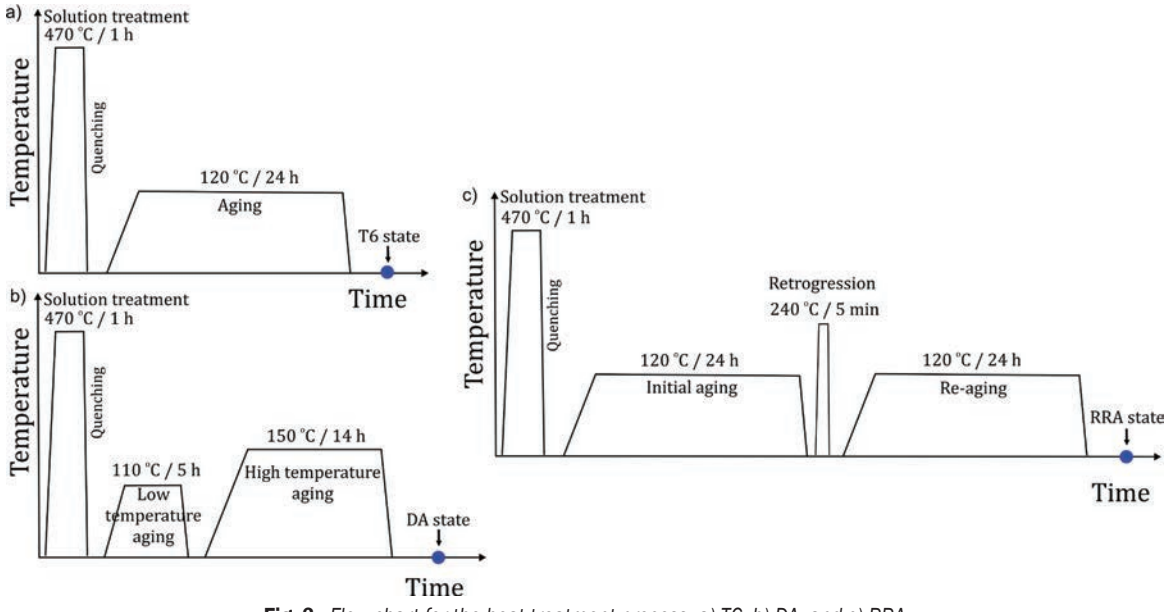

Fig. 3. *Flow chart for the heat treatment process; a) T6, b) DA, and c) RRA*

The parameters of three various heat treatments were developed for 0 mm × 00 mm sections with a thickness of 10 mm that were cut from the tested alloy (Fig. 3). The microstructure was investigated on conventionally prepared metallographic microsections using a Leica DM600M light microscope. The tests were carried out before and after etching with a 0 % aqueous solution of HF. To determine the material hardening, BHN hardness measurements were carried out using the Brinell method and a DuraJet G5 hardness tester (Struers).

To determine the abrasive wear resistance, tests were carried out on the T-07 tester made at the Institute of Sustainable Technology in Radom (Poland). The tribological tests were performed in the presence of the loose F60 electro-corundum abrasive, and all the tested samples were subjected to the same friction conditions. The used abrasive reflects the penetration of aluminium oxide or anodic coatings into the friction area very well. The oxide film is thin and can break off easily, in turn producing wear debris particles. The removal of the protective layer also accelerates the corrosive effects [20]. The method complied with the requirements of the GOST 2320 8 9 tandard [21].

The tested system consisted of a sample (plate) made of the tested material, and a counter-sample (roll) with a rubber ring. During the test, the material sample was pressed with a defined force of (F_N) to a rubber disk with a diameter of d = 50 mm, which was rotating at a constant speed (n). Gravity was used to deliver a loose abrasive between the rotating disc and the fixed sample. In the presence of loose abrasive, the sample of the tested materials and the reference sample were subjected to abrasive wear under the used operating conditions, i.e., rotational speed n = 60 rpm/min, test time t, and F_N loads in accordance with the above standard (t = 10 min, F = 44 N). The reference sample was grade C45 normalized steel. Next, the mass loss of the reference sample (Z_{ww}) and the mass loss of the tested materials (Z_{wb}) were

determined. The mass loss of the samples (weight difference before and after the tests) was determined after a defined test time (determined by the number of rotations of the rubber roller). Based on the mass loss measurements, the abrasive wear resistance index K_b (relative wear resistance) was calculated from the following equation (Eq. (1)):

$$K_b = \frac{Z_{ww} \cdot \rho_b \cdot N_b}{Z_{wb} \cdot \rho_w \cdot N_w}, \quad (1)$$

where Z_{ww} is the mass loss of the reference material (C45 steel), Z_{wb} the mass loss of the tested material, ρ_w the density of the reference material, ρ_b the density of the tested material, N_w the number of revolutions of the reference material's friction path, and N_b the number of revolutions of the tested material's friction path. The density of the tested material (AW 7075) was 2.8 g/cm³.

The morphology of the specimens after the tribological tests was observed using scanning electron microscopy (SEM), which also identified the wear features. The Phenom World ProX microscope was used for this purpose. Backscattered electrons (BSE) and second electrons (SE) detectors with an accelerating voltage of 15 kV were used.

2 RESULTS AND DISCUSSION

2.1 Hardness Measurements

Based on the performed measurements, it can be stated that the proposed heat treatment contributed to the material strengthening (Fig. 4). It was found that the Brinell hardness (BHN) of the AW 7075 alloy increases in the following order: DA<T6<RRA. The highest hardness of the AW 7075 alloy was obtained after the RRA heat treatment, while the alloy that was heat treated to the T6 state had a slightly lower hardness. The use of double-stage ageing adversely affected the alloy strengthening, with the hardness after this process being the lowest.

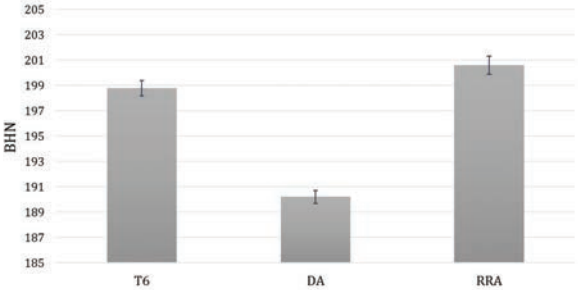

Fig. 4. *Results of hardness measurements of the AW 7075 alloy after various heat treatments*

2.2 Abrasive Wear

The AW 7075 aluminium alloy, with different levels of hardness obtained by heat treatment, was tested. Figs. 5 and 6 present the three-body dry abrasion of the AW 7075 alloy, which was determined as the weight loss for its heat-treated state. The results of the hardness and abrasive wear measurements can be summarized as follows:

- the abrasive wear kinetics of the T6 state were lower than for the DA and RRA states,
- the DA and RRA states, despite having different hardness values, had a comparable wear resistance,
- the hardest sample (RRA state) had worse wear resistance than the one with lower hardness (T6 state).

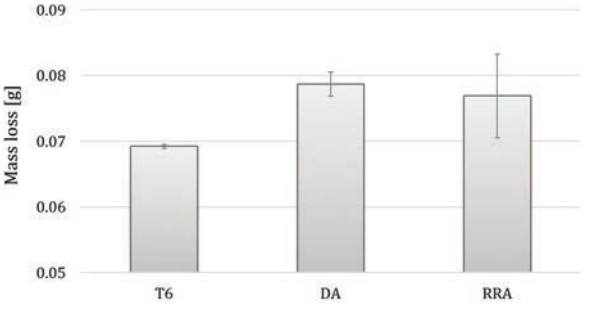

Fig. 5. *Mass loss (Z_{wb}) results obtained for the AW 7075 alloy after various heat treatments*

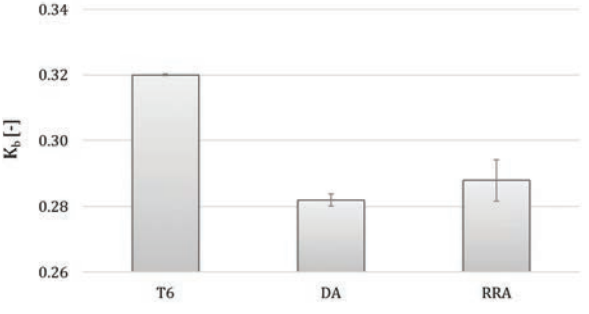

Fig. 6. *K_b factor obtained for the AW 7075 alloy after various heat treatments*

Linear wear low theory (also called Archard's equation) indicates the relationship between the hardness of the material and its abrasive wear resistance. In the case of the alloys in the DA state with the lowest hardness, the greatest weight loss, and thus the lowest wear resistance, was observed. However, in the remaining cases, this relationship did not work. Other authors also note that the correlation between hardness and wear resistance is not always

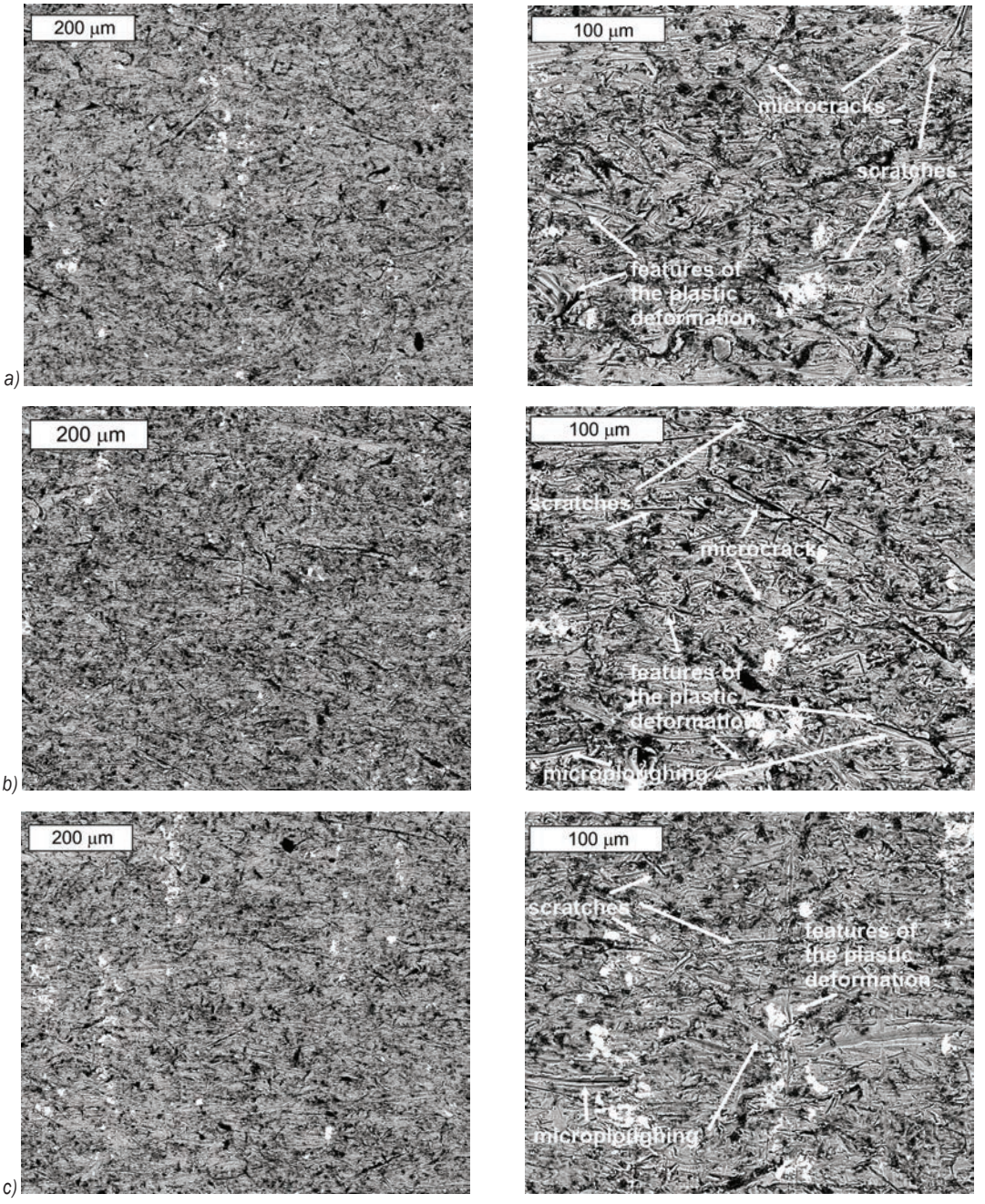

Fig. 7. *General views of the wear features after the different heat treatments; a) T6, b) DA, and c) RRA, SEM*

clear [22] to [24]. However, Archard did not consider the role of the microstructure as one of the key factors in abrasive wear.

The conducted research shows that the hardness of the AW 7075 alloy is not the only factor that determines its wear. No linear relationship was observed between the hardness of the material and its wear; therefore, it can be concluded that the wear is also determined by the microstructure of the material. From the point of view of the microstructure, aluminium alloys can be considered as "composites" that consist of a soft matrix and hard precipitates formed during the heat treatment stage, which in turn affect the hardness and strength of these alloys. The presence of hard particles in the matrix effectively reduces wear [25] and [26]. Microstructural parameters (e.g., the hardness, shape, size, volume fraction, and distribution of the second phases), the properties of

the matrix, and the interfacial bonding between the second phase and the matrix significantly influence the abrasive wear resistance [27]. Even a subtle change in the size and distribution of these precipitates can significantly affect the AW7075 alloy's operational properties.

It is not difficult to observe that the wear was lower in the states in which the microstructure mainly shows significant precipitation that is coherent with the matrix (T6 state). Literature data clearly indicate that in the T6 condition, GBPs are mainly continuous and coherent particles [6] and [7]. The hardening peak caused by the presence of coherent phases is also confirmed by hardness measurements (Fig. 4). During micro-ploughing, the metallic material is mainly elastically-plastically deformed, and it flows around and beneath the sliding particle [27]. In an ideal case, micro-ploughing, due to a single pass of one abrasive particle, does not result in any detachment of material from the wearing surface. A prow is formed ahead of the abrading particle, and the material is continuously displaced sideways to form ridges adjacent to the produced groove. As shown in Fig. 1, the particles coherent with the matrix will be sheared in accordance with the Friedel effect. This is conducive to maintaining the continuity of the matrix as well as the precipitations. Consequently, these particles are more difficult to detach from the matrix. In this situation, the wear will be mainly caused by foreign abrasive particles that are involved in the abrasion, which contributes to reduced consumption and higher K_b ratios. For both the RRA treatment and the T6 state, the particles that are partially coherent with the matrix constitute a significant contribution to the microstructure. The high degree of strengthening after RRA treatment is confirmed by high hardness (Fig. 4). However, after RRA treatment, the MPs are similar to those occurring in the T6 state [6], [7], [9], [14], and [15]. The grain boundaries are close to the over-ageing state. The GBPs consist of incoherent, discontinuous, and coarse precipitations [6], [7], [9], [14], [15], and [19]. In a situation in which a significant amount of precipitation is incoherent with the matrix, their presence in the microstructure may contribute to the decohesion of the material. However, it has been proved that a too high concentration of MPs deteriorates the resistance to stress corrosion cracking [6]. Material may be ploughed aside repeatedly by displacing particles, which may then detach due to micro-fatigue. The precipitations torn out in this

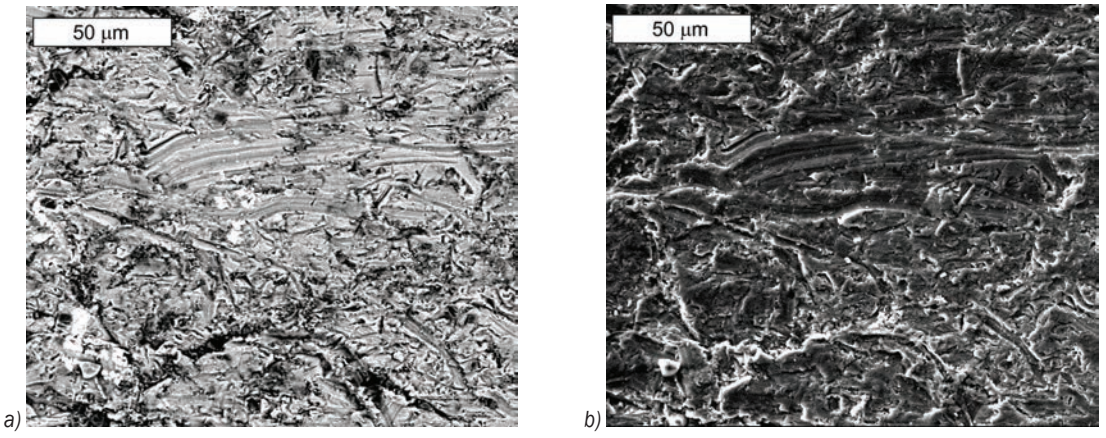

a) b)

Fig. 8. *Wear morphology after the T6 heat treatment; SEM; a) BSE, and b) SE*

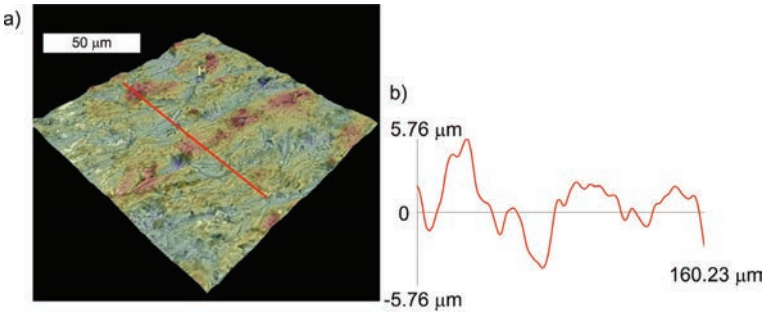

Fig. 9. *a) Exemplary SEM 3D-profilometry image, and b) surface texture of the wear tracks after the T6 heat treatment*

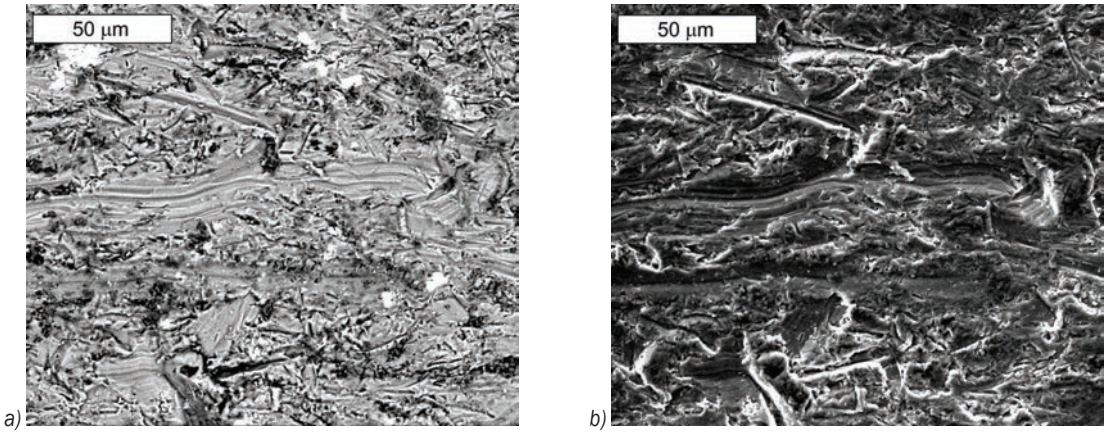

Fig. 10. *Wear morphology after DA, SEM a) BSE, and b) SE*

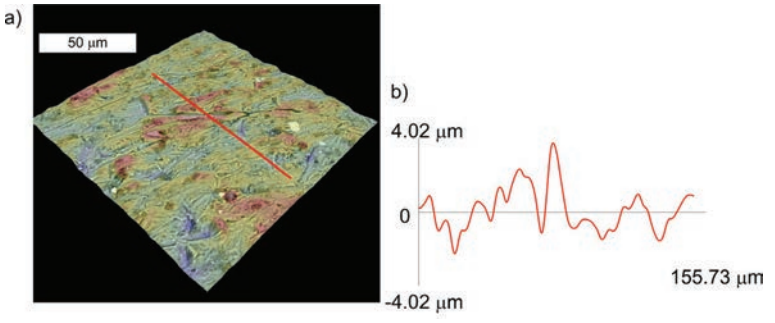

Fig. 11. *a) Exemplary SEM 3D-profilometry image, and b) the surface texture of the wear tracks after the DA heat treatment*

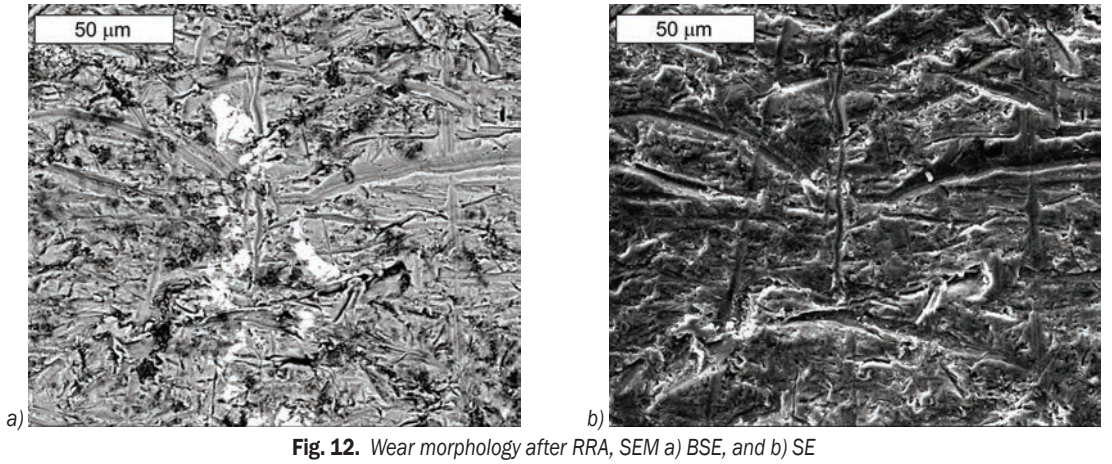

Fig. 12. *Wear morphology after RRA, SEM a) BSE, and b) SE*

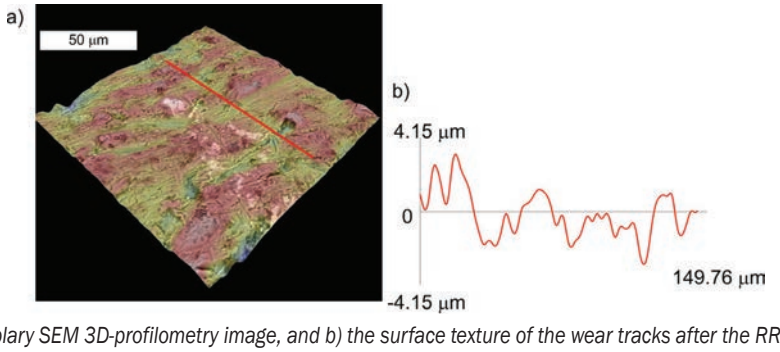

Fig. 13. *a) Exemplary SEM 3D-profilometry image, and b) the surface texture of the wear tracks after the RRA heat treatment*

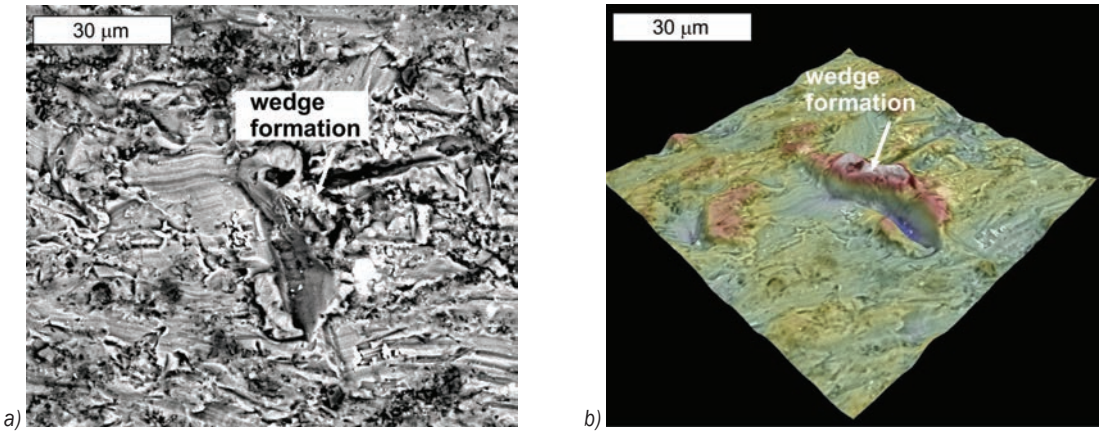

Fig. 14. *Wear morphology after DA; the wedge formation is visible locally; a) SEM image, and b) SEM 3D-profilometry image*

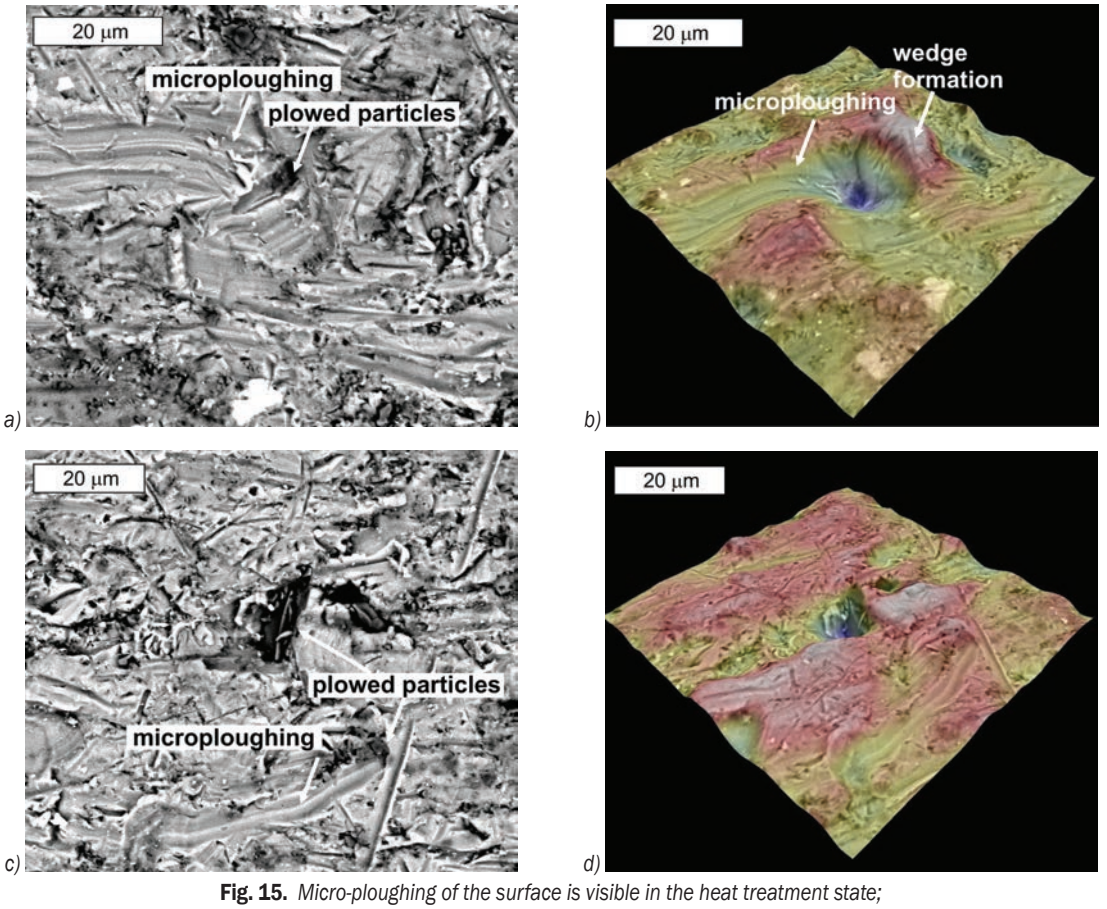

Fig. 15. *Micro-ploughing of the surface is visible in the heat treatment state; a) DA, SEM image, b) DA, SEM 3D-profilometry image, c) RRA, SEM image, and d) RRA, SEM 3D-profilometry image*

way, while moving in the mass of the material, may contribute to increased wear. Volume loss may occur as a result of the action of many abrasive particles.

2.3 Wear Surface

To understand the reason for the different wear mechanisms better and to study the influence of matrix hardness on the wear performance, the morphology of the wear track was examined using SEM analysis.

The analyses of the wear paths revealed the same type of damage in all the tested alloy states (Fig. 7), with the wear being abrasive. As shown in the images obtained at higher magnifications: grooves and scratches, microcracks, and plastic deformation can be easily observed on the surface of the wear tracks (Figs. 8 to 13). The resulting surface irregularities ranged from 4 µm to 6 µm, regardless of the heat treatment condition (Figs. 9, 11 and 13). The main wear mechanisms are therefore controlled by wedge formation and micro-ploughing (Figs. 14 and 15). However, this causes a large amount of ploughed material to embed into the matrix at the edge of the wear mark, which makes a significant contribution to material fatigue. Moreover, the abrasive material cuts the surface of the matrix. The grooves and scratches that are formed are not always parallel to the direction of friction, which indicates the displacement of the friction particles in the wear area (Fig. 7). The precipitations can increase hardness, but at the same time enhance the wear rate by causing disruption of plastic flow during particle impact. The larger ones can also act as an abrasive and, in turn, increase the wear rate during abrasion.

2.4 Subsurface Wear Morphology of the Samples and Microhardness Measurements

Observations of the wear surface carried out on the cross-section confirm the presented thesis (Figs. 16 to 20). In the case of the DA state, more even wear was observed but, at the same time, it was often accompanied by delamination, which in turn contributed to the removal of larger fragments of the wear material (Figs. 18 and 19). It is unlikely that the fragments observed in the microscopic image came from surface micro-cutting, as this mechanism was not observed on the surface in the SEM investigations. This undoubtedly contributed to the greater wear observed during the tribological tests.

As indicated earlier, the key factor was the microstructure. Observations on the perpendicular cross-section of the samples showed that decohesion developed mainly in the area of the grain boundaries and interfacial boundaries (Figs. 16, 18 and 20c). The loss of continuity with the matrix is much easier in the case of non-coherent particles than in the presence of coherent precipitations. The tendency for intergranular crack growth is an effect of planar slip band development results from the repeated shearing of precipitates by dislocation motion [28].

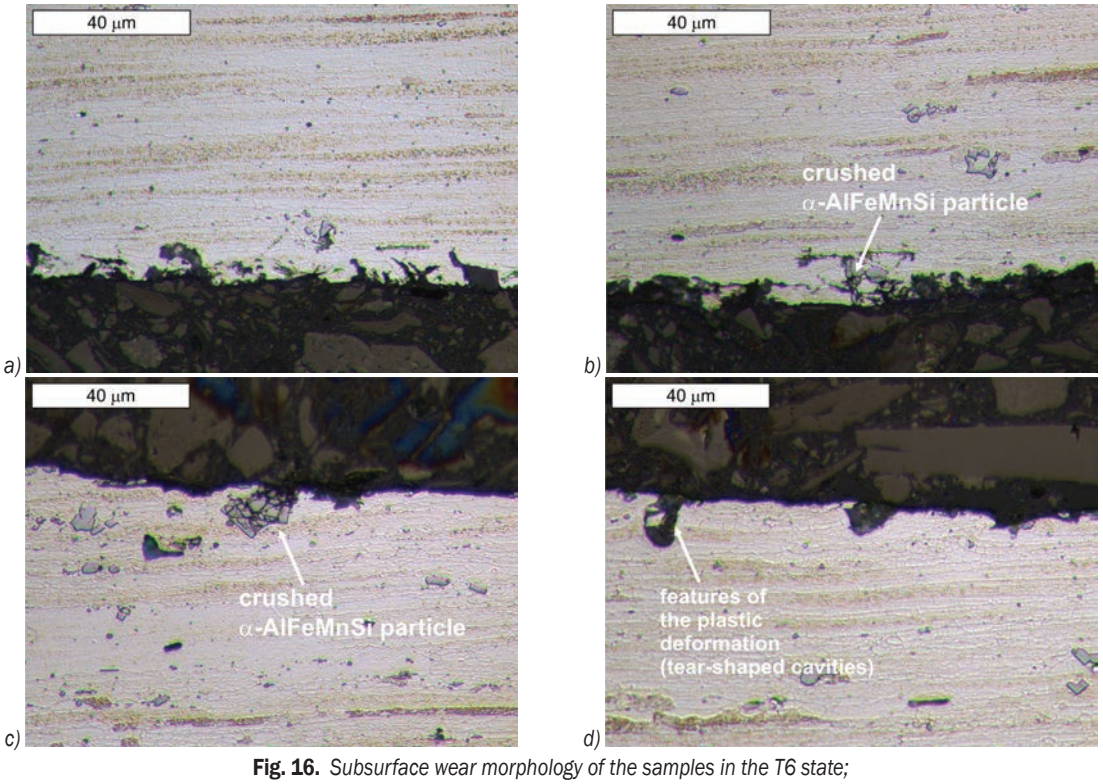

Fig. 16. *Subsurface wear morphology of the samples in the T6 state; a) and b) perpendicular, and c) and d) and parallel to the sliding direction; Light microscopy, etched with 10 % HF*

In the T6 state, which is formed mainly by coherent precipitations [4] and [29], changes typical for surface scratching and micro-ploughing were observed (Figs. 16 and 17). Although changes in the direction of the features that formed on the surface of the samples were observed, the greatest changes in the cross-section occurred in the direction perpendicular to the sliding (Figs. 16a and b). The nature of the subsurface wear morphology observed in the RRA state was similar to those in the T6 state (Fig. 20). Regardless of the heat treatment states, microstructure evolution caused by plastic deformation was not observed. Small effects of plastic deformation were observed in the places where the abrasive was pressed into the surface of the samples, which led to the formation of characteristic tear-shaped cavities (Figs. 16a and 19). In all the samples, it was also observed that the presence of the α-AlFeMnSi particles in the subsurface area leads to

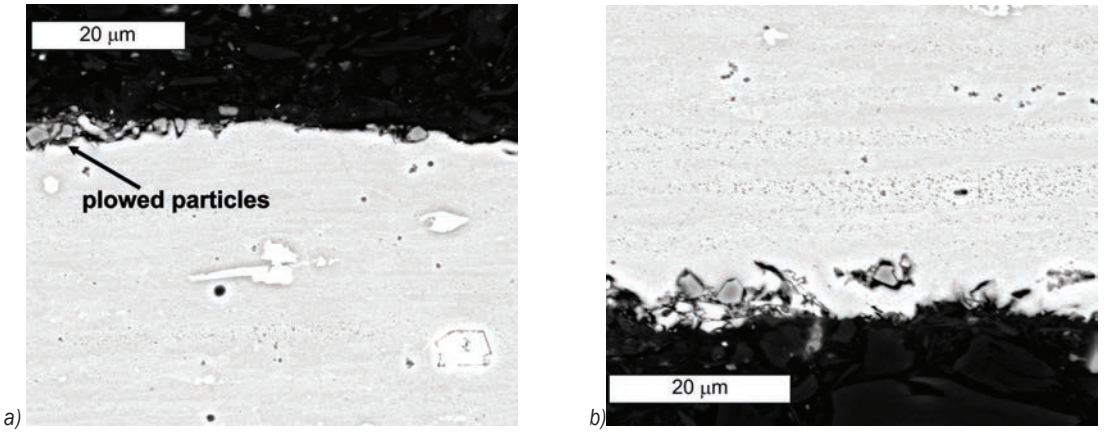

Fig. 17. *Subsurface wear morphology of the samples in the T6 state; a) parallel to the sliding direction, and b) perpendicular to the sliding direction, SEM, etched with 10 % HF*

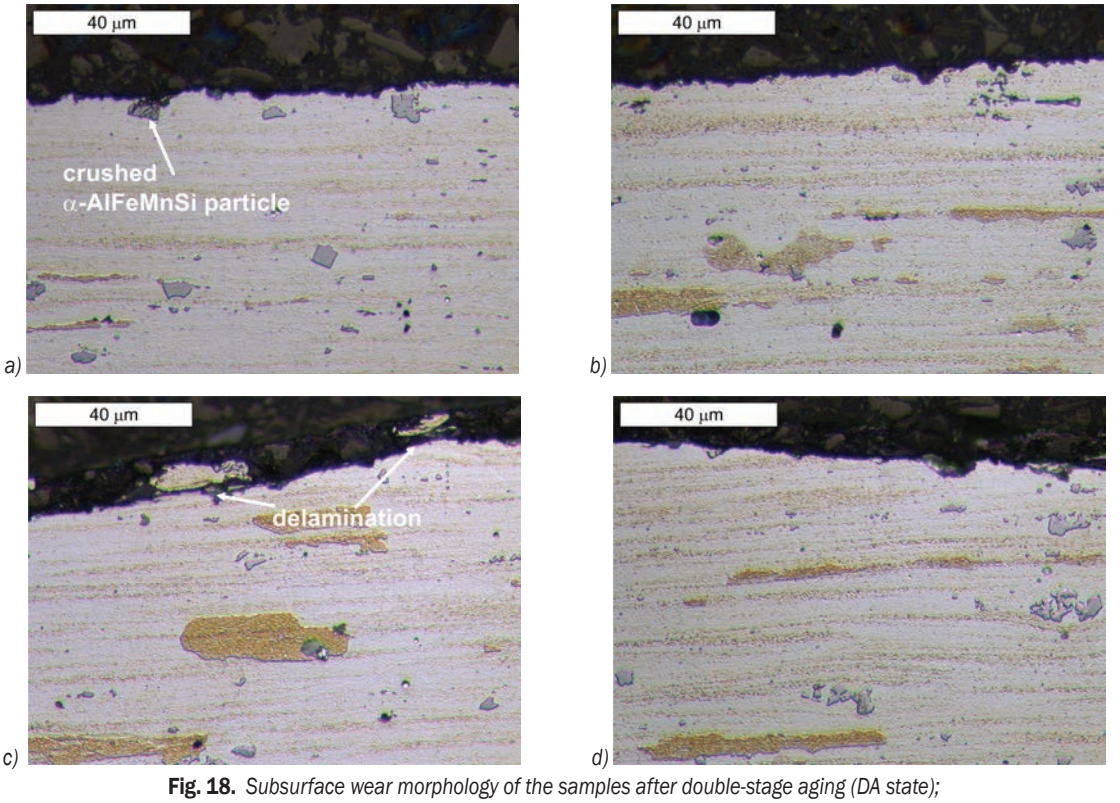

Fig. 18. *Subsurface wear morphology of the samples after double-stage aging (DA state); a) and b) perpendicular, and c) and d) parallel to the sliding direction; Light microscopy, etched with 10 % HF*

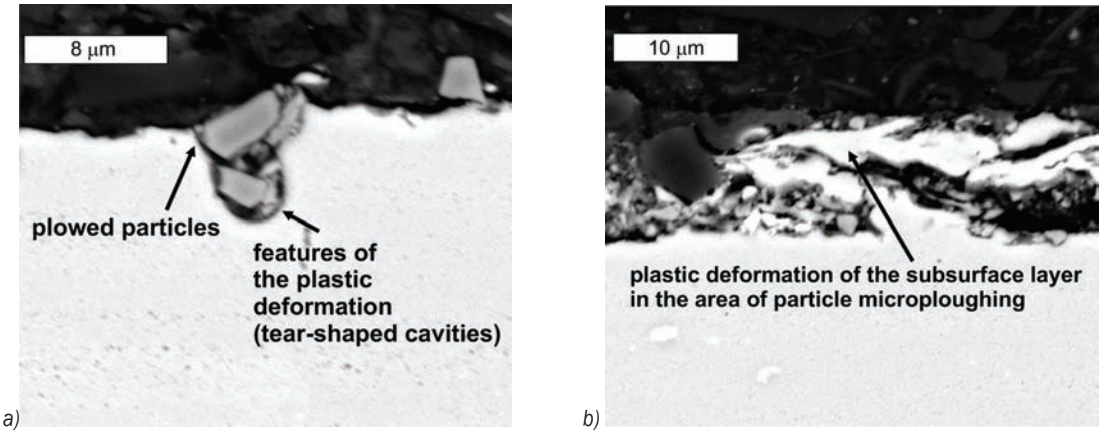

Fig. 19. *Subsurface wear morphology of the samples in the DA state; parallel to the sliding direction, SEM, etched with 10 % HF*

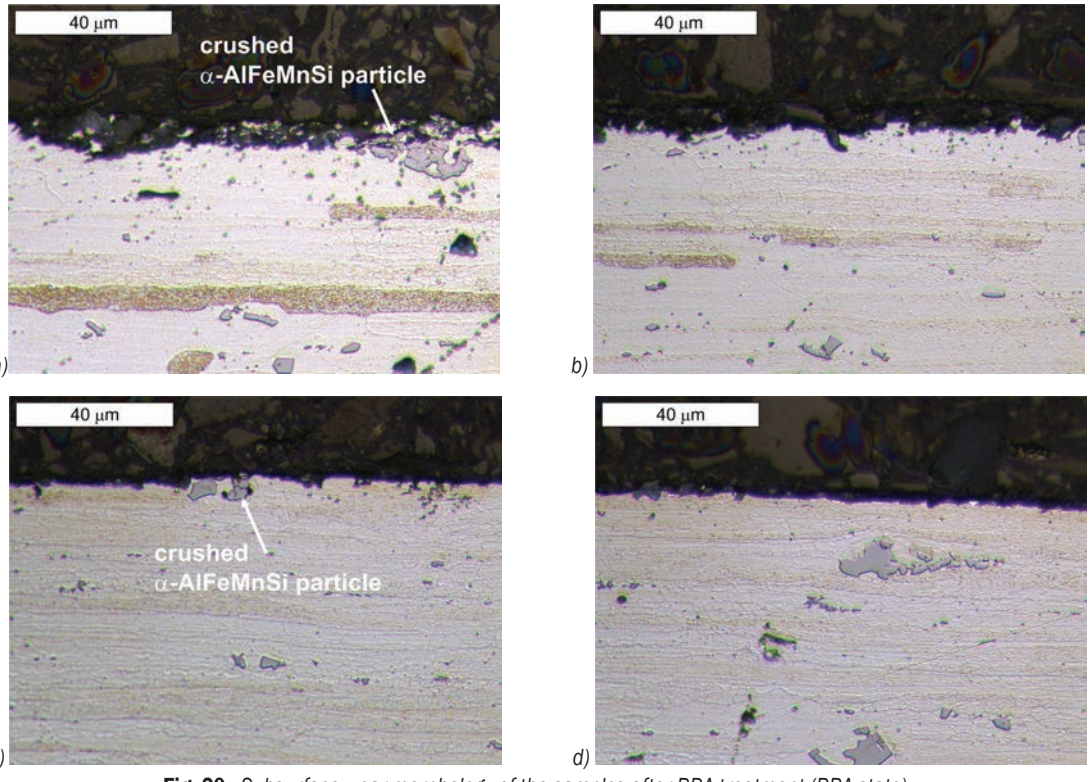

Fig. 20. *Subsurface wear morphology of the samples after RRA treatment (RRA state);*
a) and b) perpendicular, and c) and d) parallel to the sliding direction; light microscopy, etched with 10 % HF

its defragmentation and crushing. This also promotes its penetration into the friction area (Figs. 16 and c, 17 18, and 20).

The microhardness measurements are consistent with the macrohardness measurements. The microhardness can be ranked in the following increasing order: DA <T6 <RRA. Two effects can be expected as a result of the friction: an increase in hardness in the near-surface area, which would indicate the occurrence of hardening caused by plastic deformation; and the fact that increasing the temperature during friction may result in a partial disappearance and growth of the precipitation strengthening phases. The performed studies indicate that none of these effects occurred. The hardness fluctuated due to the microstructural heterogeneity. However, no tendency to increase or decrease the hardness directly at the surface was observed. The results are shown in Fig. 21 The dashed lines are

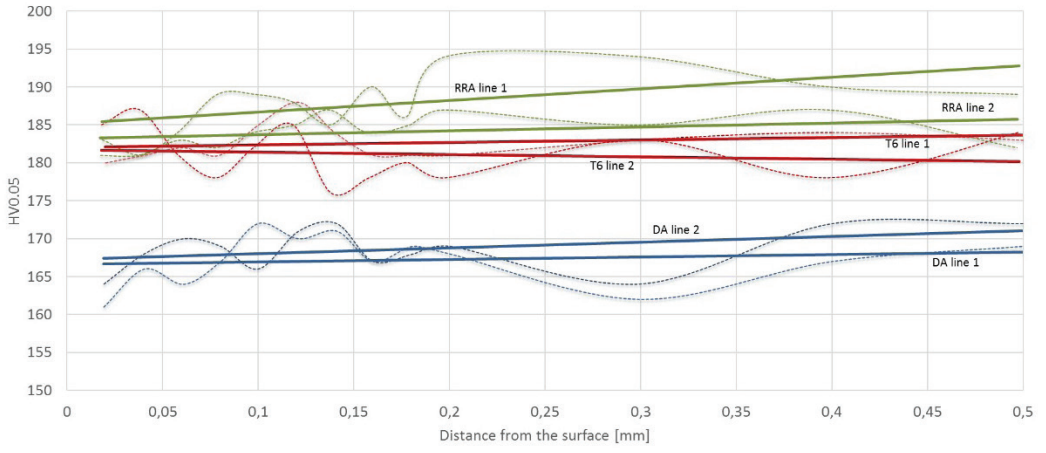

Fig. 21. *Hardness distribution curves as a function of distance from the surface*

responsible for the actual hardness distributions, while the solid line is an approximation.

3 CONCLUSIONS

The results of the hardness measurement and microscopic examinations, and the underlying reasons for the observed behaviour, can be summarized as follows:

1 The hardness of the AW7075 alloy is not the only determinant of abrasive wear. The conducted research shows that the microstructure of the tested alloy and the related heat treatment state also play an important role in this respect. The factor that favours the high value of the K_b coefficient is its high hardness, which is caused by the presence of phases that are coherent with the matrix. This parameter increases in the following order: DA <RRA <T6

2. The analyses of the wear paths showed the same type of damage in all the tested alloy states. The scratches, grooves, microcracks, and slight features of plastic deformation can be observed on the wear surface. The main wear mechanisms are therefore controlled by wedge formation and micro-ploughing. The delamination tendency may also have contributed to the increased wear of the DA condition, as delamination was observed in this condition. This is most likely related to the fact that this state has the lowest hardness.

3 The incoherent precipitation can increase hardness, as well as the wear rate, by disturbing the plastic flow during particle impact. Larger particles can also act as an abrasive and increase the wear rate during abrasion. Observations on the perpendicular cross-section of the samples showed that decohesion developed mainly around the grain boundaries and interfacial boundaries. The loss of continuity with the matrix is much easier in their case than in the presence of coherent particles.

4 The presence of large precipitates of the primary phases, which do not dissolve at the stage of heat treatment, favours their crushing and defragmentation during abrasive wear. This promotes their penetration into the friction area.

5 No tendency of an increase or decrease of the hardness directly at the surface was observed. An increase in hardness in the near-surface area could be expected, which would indicate the occurrence of hardening due to plastic deformation. However, an increase in temperature during wear could cause a partial disappearance and growth of the precipitation strengthening phases, which would result in a decrease in surface hardness. The studies performed indicate that none of these effects occurred.

4 REFERENCES

[1] Leśniewski, T. (2013). The influence of hardness of the steel sliding surfaces on their tribological characteristics. *5th World Tribology Congress*, p. 1-4.

[2] Lachowicz, M.M., Leśniewski, T., Lachowicz, M.B., Jasionowski, R. (2020). Tribological wear of as cast Zn-4Al alloy cooled at various rates from the eutectoid transformation temperature. *Archives of Foundry Engineering*, vol. 20, no. 4, p. 108-114, **DOI:10.24425/afe.2020.133356**.

[3] Krawczyk, J. (2010). Influence of the microstructure and loads on tribological properties of G155CrNiMo4-3-3 cast steel. *Archives of Foundry Engineering*, vol. 10, no. 3, p. 39-44.

[4] Yang, W., Ji, S., Wang, M., Li, Z. (2014). Precipitation behaviour of Al-Zn-Mg-Cu alloy and diffraction analysis from η′

precipitates in four variants. *Journal of Alloys and Compounds*, vol. 610, p. 623-629, **DOI:10.1016/j.jallcom.2014.05.061**.

[5] Berg, L.K., Gjønnes, J, Hansen, V, Li, X.Z, Knutson-Wedel, M., Waterloo, G., Schryvers, D., Wallenberg, L.R. (2001). GP-zones in Al-Zn-Mg alloys and their role in artificial aging. *Acta Materialia*, vol. 49, no 17, p. 3443-3451, **DOI:10.1016/S1359-6454(01)00251-8**.

[6] Peng, G., Chen, K., Chen, S., Fang, H. (2011). Influence of repetitious-RRA treatment on the strength and SCC resistance of Al-Zn-Mg-Cu alloy. *Materials Science and Engineering: A*, vol. 528, no. 12, 2011, p. 4014-4018, **DOI:10.1016/j.msea.2011.01.088**.

[7] Guo, F., Duan, S., Wu, D., Matsuda, K., Wang, T., Zou, Y. (2020). Effect of retrogression re-aging treatment on corrosion behavior of 7055 Al-Zn-Mg alloy. *Materials Research Express*, vol. 7, no 10, art. ID 106523, **DOI:10.1088/2053-1591/abc191**.

[8] Ashby, M.F., Jones, D.R.H. (2013). *Engineering Materials 2 - An Introduction to Microstructure and Processing*. Elsevier, Oxford.

[9] Ozer, G., Karaaslan, A. (2017). Properties of AA7075 aluminum alloy in aging and retrogression and reaging process. *Transactions of Nonferrous Metals Society of China*, vol. 27, no. 11, p. 2357-2362, **DOI:10.1016/S1003-6326(17)60261-9**.

[10] Park, J.K., Ardell, A.J. (1984). Effect of retrogression and reaging treatments on the microstructure of Ai-7075-T651. *Metallurgical and Materials Transactions A*, vol. 15, p. 1531-1543, **DOI:10.1007/BF02657792**.

[11] Marlaud, T., Deschamps, A., Bley, F., Lefebvre, W., Baroux, B. (2010). Evolution of precipitate microstructures during the retrogression and re-ageing heat treatment of an Al-Zn-Mg-Cu alloy. *Acta Materialia*, vol. 58, no. 14, p. 4814-4826, **DOI:10.1016/j.actamat.2010.05.017**.

[12] Wang, Y.L., Jiang, H.C., Li, Z.M., Yan, D.S., Zhang, D., Rong, L.J. (2018). Two-stage double peaks ageing and its effect on stress corrosion cracking susceptibility of Al-Zn-Mg alloy. *Journal of Materials Science & Technology*, vol. 34, no. 7, p. 1250-1257, **DOI:10.1016/j.jmst.2017.05.008**.

[13] Emani, S.V., Benedyk, J., Nash, P., Chen, D. (2009). Double aging and thermomechanical heat treatment of AA7075 aluminum alloy extrusions. *Journal of Materials Science*, vol. 44, p. 6384-6391, **DOI:10.1007/s10853-009-3879-8**.

[14] Umamaheshwer Rao, A.C., Vasu, V., Govindaraju, M., Sai Srinadh, K.V. (2016). Stress corrosion cracking behaviour of 7xxx aluminum alloys: A literature review. *Transactions of Nonferrous Metals Society of China*, vol. 26, no. 6, p. 1447-1471, **DOI:10.1016/S1003-6326(16)64220-6**.

[15] Krishnanunni, S., Gupta, R.K., Ajithkumar, G., Anil Kumar, V., Ghosh, R. (2020). Investigation on effect of optimized RRA in strength and SCC resistance for aluminium alloy AA7010. *Materials Today: Proceedings*, vol. 27, p. 2385-2389, **DOI:10.1016/j.matpr.2019.09.136**.

[16] Ładak, A., Cichoń, M., Lachowicz, M.M. (2022). Evaluation of the effect of dual-stage aging and RRA on the hardening and corrosion resistance of AW7075 Alloy. *Corrosion and Materials Degradation*, vol. 3, no. 1, p. 142-159, **DOI:10.3390/cmd3010008**.

[17] Li, Y., Xu, G., Liu, S., Peng, X., Yin, Z., Wang, L., Liang, X. (2019). Effect of ageing treatment on fatigue crack growth of die forged Al-5.87Zn-2.07Mg-2.42Cu alloy. *Engineering Fracture Mechanics*, vol. 215, p. 251-260, **DOI:10.1016/j.engfracmech.2019.04.023**.

[18] Nandana, M.S., Udaya Bhat, K., Manjunatha, C.M. (2019). Influence of retrogression and re-ageing heat treatment on the fatigue crack growth behavior of 7010 aluminum alloy. *Procedia Structural Integrity*, vol. 14, p. 314-321, **DOI:10.1016/j.prostr.2019.05.039**.

[19] Wang, Y., Liu, M., Xiao, W., Zhao, W., Ma, C. (2020). Effects of multi-stage aging treatments on the precipitation behavior and properties of 7136 aluminum alloy. *Journal of Alloys and Compounds*, vol. 814, art. ID 152256, **DOI:10.1016/j.jallcom.2019.152256**.

[20] Li, Z., Yu, H., Sun, D. (2021). The tribocorrosion mechanism of aluminum alloy 7075-T6 in the deep ocean. *Corrosion Science*, vol. 183, art. ID 109306, **DOI:10.1016/j.corsci.2021.109306**.

[21] GOST 23.208-79: Ensuring of wear resistance of products. Wear resistance testing of materials by friction against loosely fixed abrasive particles. Euro-Asian Council for Standardization, Metrology and Certification.

[22] Gore, G.J., Gates, J.D. (1997). Effect of hardness on three very different forms of wear. *Wear*, vol. 203-204, p. 544-563, **DOI:10.1016/S0043-1648(96)07414-5**.

[23] Mezlini, S., Kapsa, Ph., Henon, C., Guillemenet, J. (2004). Abrasion of aluminium alloy: effect of subsurface hardness and scratch interaction simulation. *Wear*, vol. 257, no. 9-10, p. 892-900, **DOI:10.1016/j.wear.2004.05.004**.

[24] Elleuch, K., Mezlini, S., Guermazi, N., Kapsa, Ph. (2006). Abrasive wear of aluminium alloys rubbed against sand. *Wear*, vol. 261, no. 11-12, p. 1316-1321, **DOI:10.1016/j.wear.2006.03.016**.

[25] Suleiman, I.Y., Kasim, A., Mohammed, A.T., Sirajo, M.Z. (2021). Evaluation of mechanical, microstructures and wear behaviours of aluminium alloy reinforced with mussel shell powder for automobile applications. *Strojniški vestnik - Journal of Mechanical Engineering*, vol. 67, no. 1-2, p. 27-35, **DOI:10.5545/sv-jme.2020.6953**.

[26] Udoye, N.E. Fayomi, O.S.I., Inegbenebor, A.O. (2019). Assessment of wear resistance of aluminium alloy in manufacturing industry - A review. *Procedia Manufacturing*, vol. 35, p. 1383-1386, **DOI:10.1016/j.promfg.2019.09.00721**.

[27] Chotěborský, R., Hrabě, P., Müller, M., Savková, J., Jirka, M., Navrátilová, M. (2009): Effect of abrasive particle size on abrasive wear of hardfacing alloys. *Research in Agricultural Engineering*, vol. 55, p. 101-113, **DOI:10.17221/24/2008-RAE**.

[28] Ku, A.Y., Khan, A.S., Gnäupel-Herold, T. (2020). Quasi-static and dynamic response, and texture evolution of two overaged Al 7056 alloy plates in T761 and T721 tempers: Experiments and modeling. *International Journal of Plasticity*, vol. 130, art. ID 102679, **DOI:10.1016/j.ijplas.2020.102679**.

[29] Chen, J., Zhen, L., Yang, S., Shao, W., Dai, S. (2009). Investigation of precipitation behavior and related hardening in AA 7055 aluminum alloy. *Materials Science and Engineering: A*, vol. 500, no. 1-2, p. 34-42, **DOI:10.1016/j.msea.2008.09.065**.

Strojniški vestnik - Journal of Mechanical Engineering 68(2022)7-8, 506-513
DOI:10.5545/sv-jme.2022.30
Original Scientific Paper
Received for review: 2022-01-26
Received revised form: 2022-07-08
Accepted for publication: 2022-07-11

Nitriding HS6-5-2 Steel in Inductively Coupled Plasma

Marek Binienda[1] – Robert Pietrasik[2,*] – Sylwester Pawęta[2] – Krzysztof Matczak[1] – Witold Krotewicz[1]
[1] Zemat Technology Group, Poland
[2] Lodz University of Technology, Institute of Materials Science and Engineering, Poland

This article presents research on the possibility of obtaining a hardened surface layer via nitriding in coupled plasma (ICP) for HS6-5-2 steel. The subject of the investigation was the influence of the process parameters on the properties of the obtained layers. The surface layers were characterized using an optical microscope, SEM (Scanning Electron Microscope), EDS (Energy Dispersive Spectroscopy), XRD (X-Ray Diffraction), and a microhardness tester. The generator power was changed gradually from 500 W to 2 kW and the tests were carried out for various process durations, from 15 to 45 minutes at a set pressure. The obtained results show the possibility of obtaining nitrided surface layers with a thickness of up to 0.1 mm and a significant increase in hardness in a very short time.
Keywords: plasma, nitriding, surface layer, hardness

Highlights
- *The maximum hardness of about 1100 HV was obtained: an increase in hardness by 350 % in relation to the starting material.*
- *Nitrided layers with a thickness of 100 µm were obtained following a very short process: 45 minutes.*
- *The influence of process parameters on the properties of the nitrided layers is shown.*
- *The nucleation and growth mechanism of the nitrided layers obtained by this method is described.*

0 INTRODUCTION

The constant development of technology means that there is a need to optimize the functional properties of materials used in the production of tools and machine parts. On one hand, this process can be achieved by producing tool materials with better properties, which requires the use of expensive alloying additives in a multi-stage technological process **[1]** and **[2]**. On the other hand, research to modify the surface layer to obtain new, more favourable functional features of ready-made tools is being carried out. Despite significant progress in the development of surface engineering, methods for increasing the durability and reliability of tools and structural elements, especially those of small dimensions, still cause problems **[3]** and **[4]**. One of the most frequently used technologies, especially for small dimension elements, is nitriding **[5]** to **[7]**. Nitriding done by the classical thermo-chemical treatment method leads to ε ($Fe_{2-3}N$) and γ' (Fe_4N) **[8]** to **[10]** brittle layer formation. In the case of gaseous-controlled processes, it is possible to control the phase composition of the layers, but the processes take a relatively long time, even for thin layers **[11]**. Plasma-assisted nitriding is presented in the literature on the subject primarily concerning ionic discharge, which is the phenomenon of accelerating particles in an electric field. The high kinetic energy of ions is created as a result of the potential difference between the electrodes, both in the glow discharge of direct current and in the high-frequency electric field. In the first case, the existence of strong field strength is obvious and directly dependent on the potential difference applied to the electrodes. In high-frequency plasma discharge, the discharge is obtained between opposite electrodes as a result of applying a high-energy and high-frequency signal from a generator to them. Such plasma is called "capacitively coupled plasma" (CCP). The generator can be connected by means of electrodes directly to the discharge area or by galvanic isolation of one of the electrodes using a capacitor or an insulator.

The disadvantage of the direct variant of connecting the linings with the discharge is the possibility of contamination of the treatment atmosphere with matter from the electrodes due to their contact with the plasma. In the case of isolating one of the electrodes, due to the different masses and the related mobility of ions and electrons, the high frequency of electrode polarization changes means that heavy ions cannot keep up with the changes in the electric field. As a result, a constant, non-discharged charge accumulates on one of the electrodes, causing the electrode to be polarized with a constant voltage. This phenomenon is called "autopolarization", and its consequence is the creation of a strong, directed electric field, which accelerates the ions, by giving them high kinetic energy, causing the spraying of the processed samples. This is the main reason that this method of plasma production cannot be used to nitride objects while keeping their surface and edges intact.

*Corr. Author's Address: Lodz University of Technology, Institute of Materials Science and Engineering, 1/15 Stefanowski Street,90-924 Lodz, Poland, robert.pietrasik@p.lodz.pl

Another disadvantageous effect of the directed electric field is the shadow phenomenon, which makes it necessary to change the position of the workpieces during the process [12]. It should be emphasized, however, that CCP plasma is used in numerous industrial applications in which high ion energy is useful, e.g., ion etching, surface cleaning, or expanding.

The use of inductively coupled plasma obtained in a strong magnetic field due to the flow of Foucault currents eliminates the occurrence of an accelerating electric field. The magnetic field of the solenoid causes the flow of eddy currents both in the gas region and in the workpiece, which simultaneously fulfil two tasks: they resistively heat both the gas (nitrogen) creating a plasma ring discharge and the workpieces to the penetration depth, where the value depends on the resistivity of both the ionized gas and the sample and frequency. Multiple ionization of particles in a low-temperature non-isothermal plasma [13] makes it an effective source of the nitriding agent and can be used for diffusive saturation of metals. However, the use of such an induced plasma for steel nitriding is practically unknown, as single works on a laboratory scale [14] have only been recognized. In contrast, inductively coupled plasma is widely used for the physical deposition of various types of coatings [15].

A proprietary stand for nitriding in high-frequency plasma was designed and built to perform the tests (Fig. 1). The device consists of a high-frequency generator set with an inductor, which contains a reactor inside. The set of vacuum pumps allows the appropriate vacuum to be obtained. Nitrogen with a purity of 99.9 % is taken from a cylinder via the mass flow controller.

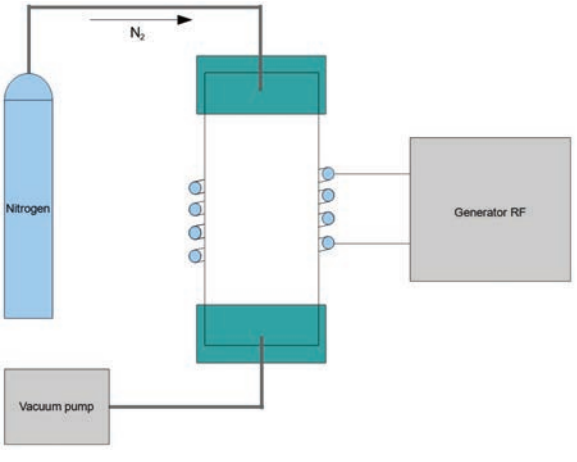

Fig. 1. *Block diagram of the device for Inductively Coupled Plasma*

As part of this work, the HS6-5-2 steel was subjected to tests. Cutting tools made of this steel, including the drills, taps, and reamers most commonly used in industry and households, constitute a specific group: they are exposed to work in very difficult conditions. Practice shows that small-size tools are not sharpened but replaced with new ones [16]. Therefore, the modification of the surface by nitriding in inductively coupled plasma, leading to a numerous increase in their durability while maintaining high core impact strength, is economically justified.

1 EXPERIMENTAL PROCEDURE

The samples used for the tests were HS6-5-2 steel bars with a diameter of 4 mm, a length of 60 mm with the composition in accordance with the standard shown in Table 1. The samples were in the raw steel state (without heat treatment).

Table 1. *Standardized chemical composition [wt. %] of HS6-5-2 steel*

C	Cr	Mo
0.80 to 0.88	3.80 to 4.50	4.70 to 5.20
V	W	Si
1.70 to 2.10	5.90 to 6.70	Max 0.45

The samples were nitrided in a stand built for nitriding in inductively coupled plasma discharge with a frequency from a band intended for industrial, scientific, and medical (ISM) applications, in a continuous operation mode. The device was made of a reactor in the form of a quartz tube, 70 mm long and 100 mm in diameter, and was connected to a set of vacuum pumps, which included a turbomolecular pump and a scroll pump. The operating pressure of the process under a nitrogen atmosphere of 99.9 % purity was 100 Pa, and its flow was controlled by a mass flow controller (MFC). The plasma discharge took place within a coil made of a copper pipe with a diameter of 8 mm and was powered by a generator with a frequency of 27.12 MHz. The power was changed in steps ranging between 600 W, 1 kW, 1.5 kW, and 2 kW. The samples placed in quartz glass process tables were nitrided at constant pressure and changed the duration of the process (15 min, 60 min, 240 min) for the set generator power.

The cross-section microstructures of specimens were observed using a Nikon MA200 optical microscope (Nikon Instech Co., Ltd., Tokyo Japan). The microstructure and chemical composition of the surface layers were also investigated by using a

scanning electron microscope (SEM) JEOL JSM-6610 LV (JEOL Ltd., Tokyo Japan) equipped with an energy dispersion spectroscope (EDS) X-MAX 80 Oxford Instruments (Oxford Instruments Group, Abingdon, United Kingdom). The X-ray diffraction (XRD) was done on a device from PANalytical Empyrean (Malvern Panalytical Ltd, Malvern, United Kingdom). The source was an x-ray tube with cobalt anode-emitting characteristic radiation (CoKα = 1.74 Å). Primary beam optic consisted of Goebel mirror for Co radiation, fixed divergence slit 0.5 deg, Soller slit 0.04 rad, and mask 10 mm. Diffracted beam optic consisted of parallel plate collimator 0.18 deg, Soller slits 0.04 rad and proportional Xe detector. The hardness distribution of the nitrided layers was measured using a Vickers microhardness tester NEXUS 4505 (INNOVATEST Ltd., Maastricht, Netherlands). The surface hardness on the sample prepared for metallographic tests was measured at a distance of 10 µm from the edge of the sample and successively further inside the sample every 5 µm. Measurements were made with 0.98 N load. The surface roughness profile parameters were tested with the T8000 RC profilometer by Hommel-Etamic. Parameter *Ra* arithmetic mean of the profile ordinates, was determined in accordance with the PN-EN ISO 4287 standard.

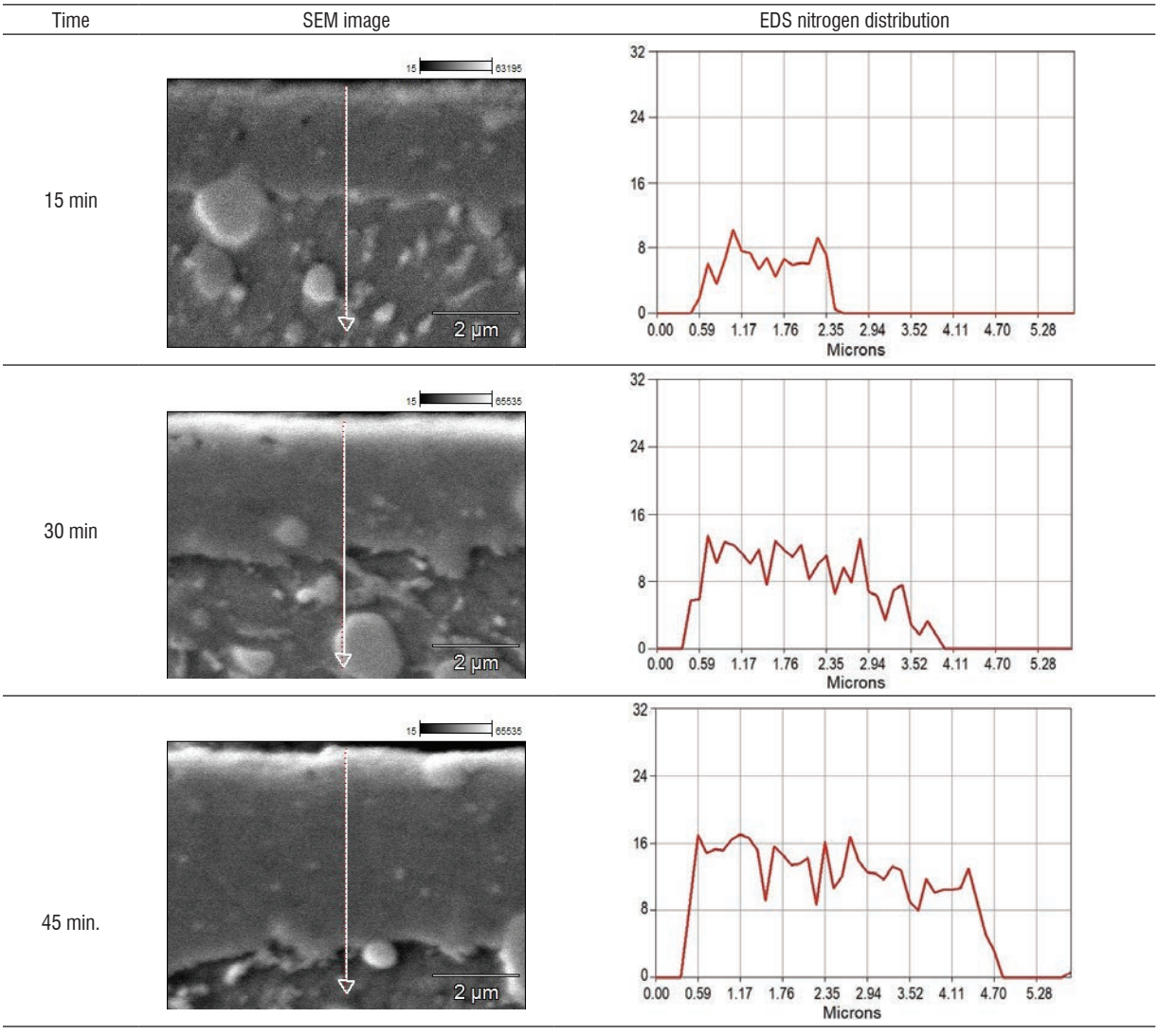

Fig. 2. *Images of the SEM structures and the corresponding EDS nitrogen distributions obtained at a generator power of 500 W for different process times.*

2 RESULTS AND DISCUSSION

As a result of the processes carried out at a generator power of 500 W, zones of nitride compounds on the surface were only obtained without an internal nitriding zone, regardless of time. Images of the SEM structures and the corresponding EDS nitrogen distribution distributions are shown in Fig. 2.

With a generator power of 500 W (Fig. 2), only the rudiments of the layer can be observed in the form of a white zone of nitride compounds: initially composed of γ' nitrides, and after longer dosing of nitrogen, transforming into ε nitrides. In this case, the internal nitriding zone was not obtained probably because of the low temperature of the samples, which was not sufficient to dissolve the nitrides and diffuse nitrogen into the samples. In the case of the shortest time (15 min), the nitrogen content in the nitride zone was about 6 % by weight, which proves that it is mainly γ' nitride (Fe_4N). If the process is prolonged to 30 min, the nitrogen content increases, on average, to a level of about 10 % by weight. This value and the fact that the content exceeds 8 % prove that we are dealing with ε nitride ($Fe_{2-3}N$). Analogically, for a time of 45 min, the average nitrogen content is about 12 % by weight, so we are dealing with slightly more saturated nitrogen, specifically the nitride ε ($Fe_{2-3}N$).

These observations are consistent with the X-ray diffraction test (Fig. 3), where the spectra for the samples after 15 min and 45 min nitriding processes are presented. In the first case, the γ' (Fe_4N) nitrides are visible only. In the case of the longer process (45

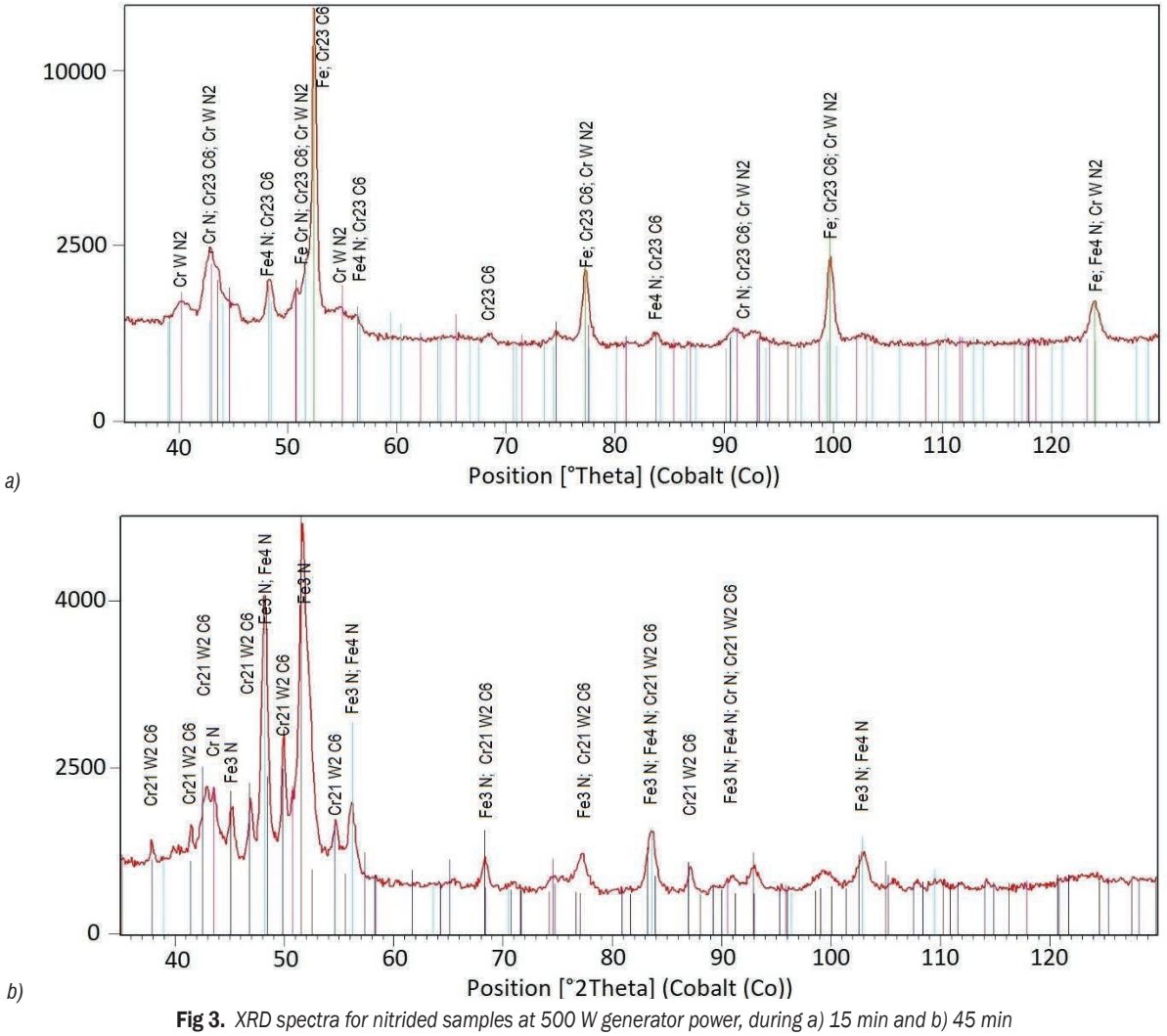

Fig 3. *XRD spectra for nitrided samples at 500 W generator power, during a) 15 min and b) 45 min*

min), the stress of nitrides ε (Fe_3N) and residuals of γ' (Fe_4N) are visible, respectively.

This may prove that the process of constituting nitrided layers takes place through the nucleation of γ' nitrides, which (together with a longer nitrogen supply) transform into ε nitride. However, with the indicated generator power, the obtained substrate temperature is too low and does not allow nitrogen diffusion deeper into the samples, as evidenced by the absence of an internal nitriding zone, and is confirmed by the lack of increase in the hardness of the sample directly under the nitride layer (the hardness at a depth of 10 µm is about 980 HV). In contrast, surface hardness ranges from 960 HV, in the case of γ' nitride on the surface, to 700 HV for ε.

The processes carried out using higher generator powers allowed diffusion layers of various uniformity and thickness, as well as structural formation, to be obtained. The summary of the obtained structures is shown in Fig. 4.

The analysis of the photos shows that there is a clear correlation between the parameters of the process and the thickness and structure of the obtained layers. Increasing the generator power to 1 kW results in the appearance of the beginnings of the diffusion zone with a very irregular depth. A longer process time results in an increase in nitrogen saturation, but the layers are highly heterogeneous. At 1.5 kW, the diffusion layer is clearly visible but is not uniform and has an island structure, especially for shorter process times. It is clearly visible at shorter process times (e.g., for 15 min, the depth of the diffusion zone ranges from 26 µm to 42 µm, but a white zone of nitride compounds appears on the surface above the areas of the thicker zone of internal nitriding). Increasing the time to 45 min makes the thickness uniform; however, the nitride compounds were not diffused. The use of a 2 kW generator results in even layers with a constant thickness after a 15 min process. However, an undiffused zone of nitride compounds is visible. Only

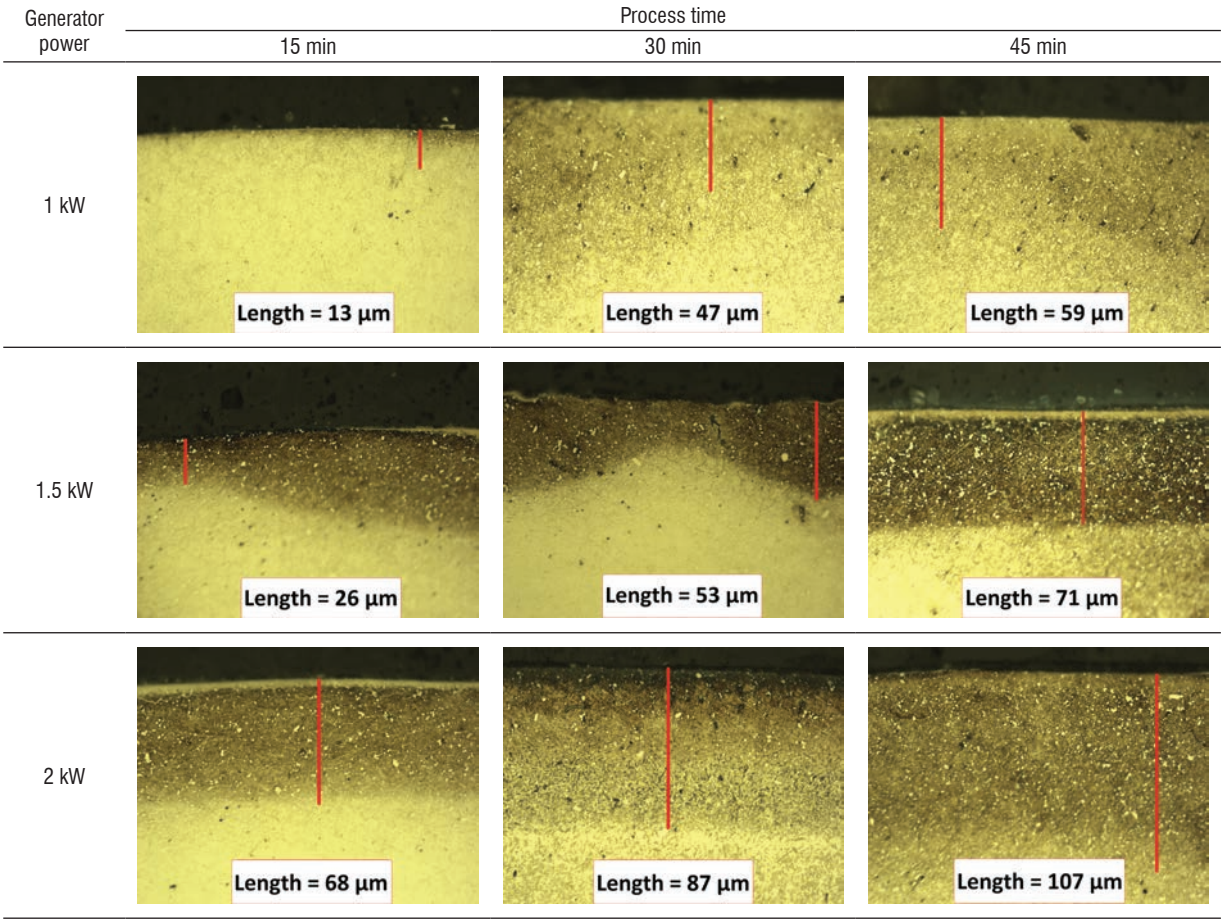

Fig. 4. *Summary of metallographic structures obtained for different generator powers and process times*

extending the duration of the process clearly results in increasing the depth of nitrogen diffusion into the steel structure and in obtaining layers with only the internal nitriding zone, without a zone of nitride compounds on the surface (white zone).

The results of XRD studies are the confirmation of the above-described phenomenon and the model of nucleation and growth of nitrided layers in inductively coupled plasma. Fig. 5 shows XRD spectrum, which was made for sample processed in the parameters considered optimal: 2 kW generator power, for 45 min. It shows reflections from the Fe phase: ferrite, and nitrides, Fe_4N and CrN. Of course, there are also visible carbide phases, e.g., of the Fe_3W_3C type, which are typical for this type of steel. The reflex at 52 deg is slightly shifted to the left (compressive stresses) and slightly widened, which indicates the existence of a solid nitrogen solution gradient in Fe and, therefore, the presence of the diffusion zone in the structure.

Fig. 6 presents a list of optical images of the surface appearance of the initial samples, after the process in which the nitride compounds zone was obtained (P = 500 W, t = 45 min.), and after the diffusion of the nitride compounds zone (P = 2 kW, t = 45 min.). For the initial samples, the surface roughness parameter Ra was 0.08 µm. In the case of nitrided samples with a zone of nitride compounds, the sample changes to dull grey (Fig. 6b), which is related to the presence of ε nitride on the surface and is consistent with the Ra = 0.87 µm roughness measurement results. However, in the case of surfaces from which the nitride layers have been diffused and in the structure, we only observe a diffusion zone, the colour changes to a darker one, and the appearance is less dull (Fig. 6c). The reduction of roughness after the diffusion of the nitrides is also visible in the results of measurements of the Ra = 0.69 µm parameter.

Fig. 6. *Summary of the surface appearance of samples in different technological conditions; a) the surface appearance of the initial sample before the nitriding process, b) the appearance of the sample surface after nitriding with the zone of nitride compounds, and c) the appearance of the sample surface after nitriding and after the zone of nitride compounds diffused*

To determine the effective thickness of the obtained surface layers, hardness distributions were made as a function of the distance from the edge of the sample. Due to the unevenness of the layers, especially for lower generator power, five hardness distributions were made. The average results, compiled separately for each of the generator powers for the tested process time lengths, are shown in Figs. 7 to 9. It should be emphasized that high hardness values were obtained despite the core not being hardened.

The maximum hardness of the samples exceeds 1000 HV, with an initial (core) hardness of about 600 HV, which translates into a 60 % increase in hardness. There is also a general tendency of increasing maximum hardness with increasing generator power and process time.

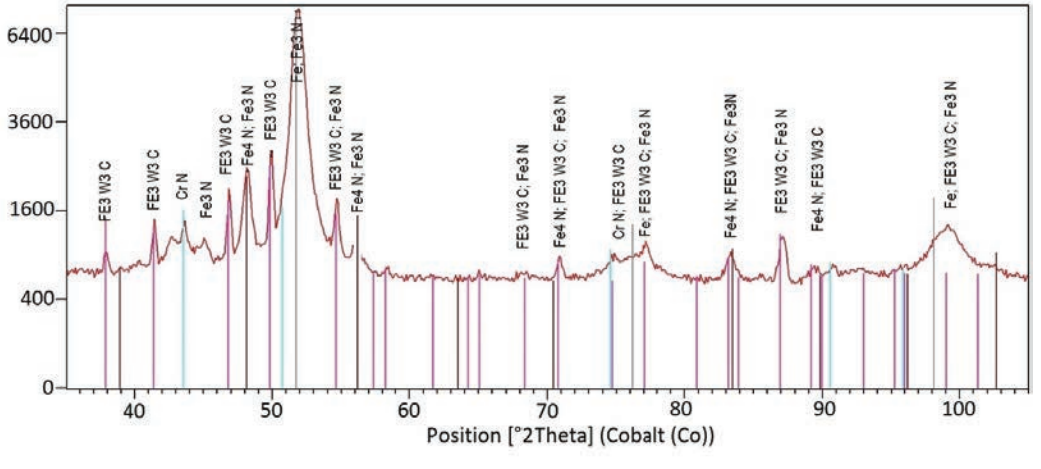

Fig 5. *XRD spectrum for nitrided sample at 2 kW generator power, 45 min*

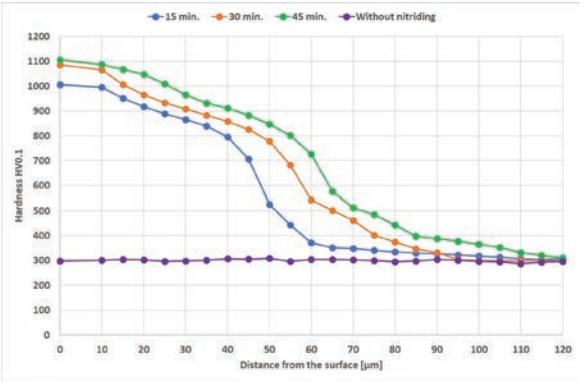

Fig. 7. *Comparison of microhardness distribution of surface layers obtained with a 1 kW generator power for different process times*

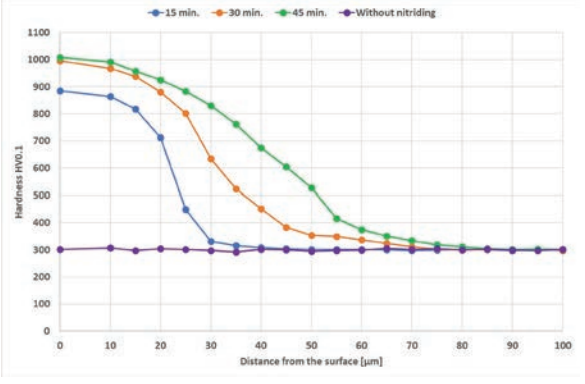

Fig. 8. *Comparison of microhardness distribution of surface layers obtained with a 1.5 kW generator power for different process times*

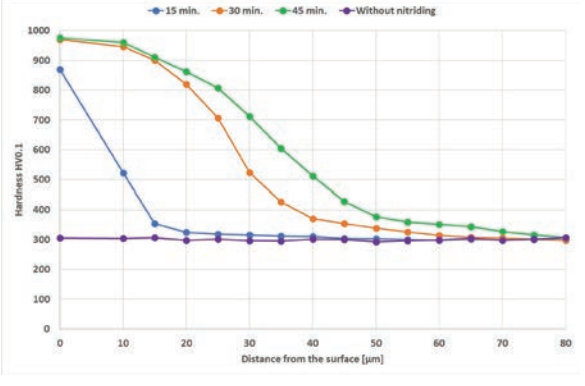

Fig. 9. *Comparison of microhardness distribution of surface layers obtained with a 2 kW generator power, for different process times*

Based on the hardness distributions made for a power of 1 kW, 1.5 kW, and 2 kW, the effective thicknesses of individual layers were determined in accordance with DIN 50190-3 (criterion 50 HV above the core hardness), while for the generator power of 500 W, the layer thickness was determined metallographically. Table 2 shows the thickness of the obtained layers as a function of generator power and process duration.

When analysing the obtained layer thicknesses, it can be observed that, in line with theoretical predictions, the layer thicknesses increase along with generator power and with the extension of the process time. However, due to the thickness of the layers, their uniformity and phase structure, only the layers obtained with a generator power of 2 kW and process times of 30 min and 45 min are of practical importance for the application. In these cases, uniform layers were obtained without the white zone and the precipitation of nitrides at the grain boundaries of the former austenite, thus the most desirable for potential applications for small cutting tools.

It should be emphasized that the layers of usable thickness are obtained after a very short process (45 min). If counting a complete pump-down cycle, this time is approximately 1.5 hours. Compared to gas nitriding methods, for which the full cycle of such thickness is about 9 hours, this is a very good result. Comparison of the ionic or plasma methods with other methods of induction provides the following conclusions: the time is similar, but the inductively coupled plasma allows to eliminate the edge dissolution phenomenon and avoid the shadow effect.

Table 2. *Summary of the thicknesses of the obtained layers as a function of generator power and process duration*

Generator power	Process time		
	15 min	30 min	45 min
500 W	2.4 μm	4.0 μm	4.7 μm
1 kW	13 μm	47 μm	59 μm
1.5 kW	26 μm	53 μm	65 μm
2 kW	68 μm	87 μm	107 μm

3 CONCLUSIONS

1. It is possible to obtain nitrided layers with the correct structure in inductively coupled plasma. It is very important from a technological and economic point of view, i.e., a significant reduction of the process time with the possibility of full regulation of the structure of the layers, also without the zone of nitride compounds.
2. The possibility of nitriding in inductively coupled plasma on an industrial scale is also very important from an ecological point of view. The process uses inert nitrogen instead of toxic ammonia. In the new technology, there are also no emissions that require the utilization of post-process gases.

3 For samples made of HS6-5-2 steel with a diameter of 4 mm, it is best to conduct the process with a generator power of 2 kW.
4 The maximum hardness obtained on the raw material is about 1000 HV; hardness increases by 50 % in relation to the starting material.
5 Layers with functional properties of 100 µm thickness are obtained in a very short process lasting 45 min.

4 ACKNOWLEDGMENTS

The work has been done under Measure 1.2 — Sectoral Research & Development programs of "Program Operacyjny Inteligentny Rozwój" 2014-2020 (Smart Growth Operational Program 2014-2020) co-funded by the European Regional Development Fund. The project: "Development of nitriding technology for machine parts and tools in inductively coupled plasma together with a device for its implementation." Contract Number: POIR.01.01.01-00-0087/17

5 REFERENCES

[1] Pye, D. (2003). *Practical Nitriding and Ferritic Nitrocarburizing*. ASM International, Russell Township, **DOI:10.31399/asm.tb.pnfn.9781627083508**.

[2] Bilger, P., Dulcy J., Gantois M., Torchane L. (1996). Control of iron nitride layers growth kinetics in the binary Fe-N system. *Metallurgical and Materials Transactions: A*, vol. 27A, p. 1823-1835, **DOI:10.1007/BF02651932**.

[3] Sawicki, J., Siedlaczek P., Staszczyk A. (2018). Fatigue life predicting for nitrided steel - finite element analysis. *Archives of Metallurgy and Materials*, vol. 63 no. 2, p. 921-927, **DOI:10.24425/122423**.

[4] Sawicki, J., Siedlaczek P., Staszczyk A. (2018). Finite-element analysis of residual stresses generated under nitriding process: a three-dimensional model. *Metal Science and Heat Treatment*, vol. 59, no. 11-12, p. 799-804, **DOI:10.1007/s11041-018-0229-y**.

[5] Pokorny, Z., Dobrocky, D., Kadlec, J., Studeny, Z. (2018). Influence of alloying elements on gas nitriding process of high-stressed machine parts of weapons. *Metallic Materials*, vol. 56, no. 2, p. 97-103, **DOI:10.4149/km_2018_2_97**.

[6] Totten, G., Colas, R. (2016). *Encyclopedia of Iron, Steel, and Their Alloys*. CRC Press, Boca Raton, **DOI:10.1081/E-EISA**.

[7] Gawroński, Z., Sawicki, J. (2006). Technological surface layer selection for small module pitches of gear wheels working under cyclic contact loads. *Materials Science Forum*, vol. 513, p. 69-74, **DOI:10.4028/www.scientific.net/MSF.513.69**.

[8] Nguyen, D.N., Nguyen, A.X., Nguyen, V.B., Le, T.N., Le, T.Ch. (2019). Control Gas Nitriding Process: A Review. *Journal of Mechanical Engineering Research and Developments*, vol. 42, no. 1, p. 17-25, **DOI:10.26480/jmerd.01.2019.17.25**.

[9] Maldzinski, L., Liliental, W., Tymowski, G., Tacikowski, J. (1999). New possibilities for controlling gas nitriding process by simulation of growth kinetics of nitride layers. *Surface Engineering*, vol. 15 no. 5, p. 377-384, **DOI:10.1179/026708499101516740**.

[10] Mittemeijer, E. J., Somers, M. A. J. (1997). Thermodynamics, kinetics, and process control of nitriding. *Surface Engineering*, vol. 13, no. 6, p. 483-497, **DOI:10.1179/sur.1997.13.6.483**.

[11] Aghajani, H., Behrangi, S. (2017). *Plasma Nitriding of Steels*. Springer International Publishing, Berlin, **DOI:10.1007/978-3-319-43068-3**.

[12] Chen, F. F. (2012) *Introduction to Plasma Physics*. Springer Science & Business Media, Berlin.

[13] Binienda, M. (2013). *Research on the Nitriding of the Small Diameter Drills in High-Frequency Ring Discharge Plasma.* Ph.D. thesis, University of Lodt, Lodz. (in Polish)

[14] Kim, H. S., Kim, J. H., Kim, W. Y., Lee, H. S., Kim, S. Y., Khil, M. S. (2017). Volume control of expanded graphite based on inductively coupled plasma and enhanced thermal conductivity of epoxy composite by formation of the filler network. *Carbon*, vol. 119, p. 40-46, **DOI:10.1016/j.carbon.2017.04.013**.

[15] Delzeit, L., McAninch, I., Cruden, B. A., Hash, D., Chen, B., Han, J., Meyyappan, M. (2002). Growth of multiwall carbon nanotubes in an inductively coupled plasma reactor. *Journal of Applied Physics*, vol. 91, no. 9, p. 6027-6033, **DOI:10.1063/1.1465101**.

[16] Global Industry Analysts. (2021). High Speed Steel (HSS) Metal Cutting Tools - A Global Market Report, from *https://strategyr.com*, accessed on 2021-04-30.

Vsebina

Strojniški vestnik - Journal of Mechanical Engineering
letnik 68, (2022), številka 7 8
Ljubljana, julij-avgust 2022
ISSN 0039-2480

Izhaja mesečno

Razširjeni povzetki (extended abstracts)

Strojniški vestnik - Journal of Mechanical Engineering 68(2022)7-8, SI 61

Prejeto v recenzijo: 2022-05-08
Prejeto popravljeno: 2022-06-22
Odobreno za objavo: 2022-08-05

Kratkotrajno lezenje različnih polimerov za dodajalno izdelavo v različnih temperaturnih in obremenitvenih razmerah

Oguz Dogan*
Univerza Kahramanmaras Sutcu Imam, Oddelek za strojništvo, Turčija

Polimerni materiali za dodajalno izdelavo so v pogojih stalnih obremenitev podvrženi signifikantnim spremembam dimenzij. To lahko vpliva na varnost delovanja polimernih konstrukcij, izdelanih po dodajalnih postopkih in zato obstaja potreba po opredelitvi lezenja polimerov, ki se uporabljajo pri dodajalni izdelavi.

Temperatura je eden glavnih parametrov, ki vplivajo na lezenje polimerov. V dostopni literaturi pa je le malo študij, ki bi obravnavale vpliv temperature na lezenje preizkušancev, izdelanih po postopku FDM. Pomanjkanje obstoječih raziskav je bilo tudi glavna motivacija za izvedbo pričujoče študije.

Lezenje preizkušancev, pripravljenih po postopku dodajalne izdelave (iz materialov PLA, ABS, TPLA, CPE, najlon, PC), je bilo eksperimentalno preizkušeno pri treh različnih temperaturah (25 °C, 40 °C in 60 °C) in dveh stopnjah obremenitve (10 MPa in 20 MPa). Preizkušanci so bili izdelani na 3D -tiskalniku Ultimaker 2+ Extended 3D printer in na CNC rezkalnem stroju, s čimer je bila zagotovljena homogena struktura. Eksperimenti so bili opravljeni na standardni napravi za preizkušanje lezenja. Merilnika na napravi merita temperaturo in raztezek preizkušanca. Preizkusi lezenja so bili opravljeni v skladu s standardom ASTM D2990 - 17 in so potekali v klimatizirani sobi na mizi, ki je izolirana proti vibracijam. Vsak preizkus lezenja je trajal 3 ure (10.800 s), v tem času pa je potekalo merjenje in beleženje raztezka zaradi lezenja z mikrometrom.

Hitrost lezenja je pri vseh materialih rasla s temperaturo okolice in ravnjo napetosti. Rezultati so pokazali, da ima obremenitev večji vpliv na lezenje kot temperatura. PC je bil v vseh eksperimentalnih scenarijih najbolj obstojen proti lezenju. Najslabšo obstojnost proti lezenju ima material PLA, ki se najpogosteje uporablja v 3D-tiskalnikih. Za dele, natisnjene iz materiala PLA na 3D-tiskalnikih, je zato priporočljiva uporaba pri sobni temperaturi ter v odsotnosti obremenitev oz. pod zelo majhnimi statičnimi obremenitvami.

Izdelava vsakega preizkušanca na 3D-tiskalniku in CNC-stroju traja približno 1,5 ure, preizkus lezenja pa nato traja še dodatne 3 ure. Pridobitev ene same krivulje lezenja torej traja v povprečju 4,5 ure. Izvedljivo število eksperimentov je zato omejeno in tudi ni bilo mogoče preiskati lezenja materialov, ki so manj razširjeni v dodajalni proizvodnji.

Poleg tega so nekateri materiali zelo elastični in zanje ni bilo mogoče določiti krivulj lezenja s to napravo (npr. TPU in PP).

Pregled literature je pokazal pomanjkanje študij lezenja raznih natisnjenih polimernih izdelkov pri različnih temperaturah in obremenitvah. Članek bo zato zanimiv za bralce, ki se ukvarjajo z dodajalno izdelavo, 3D-tiskalniki ali karakterizacijo polimerov.

Ključne besede: dodajalna izdelava, preizkusi lezenja, polimerni materiali, vpliv toplote

*Naslov avtorja za dopisovanje: Univerza Kahramanmaras Sutcu Imam, Oddelek za strojništvo, Turčija, oguzdogan@ksu.edu.tr

Strojniški vestnik - Journal of Mechanical Engineering 68(2022)7-8, SI 62

Prejeto v recenzijo: 2022-04-06
Prejeto popravljeno: 2022-06-13
Odobreno za objavo: 2022-06-16

Priprava in termična karakterizacija trdnih/kapljevitih organskih kompozitnih fazno spremenljivih snovi (PCM) na osnovi maščobnih kislin, izboljšanih z nanografenom, za shranjevanje toplote

Ragul Kumar Kittusamy* – Velavan Rajagopal – Paul Gregory Felix
Tehniški kolidž PSG, Oddelek za strojništvo, Indija

Glavni cilj pričujočega raziskovalnega dela je premostitev vrzeli med ponudbo in potrebami po energiji na področju gospodinjskih solarnih grelnikov vode (SGV). Shranjevanje toplote (ST) v SGV s pomočjo fazno spremenljivih snovi je do okolja prijazen pristop k pripravi dodatne vroče vode. Delovna temperatura gospodinjskih SGV je približno 65 °C. Konvencionalni PCM na osnovi parafina, ki se uporabljajo za ST v SGV, imajo tališče med 50 °C in 60 °C ter niso primerni za zagotavljanje vroče vode z najvišjo želeno temperaturo. V predstavljenem delu je bila uporabljena evtektična kombinacija PCM na osnovi maščobnih kislin s tališčem blizu 65 °C kot alternativa parafinskim PCM za pripravo vroče vode z najvišjo temperaturo.

Toplotna prevodnost najbolj razširjenih sodobnih PCM je razmeroma nizka (od 0,5 do 1 W/mK), kar lahko resno vpliva na celotno zmogljivost sistema za ST. Za naslavljanje omenjenega problema so bili predlagani fazno spremenljivi snovi dodani nanoaditivi na osnovi ogljika. Nanodelci grafena so bili dodani po postopku dvostopenjske mehanske disperzije v utežnih razmerjih 1, 2 in 3 %. Za pravilno uporabo pripravljenih kompozitov NPCM v kateri koli aplikaciji je potrebno osnovno poznavanje materialnih lastnosti, v objavljeni literaturi pa ni bilo mogoče najti raziskav termičnih lastnosti PCM na osnovi maščobnih kislin z različno vsebnostjo nanodelcev grafena.

Glavni cilj raziskovalnega dela je bila priprava in preučitev toplotnih lastnosti ter kemijske in toplotne stabilnosti novih kompozitov. Obstoj in enakomerna porazdelitev grafena v PCM sta bila potrjena z ramanskim spektrometrom in analizo z vrstičnim elektronskim mikroskopom. Rezultati FTIR in XRD so pokazali, da so vsi trije kompoziti NPCM kemijsko stabilni, njihova kristaliničnost pa je podobna kot pri osnovnem PCM. Pri vzorcu s 3 % grafena se je toplotna prevodnost v trdnem stanju povečala za 219,89 %, toplotna prevodnost v kapljevitem stanju pa za 161,65 %. Analiza DSC je razkrila tudi 3,52-odstotno zmanjšanje specifične latentne toplote. Vsi kompoziti NPCM imajo začetno in vršno temperaturo tališča blizu osnovnega PCM. Rezultati TGS so pokazali, da so kompoziti NPCM razmeroma toplotno stabilnejši kot osnovni PCM.

Zaradi povišane toplotne prevodnosti kompozitov NPCM je mogoče pospešiti tudi hitrost taljenja in strjevanja med cikli polnjenja in praznjenja. Za najboljši izkoristek razpoložljive sončne energije bi zato bilo mogoče povečati volumsko kapaciteto sistema za ST na osnovi NPCM oz. zagotoviti prostor za hrambo večjih količin NPCM. Tako bi se dalo maksimalno izkoristiti potencialno specifično latentno toploto NPCM za shranjevanje dodatne toplote in SGV bi lahko zagotavljali dodatno vročo vodo pri želeni temperaturi. Predlagani kompoziti NPCM so tako lahko najboljša alternativa konvencionalnim parafinskim PCM za gospodinjske SGV z integrirano možnostjo ST. Potencialna uporaba predlaganih kompozitov NPCM pa ni omejena le na ST v SGV, saj so primerni tudi za ST v sistemih za rekuperacijo nizkotemperaturne odpadne toplote in za toplotno upravljanje elektronike. Za potrditev toplotnih lastnosti NPCM v daljšem časovnem obdobju bodo potrebni še preizkusi s pospešenimi toplotnimi cikli, za preučitev realnega vedenja NPCM v SGV pa podrobnejše študije s toploto sonca.

Ključne besede: PCM, nanodelci grafena, kompozit NPCM, sončna energija, shranjevanje toplote, solarni grelnik vode

*Naslov avtorja za dopisovanje: Tehniški kolidž PSG, Coimbatore,Tamil Nadu, Indija, ragulkumarkittusamy@gmail.com

Strojniški vestnik - Journal of Mechanical Engineering 68(2022)7-8, SI 63

Prejeto v recenzijo: 2022-02-22
Prejeto popravljeno: 2022-04-29
Odobreno za objavo: 2022-05-12

Optimizacija ravni ogljikovega dioksida v petsedežnem vozilu

Prabhakaran Jayasankar* – Jayabal Subbaian
Vladni tehniški kolidž, Oddelek za strojništvo, Indija

Kakovost zraka v potniškem prostoru vozil je lahko petkrat slabša kot v stanovanjskih in nestanovanjskih stavbah, zaradi česar se pojavljajo zdravstvene težave, kot so glavobol, draženje grla in slabost, ki so simptomi onesnaženega zraka. Nadzor ogljikovega dioksida kot enega glavnih onesnaževal v kabinah vozil je pogoj za regulacijo ravni ogljikovega dioksida. Pričujoča raziskava obravnava beleženje ravni ogljikovega dioksida pri različnem številu potnikov, hitrosti zraka in temperaturi. Potniki v klimatiziranih vozilih bodo tako lahko uporabljali svoje klimatske naprave na optimalen način za zdravo uporabniško izkušnjo.

Raziskovalni problem je določitev minimalne vrednosti onesnaževal zraka v potniškem prostoru, kot je ogljikov dioksid, pri različnem številu potnikov, hitrosti zraka in temperaturi. Za določitev minimalne ravni ogljikovega dioksida pri različnih obremenitvah ter ustrezne hitrosti zraka in temperature v vozilu tipa kombilimuzina je bila uporabljena zasnova, analiza in optimizacija po metodi odzivnih površin. Poleg tega so bili za določanje minimalne ravni ogljikovega dioksida uporabljeni metoda odzivnih površin, posplošena metoda reduciranega gradienta in genetski algoritem. Večina raziskovalcev pri iskanju optimalnih vrednosti odgovorov uporablja statistične, gradientne in metahevristične algoritme.

Za meritve koncentracije ogljikovega dioksida v vozilu je bil uporabljen prenosljivi merilnik IAQ CO_2 proizvajalca Extech (model CO250). Merilna naprava deluje po načelu nedisperzivne infrardeče spektroskopije (NDIR) ter lahko meri koncentracije do 5000 ppm z ločljivostjo 1 ppm. Merilnik je bil nastavljen za snemanje podatkov v enominutnih intervalih. Rezultati meritev CO_2 so bili nato s proizvajalčevo programsko opremo preneseni v prenosni računalnik. Izbran je bil petsedežni avtomobil tipa kombilimuzina s klimatsko napravo, ki omogoča nastavitev temperature v območju od 18 °C do 25 °C ter vklop in izklop kroženja zraka.

Opravljeni so bili po trije preizkusi za primere, ko v avtu sedi 1 do 5 potnikov. Pri končni optimizaciji parametrov so bile uporabljene povprečne vrednosti rezultatov vseh treh preizkusov. Po opravljenih eksperimentih so bile uporabljene optimizacijske tehnike z metahevrističnimi algoritmi.

Opravljeni so bili eksperimenti v optimalnih pogojih, določenih po metodah RSM, GRG in GA, vrednosti ravni ogljikovega dioksida pa so bile nato razvrščene in primerjane z optimalnimi vrednostmi. Napovedane ravni ogljikovega dioksida po metodi RSM ob prisotnosti 1 do 5 ljudi v kabini so znašale 479,983 ppm, 503,832 ppm, 580,79 ppm, 659,905 ppm in 769,362 ppm. Eksperimentalno določene vrednosti so znašale 479,983 ppm, 503,832 ppm, 589,124 ppm, 659,823 ppm, 769,362 ppm in 772,268 ppm. Absolutne odstotne vrednosti napake metode GRG ob prisotnosti 1 do 5 ljudi v kabini so znašale 0,13 %, 0,09 %, 0,09 %, 0,17 % oz. 0,11 %. Napovedane ravni ogljikovega dioksida po metodi GA ob prisotnosti 1 do 5 ljudi v kabini so znašale 479,983 ppm, 503,832 ppm, 589,124 ppm, 659,823 ppm in 769,016 ppm. Eksperimentalno določene vrednosti so znašale 479,983 ppm, 503,832 ppm, 589,124 ppm, 659,823 ppm in 772,268 ppm.

Lastnosti kakovosti zraka v notranjem prostoru, kot so relativna vlažnost zraka, vsebnost trdnih delcev, raven ogljikovega monoksida in raven kisika, je mogoče optimizirati z optimizacijskimi tehnikami ter določiti optimalno vrednost za ugodno in zdravo življenje v notranjih prostorih. S temi metodami je mogoče določiti optimalne vhodne parametre klimatizacije, kot so vhodna hitrost, pretok svežega zraka, način filtriranja in zahtevana temperatura zraka za različne obremenitve notranjega prostora. Lastnosti zraka v notranjih prostorih so odvisne od vsakokratnega prostora, vrednosti v različnih državah pa se lahko spreminjajo v odvisnosti od okoljskih razmer in nenadnih klimatskih sprememb na zadevnem geografskem področju. Študijo bo v prihodnje mogoče razširiti tudi na ostala vozila, kot so športni terenci in avtomobili s sedmimi sedeži, tovornjaki, avtobusi in celo vlaki, ob upoštevanju spremenljivega števila potnikov, nadmorske višine, načina prezračevanja in zunanjih vremenskih pogojev. Študija je tako dobro izhodišče za raziskovalce kakovosti zraka v notranjih prostorih, ki uporabljajo računalniške tehnike za učinkovito analizo zdravja in ugodja v avtomobilskih kabinah. Področje optimizacije kakovosti zraka v vozilih je sicer omenjano v literaturi, kar pa le v manjši meri velja za optimizacijo vhodnih parametrov s ciljem zmanjševanje ravni CO_2 v kabinah kombilimuzin. V pričujočem delu so bili zato uporabljeni trije algoritmi za optimizacijo onesnaževal zraka v kabini.

Ključne besede: ogljikov dioksid, petsedežno vozilo, genetski algoritem, kakovost zraka v vozilu, metoda odzivnih površin

*Naslov avtorja za dopisovanje: Vladni tehniški kolidž, Oddelek za strojništvo, Indija, jpkn006@gmail.com

Strojniški vestnik - Journal of Mechanical Engineering 68(2022)7-8, SI 64

Prejeto v recenzijo: 2022-04-25
Prejeto popravljeno: 2022-06-20
Odobreno za objavo: 2022-07-08

Optimizacija postopka uporovnega točkovnega varjenja magnezijeve zlitine AZ61

Davood Afshari[1] * – Ali Ghaffari[1] – Zuheir Barsum[2]

[1] Univerza v Zanjanu, Iran
[2] Kraljevi inštitut za tehnologijo, Švedska

V članku je predstavljena integracija umetne nevronske mreže (ANN) in večciljnega genetskega algoritma (GA) za optimizacijo uporovnega točkovnega varjenja magnezijeve zlitine AZ61. Magnezijeve (Mg) zlitine v zadnjem času pridobivajo vse več pozornosti in pomena v kategoriji kovin, ki so enostavne za obdelavo. Odlikuje jih izjemno razmerje med trdnostjo in maso, med drugim pa jih uporabljajo v avtomobilski, letalski in vesoljski industriji ter za gradnjo konstrukcij. Kljub znatnemu zanimanju pa ostaja industrijska uporaba magnezijevih zlitin v primerjavi z aluminijevimi in jeklenimi zlitinami omejena zaradi nekaterih tehničnih težav. Uporovno točkovno varjenje (UTV) magnezijevih zlitin je bolj kompleksno kot UTV jeklenih in aluminijevih zlitin ter zahteva drugačne varilne parametre. Glavni cilj pričujoče študije je bila zato identifikacija optimalnih parametrov UTV za kakovostne zvarne spoje z visoko trdnostjo. Stabilnost in trdnost zvarnega spoja sta močno odvisni od velikosti zvarne leče in preostalih napetosti po postopku varjenja, zato je glavni cilj optimizacije doseganje največje velikosti zvarne leče in minimalnih preostalih nateznih napetosti v območju zvara.

Glavni varilni parametri, ki vplivajo na kakovost zvarov, so električni tok, čas varjenja in sila elektrod. Uporabljena je bila faktorska zasnova eksperimentov za preučitev vpliva varilnih parametrov na velikost zvarne leče in preostalih napetosti v uporovnem točkovnem zvarnem spoju materiala AZ61. Iz polne faktorske zasnove eksperimentov izhaja skupaj 8 kombinacij vhodnih parametrov za varjenje preizkušancev. Zvarjeni preizkušanci so bili prerezani po srednjici in nato je bila z optičnim mikroskopom izmerjena velikost zvarne leče. Za meritve preostalih napetosti je bila izbrana metoda XRD. Električni tok, čas varjenja in njune interakcije vplivajo na velikost zvarne leče, medtem ko sila elektrod in njene interakcije z ostalimi spremenljivkami praktično nimajo nikakršnega vpliva. Električni tok ima največji vpliv na velikost zvarne leče. Čas varjenja in sila elektrod vplivata na preostale napetosti. Čas varjenja ima največji vpliv na preostale napetosti, medtem ko je vpliv električnega toka praktično zanemarljiv.

V študiji sta bili uporabljeni dve ločeni večslojni ANN s povezavami naprej in algoritmom vzvratnega razširjanja za napovedovanje velikosti zvarnih leč in največjih preostalih nateznih napetosti. Rezultati so pokazali, da lahko obe umetni nevronski mreži z visoko točnostjo napovesta velikost zvarnih leč in preostalih napetosti na osnovi parametrov uporovnega točkovnega varjenja. Končno je bil razvit še integriran večciljni algoritem ANN-ANN-GA za optimizacijo parametrov uporovnega točkovnega varjenja. Za oceno točnosti predlaganega večciljnega GA je bilo opravljeno UTV preizkušanca z optimalnimi parametri. Velikost zvarne leče in preostale napetosti so bile tudi eksperimentalno izmerjene in primerjane z napovedmi integriranega optimizacijskega algoritma. Predstavljeni integrirani algoritem ANN-ANN-GA lahko z visoko točnostjo napove velikost zvarnih leč in preostalih napetosti, optimalni parametri UTV pa zagotavljajo visoko trdnost in kakovost zvarnega spoja.

Ključne besede: uporovno točkovno varjenje, preostale napetosti, umetna nevronska mreža, genetski algoritem, magnezijeva zlitina AZ61

*Naslov avtorja za dopisovanje: Univerza v Zanjanu, Zanjan, Iran, dafshari@znu.ac.ir

Strojniški vestnik - Journal of Mechanical Engineering 68(2022)7-8, SI 65

Prejeto v recenzijo: 2022-03-31
Prejeto popravljeno: 2022-05-30
Odobreno za objavo: 2022-06-01

Vpliv dvostopenjskega staranja in obdelave RRA na abrazivno obrabo med tremi telesi pri zlitini AW7075

Marzena M. Lachowicz* − Tadeusz Leśniewski − Maciej B. Lachowicz
Znanstveno-tehniška univerza v Wroclawu, Fakulteta za strojništvo, Poljska

Pri nekaterih aplikacijah z aluminijevimi zlitinami prihaja do relativnega gibanja med površinami komponent in obrabna obstojnost je v tem primeru pomembna lastnost materiala.

Mnoge raziskave so pokazale, da lahko toplotna obdelava signifikantno vpliva na tribološko obrabo. Zlasti fragmentacija sestavnih delov v mikrostrukturi lahko pomembno vpliva na tribološke parametre.

V članku je predstavljena analiza vpliva stanja po toplotni obdelavi na abrazivno obrabo aluminijeve zlitine AW7075. Za določitev obstojnosti proti abrazivni obrabi so bili opravljeni preizkusi z napravo T-07. Glede na rezultate preizkusov so stopnje abrazivne obrabe preizkušanih zlitin po različnih toplotnih obdelavah razvrščene takole: dvostopenjsko staranje < obdelava RRA < stanje T6

Za določitev utrjevanja materiala je bila opravljena meritev trdote po Vickersu. Trdota zlitine AW7075 narašča v tem vrstnem redu: dvostopenjsko staranje < stanje T6 < obdelava RRA. Z analizo odvisnosti med trdoto in abrazivno obrabo je bilo ugotovljeno, da trdota ni edini dejavnik vpliva na tovrstno obrabo, saj imata pomembno vlogo tudi mikrostruktura preizkušene zlitine in stanje po toplotni obdelavi. Material ima po dvostopenjskem staranju in po obdelavi RRA kljub različnim vrednostim trdote podobno obrabno obstojnost in zato je bil analiziran tudi vpliv mikrostrukture. Podana je domneva, da prevlada izločenih delcev, ki so koherentni z osnovo v mikrostrukturi, spodbuja ohranjanje zveznosti osnove in izločenih delcev. Večji in nekoherentni izločeni delci v osnovi lahko nasprotno delujejo kot abraziv in povečajo stopnjo obrabe. Kontinuiteta izločkov in osnove se v tem primeru lažje prekine kot v prisotnosti koherentnih delcev. Dekohezija običajno nastopi na mejah zrn oz. na mejnih površinah. Po triboloških preiskavah je bila opravljena še preiskava površin z vrstičnim elektronskim mikroskopom za določitev dominantnega mehanizma površinskih poškodb. Obrabne lastnosti kažejo podoben tip poškodb ne glede na stanje po toplotni obdelavi. Gre predvsem za praske, brazde, mikrorazpoke in rahlo plastično deformacijo na obrabni površini. Prisotnost večjih delcev primarnih faz, ki se ne raztopijo med toplotno obdelavo, vpliva na njihovo drobljenje in defragmentacijo med abrazivnim obrabljanjem. Zaradi trenja je mogoče pričakovati dva pojava v predelu blizu površine: povečanje trdote, ki je znamenje utrjanja zaradi plastične deformacije, ter delno izginotje in rast faz izločevalnega utrjanja zaradi povišanja temperature, ki je posledica trenja.

Analiza je bila zato razširjena z meritvami porazdelitve trdote po preseku. Rezultati so pokazali, da ni prišlo do nobenega od omenjenih pojavov. Spremembe trdote, ki bi bile povezane z deformacijskim utrujanjem, ali strukturne spremembe zaradi trenja niso bile opažene.

Ključne besede: aluminijeve zlitine, AW7075, abrazivna obraba, toplotna obdelava, trdota, mikrostruktura

*Naslov avtorja za dopisovanje: Znanstveno-tehniška univerza v Wroclawu, Fakulteta za strojništvo, Oddelek za preoblikovanje, varjenje kolvin in meroslovje, Lukasiewicza 7-9, 50-371 Wroclaw, Poljska, marzena.lachowicz@pwr.edu.pl

Strojniški vestnik - Journal of Mechanical Engineering 68(2022)7-8, SI 66

Prejeto v recenzijo: 2022-01-26
Prejeto popravljeno: 2022-07-08
Odobreno za objavo022-07-11

Nitridiranje jekla HS6-5-2 v induktivno sklopljeni plazmi

Marek Binienda[1] – Robert Pietrasik[2,*] – Sylwester Pawęta[2] – Krzysztof Matczak[1] – Witold Krotewicz[1]

[1] Tehnološka skupina Zemat, Poljska

[2] Tehniška univerza v Lodžu, Inštitut za materiale in inženiring, Poljska

V članku je predstavljena raziskava o možnostih površinskega utrjevanja jekla HS6-5-2 z nitridiranjem v induktivno sklopljeni plazmi (ICP). Zaradi nenehnega tehnološkega razvoja obstaja potreba po optimizaciji funkcionalnih lastnosti materialov, ki se uporabljajo pri proizvodnji orodij in strojnih delov. Problema se je po eni strani mogoče lotiti s proizvodnjo orodnih materialov z boljšimi lastnostmi, ki zahtevajo uporabo dragih zlitinskih dodatkov v večstopenjskih tehnoloških procesih. Po drugi strani pa potekajo tudi raziskave na področju modifikacije površinskih slojev za doseganje novih, primernejših funkcionalnih lastnostih pri orodjih, ki so takoj pripravljena za uporabo. Kljub znatnemu napredku na področju inženiringa površin pa še vedno povzročajo težave metode za izboljševanje trajnosti in zanesljivosti orodij ter konstrukcijskih elementov, zlasti tistih z majhnimi dimenzijami. Ena najbolj razširjenih tehnologij, zlasti za dele majhnih dimenzij, je nitridiranje. Nitridiranje po klasični termokemični metodi povzroči formiranje krhkih slojev ε ($Fe_{2-3}N$) in γ' (Fe_4N). Procesi v nadzorovani plinski atmosferi sicer omogočajo obvladovanje fazne sestave slojev, so pa razmeroma zamudni, tudi pri pripravi tankih slojev.

Uporaba induktivno sklopljene plazme, ustvarjene v močnem magnetnem polju s Foucaultovimi tokovi, odpravlja pospeševalno električno polje. Magnetno polje tuljave ustvarja vrtinčne tokove v plinu in v obdelovancu, ti pa hkrati izpolnjujejo dve nalogi: uporovno segrevanje plina (dušika) do razelektritve in nastanka obroča plazme ter segrevanje obdelovanca do globine penetracije. Vrednost je odvisna od upornosti ioniziranega plina in obdelovanca ter od frekvence. Večkratna ionizacija delcev v nizkotemperaturni neizotermni plazmi zagotavlja učinkovit vir medija za nitridiranje in je primerna za difuzno nasičenje kovin. Uporaba inducirane plazme za nitridiranje jekel je praktično neznana, saj je objavljenih le nekaj raziskav na laboratorijski ravni.

Za preizkuse v okviru pričujoče raziskave je bilo izbrano jeklo HS6-5-2. Nitridiranje preizkušancev je bilo opravljeno v reaktorju s kvarčno cevjo v induktivno sklopljeni plazmi pri frekvenci 27,12 MHz. Delovni procesni tlak v dušikovi atmosferi s čistočo 99,9999 % je znašal 100 Pa. Plazemski reaktor je poganjal generator z naslednjimi stopnjami močmi: 500 W, 1 kW, 1,5 kW in 2 kW. Preizkušanci na delovnih mizicah iz kvarčnega stekla so bili nitridirani pri konstantnem tlaku in nastavljeni moči generatorja 15, 30 oz. 45 minut.

Mikrostruktura preizkušancev v prerezu je bila preiskana pod optičnim mikroskopom Nikon MA200 (Nikon Instech Co., Ltd., Tokio, Japonska). Mikrostruktura in kemična sestava površinskih slojev sta bili preiskani tudi pod vrstičnim elektronskim mikroskopom (SEM) JEOL JSM-6610 LV (JEOL Ltd., Tokio, Japonska), opremljenim z energijsko disperzijskim spektroskopom (EDS) X-MAX θ Oxford Instruments (Oxford Instruments Group, Abingdon, Združeno kraljestvo). Rentgentska difrakcija (XRD) je bila opravljena z napravo PANalytical Empyrean (Malvern Panalytical Ltd, Malvern, Združeno kraljestvo). Porazdelitev trdote v nitridiranih slojih je bila izmerjena z merilnikom mikrotrdote po Vickersu NEXUS θ5 (INNOVATEST Ltd., Maastricht, Nizozemska). Površinska trdota preizkušanca, pripravljenega za metalografske preiskave, je bila izmerjena na oddaljenosti 0 µm od roba preizkušanca in nato v korakih velikosti 5µ m proti notranjosti z obremenitvijo 0,θ N.

Na podlagi porazdelitve trdote po obdelavi z močjo 1 kW, 1,5 kW in 2 kW je bila določena efektivna debelina posameznih slojev po standardu DIN θ0- 3(merilo je trdota θ H V nad trdoto jedra).

Induktivno sklopljena plazma omogoča izdelavo nitridiranih slojev s primerno strukturo. Ta ugotovitev je pomembna s tehnološkega in ekonomskega vidika, saj postopek zagotavlja signifikantno skrajšanje časa obdelave ter popoln nadzor nad strukturo slojev, torej tudi nad območji brez nitridov. Možnost industrijskega nitridiranja v induktivno sklopljeni plazmi je zelo pomembna tudi z ekološkega stališča – v procesu je namreč namesto strupenega amoniaka uporabljen inertni plin dušik. Pri novi tehnologiji tudi ni emisij, ki bi zahtevale uporabo plinov za naknadno obdelavo. Dosežena je bila največja trdota pribl. 1100 HV, kar predstavlja 350-odstotno povečanje trdote v primerjavi z neobdelanim materialom. Čas obdelave za ustvarjanje slojev debeline 100 µm s funkcionalnimi lastnostmi je zelo kratek, komaj 4m inut.

Ključne besede: plazma, nitridiranje, površinski sloj, trdota

*Naslov avtorja za dopisovanje: Tehniška univerza v Lodzu, Inštitut za materiale in strojništvo, 1/15 Stefanowski c.,90-924 Lodz, Poljska, robert.pietrasik@p.lodz.pl

Guide for Authors

All manuscripts must be in English. Pages should be numbered sequentially. The manuscript should be composed in accordance with the Article Template given above. The suggested length of contributions is 10 to 20 pages. Longer contributions will only be accepted if authors provide justification in a cover letter. For full instructions see the Information for Authors section on the journal's website: http://en.sv-jme.eu .

SUBMISSION:

Submission to SV-JME is made with the implicit understanding that neither the manuscript nor the essence of its content has been published previously either in whole or in part and that it is not being considered for publication elsewhere. All the listed authors should have agreed on the content and the corresponding (submitting) author is responsible for having ensured that this agreement has been reached. The acceptance of an article is based entirely on its scientific merit, as judged by peer review. Scientific articles comprising simulations only will not be accepted for publication; simulations must be accompanied by experimental results carried out to confirm or deny the accuracy of the simulation. Every manuscript submitted to the SV-JME undergoes a peer-review process.

The authors are kindly invited to submit the paper through our web site: http://ojs.sv-jme.eu. The Author is able to track the submission through the editorial process - as well as participate in the copyediting and proofreading of submissions accepted for publication - by logging in, and using the username and password provided.

SUBMISSION CONTENT:

The typical submission material consists of:

- A **manuscript** (A PDF file, with title, all authors with affiliations, abstract, keywords, highlights, inserted figures and tables and references),
- Supplementary files:
  - a **manuscript** in a WORD file format
  - a **cover letter** (please see instructions for composing the cover letter)
  - a ZIP file containing **figures** in high resolution in one of the graphical formats (please see instructions for preparing the figure files)
  - possible **appendicies** (optional), cover materials, video materials, etc.

Incomplete or improperly prepared submissions will be rejected with explanatory comments provided. In this case we will kindly ask the authors to carefully read the Information for Authors and to resubmit their manuscripts taking into consideration our comments.

COVER LETTER INSTRUCTIONS:

Please add a **cover letter** stating the following information about the submitted paper:

1. Paper **title**, list of **authors** and their **affiliations**. **One** corresponding author should be provided.
2. **Type of paper**: original scientific paper (1.01), review scientific paper (1.02) or short scientific paper (1.03).
3. A **declaration** that neither the manuscript nor the essence of its content has been published in whole or in part previously and that it is not being considered for publication elsewhere.
4. State the **value of the paper** or its practical, theoretical and scientific implications. What is new in the paper with respect to the state-of-the-art in the published papers? Do not repeat the content of your abstract for this purpose.
5. We kindly ask you to suggest at least two **reviewers** for your paper and give us their names, their full affiliation and contact information, and their scientific research interest. The suggested reviewers should have at least two relevant references (with an impact factor) to the scientific field concerned; they should not be from the same country as the authors and should have no close connection with the authors.

FORMAT OF THE MANUSCRIPT:

The manuscript should be composed in accordance with the Article Template. The manuscript should be written in the following format:

- A **Title** that adequately describes the content of the manuscript.
- A list of **Authors** and their **affiliations**.
- An **Abstract** that should not exceed 250 words. The Abstract should state the principal objectives and the scope of the investigation, as well as the methodology employed. It should summarize the results and state the principal conclusions.
- 4 to 6 significant **key words** should follow the abstract to aid indexing.
- 4 to 6 **highlights;** a short collection of bullet points that convey the core findings and provide readers with a quick textual overview of the article. These four to six bullet points should describe the essence of the research (e.g. results or conclusions) and highlight what is distinctive about it.
- An **Introduction** that should provide a review of recent literature and sufficient background information to allow the results of the article to be understood and evaluated.
- A **Methods** section detailing the theoretical or experimental methods used.
- An **Experimental section** that should provide details of the experimental set-up and the methods used to obtain the results.
- A **Results** section that should clearly and concisely present the data, using figures and tables where appropriate.
- A **Discussion** section that should describe the relationships and generalizations shown by the results and discuss the significance of the results, making comparisons with previously published work. (It may be appropriate to combine the Results and Discussion sections into a single section to improve clarity.)
- A **Conclusions** section that should present one or more conclusions drawn from the results and subsequent discussion and should not duplicate the Abstract.
- **Acknowledgement** (optional) of collaboration or preparation assistance may be included. Please note the source of funding for the research.
- **Nomenclature** (optional). Papers with many symbols should have a nomenclature that defines all symbols with units, inserted above the references. If one is used, it must contain all the symbols used in the manuscript and the definitions should not be repeated in the text. In all cases, identify the symbols used if they are not widely recognized in the profession. Define acronyms in the text, not in the nomenclature.
- **References** must be cited consecutively in the text using square brackets [1] and collected together in a reference list at the end of the manuscript.
- **Appendix(-icies)** if any.

SPECIAL NOTES

Units: The SI system of units for nomenclature, symbols and abbreviations should be followed closely. Symbols for physical quantities in the text should be written in italics (e.g. *v*, *T*, *n*, etc.). Symbols for units that consist of letters should be in plain text (e.g. ms^{-1}, K, min, mm, etc.). Please also see: http://physics.nist.gov/cuu/pdf/sp811.pdf .

Abbreviations should be spelt out in full on first appearance followed by the abbreviation in parentheses, e.g. variable time geometry (VTG). The meaning of symbols and units belonging to symbols should be explained in each case or cited in a **nomenclature** section at the end of the manuscript before the References.

Figures (figures, graphs, illustrations digital images, photographs) must be cited in consecutive numerical order in the text and referred to in both the text and the captions as Fig. 1, Fig. 2, etc. Figures should be prepared without borders and on white grounding and should be sent separately in their original formats. If a figure is composed of several parts, please mark each part with a), b), c), etc. and provide an explanation for each part in Figure caption. The caption should be self-explanatory. Letters and numbers should be readable (Arial or Times New Roman, min 6 pt with equal sizes and fonts in all figures). Graphics (submitted as supplementary files) may be exported in resolution good enough for printing (min. 300 dpi) in any common format, e.g. TIFF, BMP or JPG, PDF and should be named Fig1.jpg, Fig2.tif, etc. However, graphs and line drawings should be prepared as vector images, e.g. CDR, AI. Multi-curve graphs should have individual curves marked with a symbol or otherwise provide distinguishing differences using, for example, different thicknesses or dashing.

Tables should carry separate titles and must be numbered in consecutive numerical order in the text and referred to in both the text and the captions as Table 1, Table 2, etc. In addition to the physical quantities, such as *t* (in italics), the units [s] (normal text) should be added in square brackets. Tables should not duplicate data found elsewhere in the manuscript. Tables should be prepared using a table editor and not inserted as a graphic.

REFERENCES:

A reference list must be included using the following information as a guide. Only cited text references are to be included. Each reference is to be referred to in the text by a number enclosed in a square bracket (i.e. [3] or [2] to [4] for more references; do not combine more than 3 references, explain each). No reference to the author is necessary.

References must be numbered and ordered according to where they are first mentioned in the paper, not alphabetically. All references must be complete and accurate. Please add DOI code when available. Examples follow.

Journal Papers:

Surname 1, Initials, Surname 2, Initials (year). Title. *Journal*, volume, number, pages, DOI code.

[1] Hackenschmidt, R., Alber-Laukant, B., Rieg, F. (2010). Simulating nonlinear materials under centrifugal forces by using intelligent cross-linked simulations. *Strojniški vestnik - Journal of Mechanical Engineering,* vol. 57, no. 7-8, p. 531-538, DOI:10.5545/sv-jme.2011.013.

Journal titles should not be abbreviated. Note that journal title is set in italics.

Books:

Surname 1, Initials, Surname 2, Initials (year). Title. Publisher, place of publication.

[2] Groover, M.P. (2007). *Fundamentals of Modern Manufacturing*. John Wiley & Sons, Hoboken.

Note that the title of the book is italicized.

Chapters in Books:

Surname 1, Initials, Surname 2, Initials (year). Chapter title. Editor(s) of book, book title. Publisher, place of publication, pages.

[3] Carbone, G., Ceccarelli, M. (2005). Legged robotic systems. Kordić, V., Lazinica, A., Merdan, M. (Eds.), Cutting Edge Robotics. Pro literatur Verlag, Mammendorf, p. 553-576.

Proceedings Papers:

Surname 1, Initials, Surname 2, Initials (year). Paper title. Proceedings title, pages.

[4] Štefanić, N., Martinčević-Mikić, S., Tošanović, N. (2009). Applied lean system in process industry. *MOTSP Conference Proceedings*, p. 422-427.

Standards:

Standard-Code (year). Title. Organisation. Place.

[5] ISO/DIS 16000-6.2:2002. *Indoor Air – Part 6: Determination of Volatile Organic Compounds in Indoor and Chamber Air by Active Sampling on TENAX TA Sorbent, Thermal Desorption and Gas Chromatography using MSD/FID.* International Organization for Standardization. Geneva.

WWW pages:

Surname, Initials or Company name. Title, from http://address, date of access.

[6] Rockwell Automation. Arena, from *http://www.arenasimulation.com,* accessed on 2009-09-07.

EXTENDED ABSTRACT:

When the paper is accepted for publishing, the authors will be requested to send an **extended abstract** (approx. one A4 page or 3500 to 4000 characters or approx. 600 words). The instruction for composing the extended abstract are published on-line: http://www.sv-jme.eu/information-for-authors/ .

COPYRIGHT:

Authors submitting a manuscript do so on the understanding that the work has not been published before, is not being considered for publication elsewhere and has been read and approved by all authors. The submission of the manuscript by the authors means that the authors automatically agree to publish the paper uder CC-BY 4.0 Int. or CC-BY-NC 4.0 Int. when the manuscript is accepted for publication. All accepted manuscripts must be accompanied by a Copyright Agreement, which should be sent to the editor. The work should be original work by the authors and not be published elsewhere in any language without the written consent of the publisher. The proof will be sent to the author showing the final layout of the article. Proof correction must be minimal and executed quickly. Thus it is essential that manuscripts are accurate when submitted. Authors can track the status of their accepted articles on https://en.sv-jme.eu/.

PUBLICATION FEE:

Authors will be asked to pay a publication fee for each article prior to the article appearing in the journal. However, this fee only needs to be paid after the article has been accepted for publishing. The fee is 380 EUR (for articles with maximum of 6 pages), 470 EUR (for articles with maximum of 10 pages), plus 50 EUR for each additional page. The additional cost for a color page is 90.00 EUR (only for a journal hard copy; optional upon author's request). These fees do not include tax.

9 770039 248001
ISSN 0039-2480

http://www.sv-jme.eu

Contents

Papers